Numerical Simulations of Wakes, Blade-Vortex Interaction, Flutter, and Flutter Suppression by Feedback Control

by

Bonian Dong

Dissertation submitted to the Faculty of the

Virginia Polytechnic Institute and State University

in partial fulfillment of the requirements for the degree of

Doctor of Philosophy

in

Engineering Mechanics

APPROVED:

Dean T. Mook

Dr. Dean. T. Mook, Chairman

Ali H. Nayfeh

Dr. Ali. H. Nayfeh

Raymond H Plaut

Dr. Raymond. H. Plaut

Saad Ragab

Dr. Saad A. Ragab

Scott L. Hendricks

Dr. Scott L. Hendricks

August, 1991

Blacksburg, Virginia

c.2

LD
5655
V856
1991

D663
c.2

Numerical Simulations of Wakes, Blade-Vortex Interaction, Flutter, and Flutter Suppression by Feedback Control

by

Bonian Dong

Dr. Dean. T. Mook, Chairman

Engineering Mechanics

(ABSTRACT)

A general aerodynamic model for two-dimensional inviscid flows is developed. This model is used to simulate wakes and blade-vortex interaction. This model is also coupled with dynamics and feedback controls to simulate flutter and flutter suppression.

The flow is assumed to be attached and incompressible. The present aerodynamic model is based on a vorticity-panel method coupled with vortex dynamics.

The present aerodynamic model is used to simulate some actual experiments: wakes generated by oscillating airfoils and blade-vortex interactions in which one airfoil is placed in or near the wake generated by another oscillating airfoil upstream. The present numerical model predicts wake structures, vorticity strength, and velocity profiles across the wake that compare very favorably with the experiments. The present numerical results of the blade-vortex interaction show good agreement with the experiments when separation does not occur. If separation is involved, the present model fails to accurately simulate blade-vortex interaction because separation is not considered in the present model.

Flutter is studied by means of numerical simulations. In an incompressible flow, an airfoil is mounted on an elastic support. The airfoil can pitch (rotate) and plunge (translate vertically). The dynamic equations that describe this two-degree-of-freedom motion are general and nonlinear. To calculate the aerodynamic loads on the airfoil, the aerodynamic model is coupled with this dynamic model. The motions of the airfoil and flowing air are calculated interactively and simultaneously.

The coupled aerodynamic/dynamic model accurately predicts the critical flutter speed of the freestream, the speed at which the motion of the airfoil grows spontaneously. The contributions of the phase difference and energy exchange to the flutter motion are discussed. The effect of the static angle of attack on the critical flutter speed is investigated. Also the effect of the nonlinearity of the elastic support (cubic term in the hardening spring) is studied.

A feedback control is coupled with aerodynamics/dynamics to suppress the flutter motion of the airfoil. A flap is added at the trailing edge of the airfoil as a control surface, and its deflection (rotation) about the hinge point is commanded by a feedback-control law. The flow, airfoil, elastic support, and control device are considered as one system, and the flow, the motions of the airfoil, and the flap deflections are calculated simultaneously.

With carefully designed control laws, oscillations that would be unstable (i.e., growing) without control are suppressed. The numerical results show different control variables can be used. The model of aerodynamics/dynamics/control is also used to successfully suppress the response to a wind gust with the same control laws as used for the suppression of flutter.

Acknowledgements

This dissertation profited greatly from the guidance, assistance and encouragement of my advisor, Dr. Dean T. Mook. I would like to take this opportunity to express my gratitude and appreciation to him. I would also like to thank Dr. Ali H. Nayfeh, Dr. Raymond. H. Plaut, Dr. Saad A. Ragab and Dr. Scott L. Hendricks for spending their valuable time reading this manuscript. I wish to express my appreciation to Dr. Demetri P. Telionis and his students for providing some publications and their experimental results related to my work.

I would like to express my deep appreciation to my wife, Yuanjuan Gu, and my daughter, Xai Dong, for all the love, understanding, encouragement and support they have given through the years.

Table of Contents

List of Illustrations

List of Tables

Chapter 1. Introduction

1.1 Problem Statement

The numerical simulation of wakes has been an important topic in the study of vorticity-dominated flows. Here, by actually simulating some experiments in which an airfoil oscillates and generates a wake, the emphasis is put on the large-scale structure of the wake and strength of vorticity instead of on the study of instability during the evolution of a vortex sheet. With accurately computed wakes, some wind-tunnel experiments on blade-vortex interaction (BVI) are simulated, in which an airfoil is placed in or near the wake generated by another airfoil oscillating upstream.

Also in this dissertation some problems of unsteady aeroelasticity are numerically studied. During flying, small disturbances can trigger wild oscillations of the wings depending on the speed of the air flow; this is called the flutter phenomenon. How to predict the flutter speed and how to suppress the flutter by feedback control are investigated in this dissertation. The aerodynamic loads on the airfoil are predicted by an aerodynamic model instead of being approximated by some functions. The flowing air, the airfoil, the elastic support, and the control device, which is a flap hinged at the trailing edge of the airfoil, are considered parts of the same dynamic system and are

obtained simultaneously and interactively. Feedback control is also applied to the suppression of the response to a wind gust.

1.2 Motivation for Present Research

1.2.1 Vorticity-Dominated Flows

When the Reynolds number is high, the vorticity is often confined to some small regions in the flowfield. For example, in the unsteady flow around an airfoil at sufficiently small angles of attack, most of the vorticity lies in the boundary layer and the wake, and outside these regions the flow can be considered irrotational. Then the boundary layer can be treated as a bound vortex sheet with zero thickness, and the wake can be considered the result of the stretching and rolling-up of the vortex sheet shed from the trailing edge. This analysis offers an alternative to solving the Navier-Stokes or Euler equations. In the present analysis, velocity is obtained by using the Biot-Savart law or the Green's function once the vorticity is known. In other words, the problem of fluid dynamics is turned into one of vortex dynamics.

Fully understanding and accurately simulating wakes are of paramount importance in many aerodynamic problems. One of the methods of simulating wakes is to discretized a continuous vortex sheet that simulates a wake into a system of point vortices or vortex blobs. Some studies are focused on the instability of the discrete model of a vortex sheet and the formation of a singularity in it (Krasny, 1986). In such work, the convergence of the discrete model of vortex sheets is studied theoretically and numerically by investigating the effects of the round-off error of computers, size of the meshes used for discretization and smoothing parameter used to diminish the singularities. On the other hand, as an application of this discrete model of a

continuous vortex sheet some work is concentrated on how to accurately simulate wakes: their large-scale structures and vorticity strength. For practical use, the emphasis of the wake study in this dissertation is put on the implementation of the discrete vortex model and simulation of some available experiments and comparison between the numerical and experimental wakes.

Blade-vortex interaction is of considerable interest to researchers and designers because it is a primary source of unsteady loads. BVI is a three-dimensional unsteady phenomenon, but many researchers have simplified the problem by assuming that the axes of the vortices interacting with the blade are parallel to the span of the blade and then treated the flowfield as two-dimensional. In some of the earlier studies, the interaction was simulated by using a single vortex or arranging a system of vortices in a certain pattern (such as a round disk) and releasing it from upstream. With the present method of simulating the wake in some detail, it is possible to get a closer look at the BVI by actually simulating some wind-tunnel tests: an airfoil is placed in or near the wake generated by another airfoil pitching upstream.

1.2.2 Flutter and Flutter Suppression by Feedback Control

One of the major problems in aeroelasticity is the flutter of elastic structures (such as an airfoil) in wind. It is well known that the aerodynamic loads on the structure increase as the wind speed increases. At some critical speed of wind, small disturbances can cause severe damage because of the resulting violent oscillations. This is a problem of dynamic aeroelastic instability.

Another interesting problem in aeroelasticity is the response of an airfoil to a wind gust.

The early studies of the flutter of an airfoil considered incompressible attached flows and linear springs. For the convenience of calculation, the equations of

motion were linearized and the aerodynamic loads were approximated by Wagner's function. To improve the accuracy of the prediction on the aerodynamic loads, the aerodynamic model developed in this dissertation is used, which actually is used to calculate the pressure distribution on the surface of the airfoil. Then it is expected that the present analysis of flutter will be more realistic.

Naturally, the next problem is how to suppress the flutter or the response to a wind gust. This job is done by the control surface added at the trailing edge of the airfoil, which is commanded according to a control law, which has to be chosen by designers.

1.3 Literature Review

1.3.1 Vorticity-Dominated Flows

Since Helmholtz (1858) first introduced the concept of vortex dynamics, many researchers have studied this field and developed numerous vortex methods to compute vorticity-dominated flows. Sarpkaya (1989) gave a very extensive and comprehensive review of the computational methods with vortices. He discussed both the fundamental theories and the practical applications of vortex methods. In the first section of his review, he covered topics such as vorticity transportation, evolution of a vortex sheet and instabilities, Biot-Savart law, techniques of smoothing singularities, representation of bodies in the flow, and basic ideas of some numerical schemes. In the second section he presented the varieties of practical methods of computing two-dimensional and three-dimensional flows. The vortex-methods had been previously reviewed as well by Leonard (1980), Aref (1983), Aref et al. (1988) and Spalart (1988) with emphasis on some specific subjects.

As mentioned at the beginning of this chapter, in the present study the vorticity is constrained in a very thin boundary layer when the Reynolds number is large and the flow is attached. Therefore, a natural way to represent the existence of a solid body in the flow is to approximate the thin boundary layer as a vortex sheet and then impose the no-penetration condition on the surface of the body. Several different vorticity distributions have been used. Spalart (1988) arranged point vortices spaced on the surface of the solid body to represent the surface. Anderson (McGraw Hill, 1984) divided the surface of the body into small segments (panels) and used a constant vorticity distribution on each panel. The above two methods do not give a continuous surface velocity on the solid body. Raj and Gray (1978) and Kim and Mook (1986) used linear vorticity distributions on each panel so that the surface velocity is continuous at each connected point (called a node). Maskew (1980), in his calculation, divided panels into even smaller subpanels whenever and wherever the gradient of the surface velocity was locally large intending to improve the accuracy. Consequently, the number and location of subpanels were changing from time to time, and the running time was increased.

For the present model, it is assumed that the flow is attached on the surface of the solid body. Then raised is a question of how the flow leaves the sharp edge, the trailing edge of an airfoil for instance. The condition at the trailing edge is usually referred to as the Kutta condition. The studies by Poling and Telionis (1986, 1987) and the thesis of Poling (1985) contain extensive reviews of earlier work as well as their own results on the Kutta condition. Mathematically this condition is needed for the unique solution. As discussed by Poling and Telionis (1986), there are different ways to impose the Kutta condition: the pressure across the trailing edge is continuous, or the velocity is finite there.

For the steady flow, the stagnation streamline bisects the wedge angle of the trailing edge, and no vorticity is shed there (Poling and Telionis, 1986).

For the unsteady flows, the situation at the trailing edge is different: the circulation around the airfoil changes with time; hence, vorticity is shed into the wake according to the circulation-conservation law. To determine the vorticity-shedding rate, the understanding of the flowfield in the immediate neighborhood of the trailing edge is very important. Giesing (1969) analyzed the kinematic characteristics around the trailing edge by the conformal-mapping method. Based on the assumption that the mean velocity at the trailing edge is finite and nonzero, he showed that the vortex sheet was shed parallel to the upper or lower surface of the trailing edge depending on the direction of the shed vorticity. Maskell (1971) made the same argument later. Basu and Hancock (1978) pointed out that the Giesing/Maskell model could not reach the steady case as the rate at which the circulation changes goes to zero because the stagnation streamline bisects a wedged trailing edge. They argued without proof that, as the circulation rate goes to zero, the curvature of the streamline emanating from the trailing edge tends to infinity.

As discussed by Poling and Telionis (1986), the Giesing/Maskell model leads to the conclusion that, at the trailing edge, either the velocity on the upper surface or the velocity on the lower surface must be zero. This is supported by some experiments as well. In their experiment, Poling and Telionis (1986) released dyes of different colors into the upper-surface and lower-surface boundary layers on a NACA 0012 airfoil oscillating in pitch. For reduced frequencies in a certain range, they observed that during most of the downstroke, the shear layer emanating from the trailing edge had the color of the lower-surface boundary layer while a pool of the color of the upper-surface boundary layer formed on the upper surface at the trailing edge. The observations support the Giesing/Maskell model of trailing-edge flow. More recently, Liu et al. (1990) studied the flow in the trailing-edge region. In their experiment, they placed a rotating ellipse downstream from and below the trailing edge of a fixed NACA 0012 airfoil. After examining the flow near the

trailing edge by means of laser velocimetry, they also concluded that the model described above is realistic.

Hsu and Wu (1986, 1988) developed an alternative to the above model of the trailing-edge flowfield and argued that, generally in real unsteady flows, the vortex sheet released at the trailing edge does not have to be tangent to one of the surfaces. Their result was based on the argument that neither the upper-surface velocity nor the lower-surface velocity is zero. By using the momentum equation over a small control volume at the trailing edge, they calculated the velocities just aft of the trailing edge, which were deflected at finite angles. Then it seems that there is a velocity discontinuity at the trailing edge according to their analysis.

For the unsteady flow, the vorticity shed at the trailing edge forms a continuous vortex sheet. As it convects downstream, this vortex sheet stretches and rolls up and is usually referred as the wake of the airfoil. The evolution of vortex sheets is accompanied by the problem of instability. A linear stability analysis (Krasny, 1986) of the partial differential equation describing the motion of a vortex sheet showed that the shorter the wave of a disturbance is, the faster the disturbance grows (known as Kelvin-Helmholtz instability). Extensive work on this subject has been presented in the articles by Meiron et al. (1982), Moore (1979, 1984), Pozrikidis and Higdon (1985), Caflisch (1988), Aref et al. (1988), and many others.

For the purpose of expediting the numerical calculations, the continuous vortex sheet is modelled as a system of discrete point vortices. This model came from the idea of Rosenhead (1931), who first used point vortices. As Krasny (1988) pointed out the discrete model is not stable because of the Kelvin-Helmholtz instability and computer round-off error, and that this can be overcome by smoothing (removing) the singularity of point vortices. As Sarpkaya's reviewed (1989), many smoothing techniques have been developed, such as a cutoff scheme, a sub-vortex method, amalgamation of

vortices, re-discretization method, and so forth. Another smoothing method not mentioned in Sarpkaya review is to split two adjacent vortices into three whenever the two are convected apart farther than a critical length (Mook et al., 1987, 1989). The newly created vortex is put between the two and the total circulation is maintained. This method produces good simulations of the stretching of the wake.

Another approach to study the vortex sheet is to focus on the wake structure in large scale, the velocity field disturbed by the evolution of the wake, and vorticity strength of the wake. Wilder et al. (1990) provided evidence that the stability characteristics of a free vortex sheet do not influence the way a shear layer rolls up into a large-scale vortical structures.

The unsteady aerodynamics of oscillating airfoils, such as those pitching and/or plunging, have been of great interest to researchers. McCrosky (1982) gave a review on the work in this area. In some certain ranges of the amplitude and frequency of the oscillation, the flow on the surface of the airfoil stays attached, so the vortex sheet leaves the airfoil at the trailing edge. Such experiments have been conducted focussing on the flow near the trailing edge. Ohashi and Ishikawa (1972) and Ho and Chen (1980, 1981) experimentally studied the Kutta condition by means of a plunging airfoil. Poling and Telionis (1986) did something similar using a pitching airfoil. Park et al. (1988) also conducted an experiment on the near wake with a pitching airfoil. They detected the trailing-edge stall and found out that its occurrence is related to the reduced frequency of the pitching.

The far wake has also been investigated. The experimental and numerical study of Mathioulakis et al. (1985) demonstrates that the flowfield is controlled almost entirely by the inviscid self-interaction of vorticity. This claim is further confirmed by the experimental and numerical work of Wilder et al. (1990). Mook et al. (1987, 1989) numerically simulated the wake of a oscillating airfoil by using discrete vortices, and the large-scale structure of the computed wake

is very similar to the flow visualization obtained by Bratt (1950). Koochesfahani's experiment (1989) showed that the wake structure can be controlled by the frequency, amplitude, and the shape of the oscillation waveform. Booth (1987) measured, in a wind tunnel, the velocity behind a pitching airfoil and numerically integrated the measurements to obtain the circulations around the regions of concentrated vorticity. The numerical results of Mook and Dong (1990) obtained by using discrete vortices agree very well with Booth's experimental results.

One of important problems in the area of vorticity-dominated flows is the blade-vortex interaction (BVI), which happens in the flow about the helicopter blades and is a primary source of unsteady loads and noise. When a rotor advances, the blades encounter the vortex filaments generated by the preceding blades. Generally, BVI is a complicated three-dimensional unsteady phenomenon, but it can be considered as the combination of the two limit cases (Srinivasan, 1985), one in which the vortex filament is parallel to the span of the blade, and one in which the vortex filament is perpendicular to the span. The former is nearly a two-dimensional problem and is studied in this dissertation.

The two-dimensional BVI has been experimentally investigated by Poling et al. (1988), Booth and Yu (1986), Booth (1986,1987), and Straus et al. (1990). In all those experiments, which were conducted either in the wind tunnel or in the water tunnel, similar apparatus was used: a stationary airfoil was placed in or near the wake generated by a pitching airfoil upstream. The flow field and loads on the stationary airfoil were measured.

The early numerical models of BVI considered the case where a single point vortex is released far upstream and passes through the neighborhood of an airfoil. This case has been solved by employing the Euler equations for compressible flows and the Navier-Stokes equations for incompressible flows (Srinivasan, 1985; Srinivasan et al., 1984, 1986; Domodaran and Caughey,

1988; Wu et al., 1985; Hsu and Wu, 1986). Conformal mapping and vortex methods have been used as well to simulate BVI for incompressible inviscid flows (Huang and Chow, 1982; Chow and Huang, 1983; Wu et al., 1985; Hsu and Wu, 1986, 1988; Poling et al., 1987, 1988, Dong, 1987). The major shortcoming of this single-vortex model is that in the actual situation the vorticity is not confined to a point; instead it is distributed over a finite area. Consequently, the single-vortex model appears to be reasonable only when the dimension of the vorticity-bearing area is small compared to its distance from the airfoil. Improved models have been developed by using more than just one vortex to simulate the finite vorticity-bearing area (Panaras, 1987; Lee and Smith, 1987; Poling et al., 1988).

Even further, Dong and Mook (1990), Mook and Dong (1990) developed a numerical model that actually simulates Booth's experiment (1986, 1987) by the vortex method. Though their results do not agree with Booth's, they are close to the recent experiment of Straus et al. (1990). In Booth's experiment there was a very close interaction and the vorticity passing by was strong, so separation most likely happened on the surface of the stationary airfoil. The vorticity in the experiment of Straus et al. was weaker and the interaction was not as close as Booth's. This is why the model of Dong and Mook, which is based on the assumption of attached flows, could not simulate Booth's experiment well.

1.3.2 Aeroelastic Behavior and Feedback Control

Flutter is an important subject in aeroelasticity. In his textbook "An Introduction to the Theory of Aeroelasticity" (Dover Publications, 1969), Fung gave a fully comprehensive description of the flutter phenomenon. Flutter is a type of self-excited nondecaying oscillation which can be triggered by a small disturbance and happens to a elastic structure at a certain critical speed of air

flow. If the separation of flow is involved and the angle of attack is near the stall angle, the flutter is called stall flutter.

Flutter has been analyzed as both two-dimensional and three-dimensional problems. For the classic two-dimensional model, the airfoil is treated as a rigid body mounted on an elastic support (Fung, 1969). Consequently, the emphasis of this model is on the motions in plunge and pitch (sometimes referred to as bending and torsion, respectively). Niblett (1988) pointed out that it is the phase difference between the two motions that makes the airfoil extract energy from the airflow. Furthermore, the airfoil with only one degree of freedom in plunge does not flutter, and the airfoil with one degree of freedom in pitch can flutter only when the angle of attack is near the stalling angle or some special mass distribution and elastic-axis locations are involved (Fung, 1969). In recent years, some two-dimensional models have been developed which consider the elastic deformation of the airfoil and use the free vibration mode shapes and generalized modal coordinates in the equations of motion of the airfoil (Rausch et al., 1990). For three-dimensional problems, similar to the two-dimensional problems, the models of both rigid wing and elastic wing have been considered (Strganac and Mook, 1987, 1990; Borland and Rizzetta, 1981; Cunningham et al., 1988; Guruswamy, 1990).

For classic two-dimensional flutter problems in incompressible flows, the aerodynamic loads are calculated by the quasi-steady aerodynamic theory or linearized aerodynamic theory which employes the Wagner function to describe the change of the circulation around the airfoil (Fung, 1969). To calculate the aerodynamic loads more accurately, many numerical models have been developed, which directly compute the flow around the airfoil to get the loads and integrate the equations of motion simultaneously. Dong and Mook (1990, 1991) used a vortex method in their study of flutter. For the two-dimensional problem in transonic flows with the restriction that the disturbances are small, various computer codes based on finite difference

schemes have been developed to capture the interaction of oscillating airfoil with the flow around it (Rizzetta, 1977, 1979; Yang et al. 1979, 1980; Guruswamy and Yang, 1981; Guruswamy, 1990; Huttse and Eastep, 1988). For the three-dimensional problems, Strganac and Mook (1987, 1990) used a vortex-lattice method to investigate, in incompressible flows, the flutter of a rigid wing and the effect of the wake roll-up at the wing tips. Borland and Rizzetta (1981), Cunningham et al. (1988), and Bennett et al. (1988) used finite-different schemes in the transonic flutter analysis for an elastic wing.

The models to compute aerodynamic loads by means of computational fluid dynamics as mentioned above are nonlinear, and so they are one of the aspects of the nonlinear aeroelasticity. Recently Dowell (1990) wrote a review article on nonlinear aeroelasticity, discussing the nonlinearities of aerodynamic models and elastic structures.

In the classic flutter analysis, the elastic support is assumed to be linear for the convenience of analysis and calculation (Fung, 1969). The linear analysis is useful to predict the instability of the motion and the critical flutter speed. However, in many engineering problems, the elastic structure is nonlinear and the nonlinearity plays an important role, especially when the amplitude of the oscillation is large after flutter begins.

Lee and LeBlanc (1986) studied the effects of a cubic term in the angular spring (offering a restoring moment in the pitch direction). In the case of a soft spring, the critical flutter speed depends on the initial value of the pitch angle. In the case of a hard spring, divergent flutter does not happen, and a limit cycle can be reached whose amplitude is independent of the initial condition of the pitch angle. Furthermore, Zhao and Yang (1990) pointed out that chaotic oscillations can occur in the case of cubic hard angular spring, depending on the position of the elastic axis.

Lee and Desrochers (1987) and Yang and Zhao (1988) analytically and experimentally investigated the effects of the preload-and-freeplay angular spring on flutter, and showed that the divergent flutter boundary is identical to that of the linear case and that the limit cycle oscillations are possible when the speed of flow is below the critical speed. For the same type of nonlinearity, Hauenstein et al. (1990), experimentally and analytically, studied the chaotic oscillations. They pointed out that, when the speed of flow is below the linear critical speed, the bounded oscillation can be either a limit cycle or chaos depending on the speed of flow.

How to suppress the aeroelastic response with a control surface at the trailing edge is naturally of interest for designers and researchers. For the classic two-dimensional problem, Niblett (1988) discussed a method using a mass-balanced flap to influence the eigenvalues of the system. However, feedback control (active control) is often used in the recent research. Ohta et al. (1989) studied active flutter suppression for a two-dimensional airfoil in an incompressible flow. For the three-dimensional wing, Nissim and Burken (1988) developed a method for which no specific control law is required. This method is based on the aerodynamic-energy concept whereby the activated control surface is placed where most of the energy is extracted from the flow to the unstable structure. Matsuzaki et al. (1989) did both analytical and experimental work on the alleviation of flutter for a transport-type wing.

1.4 Outline and Contributions of Present Work

1.4.1 Outline

In Chapter 2, the aerodynamic model is described in detail. The thin boundary layer on the surface of an airfoil is modeled as a vortex sheet which is

approximated by a number of linearly piecewise continuous vorticity panels. The wake is represented by a system of discrete vortices. To capture some of the details of the structures of the wake, a splitting method is applied to the vortices in the discretized vortex sheet, so that the vorticity distribution along this vortex sheet can vary more smoothly. The method of calculating the aerodynamic loads is discussed, which integrates the Euler equation on the surface of the airfoil to evaluate the pressure relative to the trailing edge instead of using Bernoulli's equation. Also the methods of calculating the aerodynamic loads on a flat-plate airfoil, and the suction force acting at the leading edge, are discussed.

In Chapter 3, the numerical simulation of the wake and blade-vortex interaction are presented, and comparisons are made with some available experimental results. The wakes predicted by the present inviscid model are in good agreement with experiments. Specifically the spacing between the regions of concentrated vorticity, the circulation around these regions, and the velocity profiles across these regions all agree with experiments. The present simulations show that the evolution of the wake within a certain distance behind the airfoil is mainly controlled by an inviscid mechanism. Blade-vortex interaction is investigated by actually simulating a wind tunnel test in which an airfoil is placed in or near the wake of another instead of by using a single vortex or pre-arranged vortex clouds. Whether the numerically calculated loads on the stationary airfoil agree with the experimental results depends on how closely the vortex passes the stationary airfoil because the present numerical model does not consider the possible separation caused by very close vortex interaction.

In Chapter 4 are contained the developments of the unsteady aeroelastic model and the feedback control laws for the flutter analysis and flutter suppression. Gravity is included in the equations of motion, the aerodynamic loads are calculated by using the aerodynamic model discussed in Chapter 2,

and the dynamics and aerodynamics are coupled and calculated simultaneously. A control surface is added at the trailing edge to suppress the flutter motion and the response to a wind gust. The control law and the servo equation are also coupled with the dynamics and aerodynamics, i.e. the airfoil, the wake, the elastic support and the control device are treated as one system, and all governing equations are solved simultaneously and interactively.

In Chapter 5 are presented the results of examples of flutter and flutter suppression by feedback control. The present numerical model accurately predicts the critical speed for the flutter motion. The effect of the static angle of attack on the critical flutter speed is investigated. The effect of a nonlinear elastic support is also studied. Some control laws are established, which can be used to suppress the flutter motion in certain ranges of static angle of attack and speed of the flow.

Finally in Chapter 6 some conclusions on the work of this dissertation are presented.

1.4.2 Contributions

1. The wakes of oscillating airfoils are accurately simulated by an inviscid model. This simulation gives support to the argument of Mathioulakis et al. (1985) and Wilder et al. (1990) that the evolution of the wake within a certain distance behind the airfoil is mainly controlled by an inviscid mechanism.

2. Blade-vortex interaction is investigated by actually simulating a wind tunnel experiment: a stationary airfoil is placed in or near the wake generated by another airfoil upstream. Some numerical results agree very well with the experimental results.

3. Gravity is included in the equations of motion for the study of flutter.

4. The effect of the static angle of attack on the critical flutter speed is investigated.

5. A control law is established, which can be used to suppress the oscillations of a flat-plate airfoil in certain ranges of static angle of attack and speed of the freestream.

6. The flowing air, the airfoil, the elastic support and the control devices are considered parts of a single dynamic system.

Chapter 2. Aerodynamic Model

There are several good models for attached unsteady flows past airfoils. Here the concentration is on a recent development based on panels of continuously varying vorticity. Any model of unsteady flow past an airfoil must predict both the rate at which vorticity is shed from the trailing edge into the wake and the way in which the shed vorticity is transported downstream. These features of the present model are described in this chapter. First the basic concepts and the governing equations are discussed. Then some simplifications, a panel method coupled with vortex dynamics, and the Kutta condition at the trailing edge of an airfoil are introduced. The method of calculating the aerodynamic loads on airfoils and the procedure for solving the problem are also presented. Finally, a test of the present model is given. The flowfield is considered two-dimensional in all that follows. Mracek and Mook (1988) developed a three-dimensional version of the present method.

2.1 Basic Concepts of Vortex Dynamics

The continuity equation for incompressible flows is

$$\nabla \cdot \vec{V} = 0 \tag{2.1.1}$$

where $\vec{V}$ is the velocity vector.

The vorticity is defined by the following equation

$$\vec{\Omega} = \nabla \times \vec{V} \tag{2.1.2}$$

When the flow is incompressible, Equation (2.1.2) can be inverted to give $\vec{V}$ as a function of $\vec{\Omega}$ (see, e.g., the general discussion of Sommerfeld, 1964, section IV. 20, more recent discussions by Wu and Thompson, 1973, and Wu and Sankar, 1980)

$$\vec{V}(\vec{r}, t) = \frac{1}{2\pi} \int_S \frac{\vec{\Omega}(\vec{r}_0, t) \times (\vec{r} - \vec{r}_0)}{|\vec{r} - \vec{r}_0|^2} \, dS(\vec{r}_0) + \vec{V}_\infty \tag{2.1.3}$$

where S is the entire region of interest (the entire vorticity-containing region), $\vec{r}_0$ is the position of the area element dS, $\vec{r}$ is the position where the velocity is being evaluated, t is the time, and $\vec{V}_\infty$ is the uniform velocity of the freestream. The derivation of Equation (2.1.3) is given in Appendix A.

Six important characteristics of the velocity field $\vec{V}$ are worth mentioning:

1. Equation (2.1.3) is an expression of the Biot-Savart law.

2. The region S includes the flowfield as well as the interiors of the objects in the flowfield, and the vorticity in those interiors is twice the angular velocity of these objects. More details are given in Section 2.3 and Appendix A.

3. It is noted that $\vec{\Omega}$ may be zero in large subregions of S and that $\vec{V}$, as given by Equation (2.1.3), is irrotational in these regions.

4. Vorticity anywhere in S creates velocity everywhere in S.

5. The velocity given by Equation (2.1.3) decays as the reciprocal of the distance from the vorticity-bearing subregions.

6. Equation (2.1.3) is a purely kinematic relationship; in deriving it, one does not need to make any assumptions regarding the velocity field other than $\vec{V}$ is single-valued and $\nabla \cdot \vec{V} = 0$. Consequently, Equation (2.1.3) is valid for "viscous" as well as "inviscid" flows.

In the model of attached unsteady flow past an airfoil, one postulates a priori that all the vorticity is in the following three subregions: a thin layer of fluid adjoining the surface of the airfoil, the wake (a free shear layer emanating from the trailing edge), and the interior of the airfoil itself. Thus, instead of having to integrate over the entire flowfield, one only needs to integrate over three relatively small subregions.

By using the vorticity-transport equation and the no-slip condition on the surfaces of the solid bodies, Wu and Sankar (1980) also obtained the following equation expressing the temporal conservation of "total vorticity" (i.e., circulation)

$$\frac{d}{dt} \int_S \vec{\Omega} \, dS = 0 \tag{2.1.4}$$

where the integral is carried out over the entire vorticity-containing region S, the same as the integral in Equation (2.1.3). Equation (2.1.4) is also valid for viscous as well as inviscid flows. The derivation of Equation (2.1.4) is given in Appendix A.

2.2 Boundary Layer Adjoining the Surface of the Airfoil

The flow in the layer adjoining the surface of the airfoil is accurately predicted by the boundary-layer theory, a theory that provides an asymptotic approximation for high Reynolds numbers to the solution of the Navier-Stokes equations. In boundary-layer theory, the pressure predicted by the outer (irrotational) flow on the surface of the airfoil appears as the driving (forcing) term in the governing equations and the tangential component of the velocity given by the outer flow at the surface of the airfoil appears in the boundary (matching) condition. Thus, according to this theory, the outer flow must be known before the flow in the boundary layer can be obtained. But it is also true that, if the flow (specifically the vorticity) is known in the boundary layer and wake and if the motion of the airfoil is known, the corresponding outer flow can be computed by means of Equation (2.1.3). The flow created by the vorticity disturbs the oncoming freestream in such a way that the no-penetration condition is satisfied by the resulting velocity field.

In the vorticity-panel approach, one first integrates Equation (2.1.3) across the thickness of the boundary layer, using the boundary-layer approximation for the vorticity, and then lets the boundary-layer thickness approach zero. The process reduces Equation (2.1.3) to the following

$$\begin{aligned}\vec{V}_b(\vec{r}\,,t) &= \frac{1}{2\pi}\int_{S_b}\frac{\vec{\Omega}(\vec{r}_0,t)\times(\vec{r}-\vec{r}_0)}{|\vec{r}-\vec{r}_0|^2}\,dS_b(\vec{r}_0)\\ &= -\frac{1}{2\pi}\vec{e}_z\times\oint_C\frac{\gamma[\ell(\vec{r}_0),t](\vec{r}-\vec{r}_0)}{|\vec{r}-\vec{r}_0|^2}\,d\ell(\vec{r}_0)\end{aligned} \tag{2.2.1}$$

where $\vec{V}_b$ is the velocity induced by the vorticity in the boundary layer, S_b is the region of the boundary layer, $\vec{e}_z$ is a unit vector perpendicular to the flowfield chosen so as to form a right-hand system with the base vectors in the plane

of the flow, the line integral is carried out along the contour of the airfoil C, ℓ is the distance along C measured from the lower trailing edge, and

$$\gamma(\ell, t)\vec{e}_z = \lim_{\substack{Re \to \infty \\ \delta \to 0}} \left[- \int_0^{\delta(\ell)} \vec{\Omega}(\ell, \vec{n}, t)\, dn \right] \tag{2.2.2a}$$

$$\gamma(\ell, t) = \lim_{\substack{Re \to \infty \\ \delta \to 0}} \left[\int_0^{\delta(\ell)} \frac{\partial u}{\partial n}\, dn \right] = u(\ell, 0^+, t) - u(\ell, 0, t) \tag{2.2.2b}$$

where Re is the Reynolds number, δ the thickness of the boundary layer, $\vec{n}$ is the unit outward-pointing vector on the contour of the airfoil C, and u is the velocity of the fluid relative to the surface of the airfoil.

Hence, the thin boundary layer is approximated as a bound vortex sheet of strength $-\gamma$ on the surface of the airfoil. If the no-slip condition is imposed on the surface, γ is the the tangential component of the velocity of the fluid next to the surface of the airfoil relative to the nearest point in the surface. The normal component of the relative velocity is zero if the no-penetration condition is satisfied.

The line integral in Equation (2.2.1) is evaluated first by dividing the contour of the airfoil into a number of short straight segments (see Figure 1) and then by approximating γ as a linear function of position along each element. The values of γ in adjoining elements are equal at the common point where the two are connected, the so-called node.

The calculation of the velocity induced by the vorticity on the individual elements is facilitated by introducing a local coordinate system. The origin of the local frame of reference for element i is placed at node i, the local x-axis runs along the element, and the local y-axis is points outward from the airfoil into the flowfield (see Figure 1). The transformations between the two frames are

$$\begin{Bmatrix} x \\ y \end{Bmatrix} = \begin{bmatrix} d_1 & d_2 \\ -d_2 & d_1 \end{bmatrix} \begin{Bmatrix} X - X_i \\ Y - Y_i \end{Bmatrix} \tag{2.2.3a}$$

$$\begin{Bmatrix} \vec{e}_x \\ \vec{e}_y \end{Bmatrix} = \begin{bmatrix} d_1 & d_2 \\ -d_2 & d_1 \end{bmatrix} \begin{Bmatrix} \vec{E}_X \\ \vec{E}_Y \end{Bmatrix} \tag{2.2.3b}$$

where (x, y) are the coordinates in the local frame with the base vectors $(\vec{e}_x, \vec{e}_y)$, (X, Y) are the coordinates in the global frame with the base vectors $(\vec{E}_X, \vec{E}_Y)$, and (X_i, Y_i) are the global coordinates of the node that serves as the origin of the local frame, and

$$\begin{aligned} d_1 &= (X_{i+1} - X_i)/\Delta\ell_i \\ d_2 &= (Y_{i+1} - Y_i)/\Delta\ell_i \end{aligned} \tag{2.2.4}$$

where

$$\Delta\ell_i = \sqrt{(X_{i+1} - X_i)^2 + (Y_{i+1} - Y_i)^2} \tag{2.2.5}$$

is the length of the element i.

The two linear basis functions

$$f_1(\xi) = 1 - \frac{\xi}{\Delta\ell_i} \tag{2.2.6a}$$

and

$$f_2(\xi) = \frac{\xi}{\Delta\ell_i} \tag{2.2.6b}$$

are used to describe γ on each element

$$\gamma(\xi, t)_i = G_i(t)\, f_1(\xi) + G_{i+1}(t)\, f_2(\xi) \tag{2.2.7}$$

where $0 \leq \xi \leq \Delta\ell_i$, G_i and G_{i+1} are the values of γ at nodes i and $i+1$, and $\Delta\ell_i$ is given by Equation (2.2.5).

From Equation (2.2.1), it follows that, in the local frame, the components of the velocity induced by the vorticity on a single element are given by

$$\begin{aligned}\vec{V}_{bi}(x, y, t) &= \frac{1}{2\pi}\int_0^{\Delta\ell_i} \frac{\gamma(\xi, t)_i[y\,\vec{e}_x - (x-\xi)\,\vec{e}_y]}{(x-\xi)^2 + y^2}\,d\xi \\ &= G_i\,[v_{1xi}\,\vec{e}_x + v_{1yi}\,\vec{e}_y] + G_{i+1}\,[v_{2xi}\,\vec{e}_x + v_{2yi}\,\vec{e}_y]\end{aligned} \tag{2.2.8}$$

where

$$\begin{aligned} v_{1xi} &= \frac{1}{2\pi\Delta\ell_i}\,[(\Delta\ell_i - x)\Delta\theta - 0.5y\ \ln R] \\ v_{1yi} &= \frac{1}{2\pi\Delta\ell_i}\,[y\Delta\theta - \Delta\ell_i + 0.5(\Delta\ell_i - x)\ \ln R] \\ v_{2xi} &= \frac{1}{2\pi\Delta\ell_i}\,(x\Delta\theta + 0.5y\ \ln R) \\ v_{2yi} &= \frac{1}{2\pi\Delta\ell_i}\,(\Delta\ell_i - y\Delta\theta + 0.5x\ \ln R) \end{aligned} \tag{2.2.9}$$

where

$$\Delta\theta = \tan^{-1}\left(\frac{x}{y}\right) - \tan^{-1}\left(\frac{x-\Delta\ell_i}{y}\right) \tag{2.2.10}$$

and

$$R = \frac{(x-\Delta\ell_i)^2 + y^2}{x^2 + y^2} \tag{2.2.11}$$

Using the inverse transformation of Equation (2.2.3) one can obtain the velocity induced by element *i* in terms of components in the global frame

$$\vec{V}_{bi}(X, Y, t) = G_i\,[V_{1Xi}\,\vec{E}_X + V_{1Yi}\,\vec{E}_Y] + G_{i+1}\,[V_{2Xi}\,\vec{E}_X + V_{2Yi}\,\vec{E}_Y] \tag{2.2.12}$$

where

$$\begin{Bmatrix} V_{kXi} \\ V_{kYi} \end{Bmatrix} = \begin{bmatrix} d_1 & -d_2 \\ d_2 & d_1 \end{bmatrix} \begin{Bmatrix} v_{kxi} \\ v_{kyi} \end{Bmatrix} \tag{2.2.13}$$

for $k = 1$ and 2.

2.3 Contribution to the Flowfield from the Rotation of Airfoils

According to the articles of Wu and Thompson (1973) and Wu and Sankar (1980), the motion of the airfoil also makes a contribution to the flowfield

$$\vec{V}_a(\vec{r}, t) = \frac{1}{2\pi} \oint_C \frac{(\vec{r} - \vec{r}_0)[\vec{v}_\ell(\vec{r}_0) \bullet \vec{n}(\vec{r}_0)] - [\vec{v}_\ell(\vec{r}_0) \times \vec{n}(\vec{r}_0)] \times (\vec{r} - \vec{r}_0)}{|\vec{r} - \vec{r}_0|^2} \, d\ell(\vec{r}_0) \tag{2.3.1}$$

where $\vec{V}_a$ is the flow velocity induced by the motion of the airfoil, $\vec{n}$ is the unit outward-pointing vector normal to the the contour of the airfoil C, $\vec{v}_\ell$ is the velocity of the fluid next to the surface, which is equal to the velocity of the airfoil at the same position according to the no-slip condition and no-penetration condition on the surface of the airfoil.

Wu and Thompson (1973) and Wu and Sankar (1980) also showed that Equation (2.3.1) can be rewritten as

$$\vec{V}_a(\vec{r}, t) = \frac{1}{2\pi} \vec{\Omega} \times \int_{S_a} \frac{\vec{r} - \vec{r}_0}{|\vec{r} - \vec{r}_0|^2} \, dS_a(\vec{r}_0) \tag{2.3.2}$$

where S_a is the interior of the airfoil, and

$$\vec{\Omega} = 2\vec{\omega}_a \tag{2.3.3}$$

where $\vec{\omega}_a$ is the angular velocity of the airfoil.

From Equation (2.3.3), one can see that the rotation of the airfoil only makes a contribution to $\vec{V}_a$ when $\vec{\omega}_a \neq 0$. This gives the explains why the region S in Equation (2.1.3) includes the flowfield as well as the interiors of any objects in the flowfield. Here S includes the flowfield S_f and the interior of the rotating airfoil S_a, i.e.,

$$S = S_f + S_a \tag{2.3.4}$$

To expedite the numerical calculations, Equation (2.3.1) is used instead of Equation (2.3.2). The derivations for Equations (2.3.1) and (2.3.2) are given in Appendix A.

2.4 Condition at the Trailing Edge and Vorticity-Shedding Rate

Next the trailing-edge condition is discussed. The Euler equation can be applied on the flow side of the bound vortex sheet, where viscous effects are ignorable, and written in terms of the relative velocity γ. The equation takes the following form

$$\frac{\partial \gamma}{\partial t} + \gamma \frac{\partial \gamma}{\partial \ell} + [\vec{a}_a + \dot{\vec{\omega}}_a \times \vec{r} + \vec{\omega}_a \times (\vec{\omega}_a \times \vec{r})] \bullet \vec{e}_\ell = -\frac{1}{\rho} \frac{\partial p}{\partial \ell} \tag{2.4.1}$$

where $\vec{r}$ is the position vector relative to the origin of the moving coordinate system fixed on the airfoil, $\vec{e}_\ell$ is the unit vector tangent to the contour in the direction of increasing ℓ, p is the pressure, ρ is the density of the fluid, $\vec{a}_a$ is the translational acceleration of the airfoil, and

$$\vec{\omega}_a = \dot{\theta}\,\vec{e}_z$$
$$\dot{\vec{\omega}}_a = \ddot{\theta}\,\vec{e}_z \tag{2.4.2}$$

are the angular velocity and acceleration of the airfoil respectively, where θ is the angle of rotation which is positive in the counterclockwise direction.

Integrating Equation (2.4.1) in the clockwise direction from the lower to the upper trailing edge and then equating the pressures on the upper and lower surfaces (no pressure discontinuity) at the trailing edge lead to

$$\frac{\gamma_L^2 - \gamma_U^2}{2} = \frac{d}{dt}\left[\oint_C \gamma(\ell, t)d\ell - 2\dot{\theta}S_b\right] = \frac{d\Gamma}{dt} \tag{2.4.3}$$

where the subscripts U and L denote quantities on the upper and lower surfaces at the trailing edge, respectively, $\oint_C \gamma d\ell$ is the relative circulation (i.e., circulation computed with the relative velocities) in the clockwise sense around the airfoil, S_a is the cross-section area of the airfoil and

$$\Gamma = \oint_C \gamma(\ell, t)d\ell - 2\dot{\theta}S_a \tag{2.4.4}$$

is the absolute circulation around the airfoil in the clockwise direction.

When the flow is unsteady, $\frac{d\Gamma}{dt}$ is not zero and the relative velocities on the upper and lower surfaces must be different. This difference is a manifestation of the vortex sheet (wake) that must form there in an unsteady flow.

It follows from Equation (2.1.4) that

$$\frac{d}{dt}(\Gamma + \Gamma_w) = \frac{d\Gamma}{dt} + \frac{d\Gamma_w}{dt} = 0 \tag{2.4.5}$$

where Γ_w is the circulation around the wake, and

$$\Gamma + \Gamma_w = Constant \tag{2.4.6}$$

is the total circulation in the flowfield.

Then it follows from Equations (2.4.3) and (2.4.5) that

$$\frac{d\Gamma_w}{dt} = -\frac{d\Gamma}{dt} = \frac{\gamma_U^2 - \gamma_L^2}{2} \tag{2.4.7}$$

where $\frac{d\Gamma_w}{dt}$ is often called the vorticity-shedding rate. Vorticity is shed from the airfoil and added to the wake as described by Equation (2.4.7).

To determine the vorticity-shedding rate, an understanding of the flowfield in the immediate neighborhood of the trailing edge is very important. For unsteady flows, Giesing (1969) analyzed the kinematic characteristics around the trailing edge by the conformal-mapping method. Based on the assumption that the mean velocity at the trailing edge is finite and non-zero, he showed that the vortex sheet was shed parallel to the upper or lower surface of the trailing edge depending on the direction of the shed vorticity. Maskell (1971) came to the same conclusion later. But Basu and Hancock (1978) pointed out that the Giesing/Maskell model can not reach the steady case as $\frac{d\Gamma}{dt}$ in Equation (2.4.7) goes to zero because the stagnation streamline bisects the angle of a wedge-shaped trailing edge in the steady case. They argued without proof that, as $\frac{d\Gamma}{dt} \rightarrow 0$, the curvature of the streamline emanating from the trailing edge tends to infinity.

The flow in the trailing-edge region has also been studied experimentally. Studies by Poling and Telionis (1986, 1987) and the thesis of Poling (1985) contain extensive reviews of earlier work. In their experiment, Poling and Telionis released dyes of different colors into the upper-surface and lower-surface boundary layers on a NACA 0012 airfoil oscillating in pitch. For reduced frequencies in the range considered here, they observed that during most of the downstroke, the shear layer emanating from the trailing edge had

the color of the lower-surface boundary layer while a pool of the color of the upper-surface boundary layer formed on the upper surface at the trailing edge. The observations support the Giesing/Maskell model of trailing-edge flow. More recently, Liu et al. (1990) studied the flow in the trailing-edge region. In this experiment, they placed a rotating ellipse downstream from and below the trailing edge of a fixed NACA 0012 airfoil. They observed the unsteady flow near the trailing edge of the fixed airfoil, and also concluded that the model described above is realistic.

The present simulation of the flowfield in the region of the the trailing edge is based on the Giesing/Maskell model. As illustrated in Figure 2, the flow at the trailing edge has the following characteristics:

1. When $\frac{d\Gamma}{dt} > 0$, $\gamma_L \neq 0$ and $\gamma_U = 0$; the streamline (for the velocity field relative to the moving airfoil) along the lower surface of the airfoil leaves the airfoil smoothly (i.e., tangent to the lower surface), and its counterpart along the upper surface has a sharp corner at the trailing edge (i.e., the relative velocity along the upper surface is zero at the trailing edge).

2. When $\frac{d\Gamma}{dt} < 0$, $\gamma_L = 0$ and $\gamma_U \neq 0$; the flow relative to the airfoil comes smoothly off the upper surface and contains a stagnation point on the lower surface at the trailing edge.

In the present numerical model, the values of the relative velocity on both the upper and lower trailing edge (γ_U and γ_L) are not directly calculated. Instead, a point vortex of circulation Γ_t is placed at the trailing edge to approximately represent the non-zero, linearly distributed relative velocity given by Equation (2.2.7) on either the upper or the lower surface at the trailing edge (refer to Figure 3). The relationship between Γ_t and the relative velocities is given by

$$\Gamma_t = \int_0^{\Delta\ell_U} \gamma_U f_2(\xi) d\xi = \frac{\gamma_U \Delta\ell_U}{2} \qquad \gamma_L = 0 \ , \qquad \text{for} \quad \Gamma_t > 0 \qquad (2.4.8a)$$

$$\Gamma_t = \int_0^{\Delta\ell_L} \gamma_L f_1(\xi) d\xi = \frac{\gamma_L \Delta\ell_L}{2} \qquad \gamma_U = 0 \ , \qquad \text{for} \quad \Gamma_t < 0 \qquad (2.4.8b)$$

where $\Delta\ell_U$ and $\Delta\ell_L$ are the panel lengths on the upper and lower surfaces at the trailing edge, respectively.

Then γ_U and γ_L are

$$\gamma_U = \frac{2\Gamma_t}{\Delta\ell_U} \qquad \gamma_L = 0 \ , \qquad \text{for} \quad \Gamma_t > 0 \qquad (2.4.9a)$$

$$\gamma_L = \frac{2\Gamma_t}{\Delta\ell_L} \qquad \gamma_U = 0 \ , \qquad \text{for} \quad \Gamma_t < 0 \qquad (2.4.9b)$$

It follows from Equation (2.4.7) that the vorticity shed into the wake during the time interval Δt is given by

$$\Delta\Gamma_w = \frac{2\Gamma_t^2}{\Delta\ell_U^2} \Delta t \qquad \text{for} \quad \Gamma_t > 0 \qquad (2.4.10a)$$

$$\Delta\Gamma_w = -\frac{2\Gamma_t^2}{\Delta\ell_L^2} \Delta t \qquad \text{for} \quad \Gamma_t < 0 \qquad (2.4.10b)$$

Hsu and Wu (1986, 1988) developed an alternative to the above model of the trailing-edge flowfield. They concluded that the trailing-edge flow does not have to be tangent to one of the surfaces by applying the momentum equation over a small control volume at the trailing edge. However, in arriving at their conclusion, they did not impose Equation (2.4.7). When Equation (2.4.7) is imposed, the two models of the trailing-edge flowfield agree.

For the potential flow past infinitesimally thin boundary layers, it is noted that, if the trailing-edge streamline is above the trailing-edge wedge, the speed

along the lower-surface streamline is infinite at the trailing edge and there is still a stagnation point on the upper-surface streamline.

When the reduced frequency is higher, the present model does not seem to be adequate. It appears that the vorticity being shed from the trailing edge is strong enough to create a stagnation point on the surface, slightly away from the trailing edge. And, in fact, Ohashi and Ishikawa (1972) observed such a flowfield experimentally. Such a flowfield can also develop at the instant following an impulsive start. Moreover, the present simulation also predicts a stagnation point close to, but not at, the trailing edge both for the instant after an impulsive start and during cyclic motion when the reduced frequency is greater then five.

Doing their experiment in air, Ohashi and Ishikawa (1972) placed thin paper containing a solution of Nessler reagent on one side of the trailing edge and released ammonia gas into the boundary layer on the other side. The reagent changed color during the motion, indicating that it came in contact with the ammonia and suggesting that the flow turned the corner instead of coming off the surface smoothly. However, the reduced frequency and the amplitude had to exceed certain limits before the paper changed color. For amplitudes and frequencies below the limits, the observations of Ohashi and Ishikawa also appear consistent with the Giesing/Maskell model used in the present work.

2.5 Discretization of Wakes

The simulation of the wake is considered next. Ideally, the wake should be modelled as a continuous vortex sheet emanating from the trailing edge with the circulation being added according to (2.4.7). However, the sheet wraps around and rolls up while stretching. In fact, it seems that a discontinuity in the curvature appears. This is a process that is difficult to simulate with a

continuous sheet (Rosenhead, 1931). Actually, the evolution of vortex sheets is accompanied by the problem of instability. A linear stability analysis (Krasny, 1986) of the partial differential equation describing the motion of a vortex sheet showed that the shorter the wave of a disturbance is, the faster the disturbance grows (known as Kelvin-Helmholtz instability). Extensive work on this subject has been presented in the articles by Meiron et al. (1982), Moore (1979, 1984), Pozrikidis and Higdon (1985), Caflisch (1988), Aref et al. (1988), and many others.

An alternative to the continuous vortex sheet as a model of the wake is the system of point vortices or vortex blobs. Then the circulation around the wake, Γ_w, is the sum of the circulations around the individual vortices

$$\Gamma_w = \sum_{k=1}^{M} \Gamma_k \tag{2.5.1}$$

where M is the number of vortices in the discretized wake, and Γ_k is the circulation of vortex k.

The use of point vortices was first proposed by Rosenhead (1931), though this concept was introduced by Helmholtz (1858). The system of point vortices is not without a major problem of its own: eventually two vortices are convected close to each other, and then, as a result of the singularity in the expression (Biot-Savart law) for the velocity field generated by a point vortex, at the next time step they are convected very far apart. As Krasny (1988) pointed out the discrete model is not stable because of the Kelvin-Helmholtz instability and computer round-off error, and that this can be overcome by smoothing (removing) the singularity of point vortices.

One of the methods to correct this irregular, seemingly chaotic behavior involves the concept of a vortex blob (see, e.g., Chorin and Bernard, 1973; Leonard, 1980; and Spalart, 1988). The vortex blob distributes the vorticity of

a point vortex over a small, but finite, circular core by means of a so-called core function and thereby eliminates singularities. In the present numerical calculations, the following core function is used

$$F(d) = \frac{d^2}{1 + d^2} \tag{2.5.2a}$$

where

$$d = \frac{|\vec{r} - \vec{r}_k|}{\sigma} \tag{2.5.2b}$$

where σ is the small radius of the vortex blob, $\vec{r}$ represents the point in the flowfield where the velocity is being calculated, and $\vec{r}_k$ represents the point where the vortex is located. With the discrete form of Equation (2.1.3) and the core function described in Equation (2.5.2), the velocity induced by the wake is approximated by

$$\begin{aligned} \vec{V}_w(\vec{r}, t) &= -\frac{1}{2\pi}\, \vec{e}_z \times \sum_{k=1}^{M} \Gamma_k F(d)\, \frac{\vec{r} - \vec{r}_k}{|\vec{r} - \vec{r}_k|^2} \\ &= -\frac{1}{2\pi}\, \vec{e}_z \times \sum_{k=1}^{M} \Gamma_k \frac{\vec{r} - \vec{r}_k}{|\vec{r} - \vec{r}_k|^2 + \sigma^2} \end{aligned} \tag{2.5.3}$$

where clockwise is taken as the positive direction of Γ_k. Vortex blobs cannot induce velocity on themselves.

However, this approach is not entirely satisfactory: Vortex blobs collect in some regions and separate in others [refer to part (a) of Figure 7]; the result can be a very uneven spatial distribution and, consequently, a very poor representation of the wake. The numerical phenomenon corresponds to the physical stretching and coiling of the actual vortex sheet. The vortex-blob simulation of the continuous vortex sheet can only be improved by splitting the

vortices as they begin to separate (see, e.g., Mook et al., 1987, 1989). Splitting is used in the present model and discussed below.

The wake is viewed as a free shear layer in an inviscid fluid. Associated with each element of its length are mean values of thickness (averages over the elemental lengths) and circulation (averages over the cross-section areas associated with the elemental lengths). For each element of the wake in a barotropic, two-dimensional, inviscid flow

$$\frac{D}{Dt}(\Omega \delta A) = \frac{D}{Dt}(\delta \Gamma) = 0 \tag{2.5.4}$$

and, when the flow is incompressible,

$$\frac{D}{Dt}(\delta A) = 0 \quad \text{and} \quad \frac{D\Omega}{Dt} = 0 \tag{2.5.5}$$

where $\frac{D}{Dt}(\,)$ is the substantial derivative, δA is the cross-section area of the element of the wake, Ω is the mean value of the vorticity associated with that element, and $\delta \Gamma$ is the circulation around that element.

When a system of discrete vortices is used to imitate the wake, each point vortex (or vortex blob) approximates one of the elemental lengths of the free shear layer, and the value of the circulation around an individual vortex is the $\delta \Gamma$ of the corresponding elemental length. In other words, each circulation in the system of discrete vortices represents an elemental length of the free shear layer that imitates the actual wake.

When the vortex sheet stretches, its thickness decreases while its length increases [in such a way that $\frac{D}{Dt}(\delta A) = 0$] and $\delta \Gamma$ remains constant. In the system of discrete vortices, stretching is manifested when two sequentially shed vortices increasingly separate as they convect. If the elemental lengths are to remain approximately uniform as the wake stretches, then more elemental lengths will be needed to represent the stretched portion of the free

shear layer. The addition of more elemental lengths corresponds to the addition of more discrete vortices to the system.

As illustrated in part (a) of Figure 4, whenever two successively shed vortices are convected apart by a distance greater than a specified critical length, they are split into three. The new vortex has the circulation equal to one third of the sum of the circulations of the original two and is placed at the midpoint between them. The circulations around the original two vortices are reduced to two thirds of their original values. The above procedure is repeated at each time step until no two successive vortices are farther apart than the critical distance.

When two vortices are convected very close, they are combined. The new vortex has circulation equal to the sum of the circulations of the original two and is placed at the centroid of the original two (Spalart, 1988) as shown in part (b) of Figure 4. Vortices having circulations of different signs are not combined.

Sarpkaya and Schoaff (1979) proposed a scheme in which the vortices are repositioned in order to achieve uniform spacing and the circulations are redistributed in order to maintain (approximately) the spatial distribution. However, because no more vortices are added (i.e., there is no splitting), this approach does not adequately account for stretching.

Pozrikidis and Higdon (1985) simulated the evolution of thick shear layers of uniform vorticity. They expressed the velocity field generated by the vortex layer as a line integral, which they evaluated numerically. The computed velocity field was used to determine the displacements of so-called marker points on the boundary of the vorticity-bearing region. Then the velocity field was recomputed, etc. Some of their results show the shear layers forming regions similar to the vortical structures obtained in the present simulation.

However, in their results the regions resembling the vortical structures have uniform vorticity instead of the spatial variation the present results provide.

2.6 Aerodynamic Loads

For the 2-D problem considered here, the pressure distribution on the surface on the airfoil can be obtained by integrating Equation (2.4.1) from the lower trailing edge

$$p(\ell) - p_t = -\rho \left\{ \frac{d}{dt} \int_0^{\ell} \gamma d\ell + \frac{\gamma(\ell)^2 - \gamma_L^2}{2} + \int_0^{\ell} [\vec{a}_a + \dot{\vec{\omega}}_a \times \vec{r} + \vec{\omega}_a \times (\vec{\omega}_a \times \vec{r})] \bullet \vec{e}_\ell \, d\ell \right\} \tag{2.6.1}$$

where p_t is the pressure at the trailing edge. It is not necessary to know p_t in the calculation of the aerodynamic loads because p_t is only a function of time and the the aerodynamic loads are obtained by integrating the pressure around the closed contour of the airfoil.

According to Equation (2.6.1), the pressure on the surface is a function of the relative surface velocity and the motion of the airfoil. Integrating Equation (2.6.1) from the lower trailing edge to the upper trailing edge leads to Equation(2.4.3).

If the airfoil is a flat plate, the pressure difference across the plate at any point, Q (as shown in Figure 5), can be obtained by integrating Equation (2.4.1) in the clockwise direction from this point on the lower surface (Q_{lower}), passing the leading edge, and back to this point on the upper surface (Q_{upper}). The integral has the form of

$$\int_{Q_{lower}}^{Q_{upper}} (\quad)\, d\ell \tag{2.6.2}$$

and the path of this integral is shown in Figure 5.

Because the vector $\vec{e}_\ell$ in Equation (2.4.1) takes the opposite directions on the lower and upper surfaces, one has

$$\int_{Q_{lower}}^{Q_{upper}} [\vec{a}_a + \dot{\vec{\omega}}_a + \vec{\omega}_a \times (\vec{\omega}_a \times \vec{r})]\, d\ell = 0 \tag{2.6.3}$$

for the case of a flat plate.

In addition, $\gamma(\ell)$ calculated by the present numerical model is the difference between the velocities on the upper and lower surfaces (the flat plate is treated as a vortex sheet), ℓ is redefined as the measurement from the trailing edge ($\ell = 0$) to the leading edge ($\ell = \ell_{lea.}$). Then the pressure difference is

$$\Delta p(\ell) = p_{upper} - p_{lower} = -\rho\,(\gamma_M \gamma + \frac{\partial}{\partial t} \int_{\ell}^{\ell_{lea.}} \gamma\, d\ell) \tag{2.6.4}$$

where γ_M is the mean value of the upper and lower relative surface velocities, and can be calculated by

$$\gamma_M = (\vec{V}_\infty + \vec{V}_w - \vec{v}_\ell) \bullet \vec{\tau} \tag{2.6.5}$$

where $\vec{V}_\infty$ is the velocity of the freestream, $\vec{V}_w$ is the velocity induced by the wake, $\vec{v}_\ell$ is the velocity of the plate, and $\vec{\tau}$ is the unit vector tangent to the flat airfoil pointing toward the trailing edge. In Equation (2.6.5), there is no contribution due to the vortex sheet (representing the flat plate) because this sheet is a straight line segment. If this vortex sheet is curved, its contribution must also be considered.

It is important to mention here that there is a singularity at the leading edge of the flat airfoil, so there is a suction force $-F_S\vec{\tau}$ there pointing away from the leading edge as shown in Figure 5. As described in detail in Appendix B, this force can be obtained by the conformal-mapping method and its magnitude is given by the following

$$F_S = \frac{\rho b \pi}{8}\left[2V_\infty \sin\alpha_{ins} + \frac{\Gamma}{b\pi} + \frac{2}{b\pi}\sum_{k=1}^{M}\frac{\Gamma_k(1+\xi_k)}{(1+\xi_k)^2+\eta_k^2}\right]^2 \qquad (2.6.6)$$

where b is the half chord of the flat airfoil, α_{ins} is the instantaneous angle of attack with respect to the freestream, Γ in the circulation around the airfoil, Γ_k is the circulation around the k^{th} vortex at the position $z_k = x_k + iy_k$ in the wake, $\xi_k + i\eta_k = (z_k + \sqrt{z_k^2 - b^2})/b$, and $i = \sqrt{-1}$.

2.7 Equations for the Unknowns and Numerical Procedures

If the contour of the airfoil C is approximated by N panels, then there are $N+1$ nodes with the lower trailing edge being numbered 1 and the upper trailing edge $N+1$. The element size is nonuniform in the present method, the elements near the leading and trailing edges being smaller than those in the mid-chord region. The approximation of the very last portion of γ by a vortex becomes more accurate as the panel adjoining the trailing edge becomes smaller. The number of elements in Figure 1 is 18, but all the present results were computed with 36 or more.

Because the vorticity over either the first or the last element is concentrated in a vortex of circulation Γ_t at the trailing edge [refer to Equation (2.4.8)], G_1 and G_{i+1} are both zero. In other words, the vortex of circulation Γ_t at the trailing edge accounts for the fact that either γ_U or γ_L is nonzero, depending on the sign of $\frac{d\Gamma}{dt}$ [recall that γ_U and γ_L are given by Equation (2.4.9)]. The

values of the relative surface velocity at each node, except the trailing edge, G_i, and the circulation of the vortex at the trailing edge Γ_t are together N unknowns.

With Equation (2.2.7), the relative circulation around the airfoil appearing in Equation (2.4.3) is approximated as

$$\oint_C \gamma \, d\ell = \frac{1}{2} \sum_{i=1}^{N} (G_i + G_{i+1}) \Delta\ell_i + \Gamma_t \tag{2.7.1}$$

where N is the number of elements on the contour of the airfoil, $\Delta\ell_i$ is given by Equation (2.2.5) and $G_1 = G_{N+1} = 0$.

According to Equation (2.2.1), the velocity induced by the bound vortex sheet on the surface of the airfoil is approximated as

$$\vec{V}_b = \sum_{i=1}^{N} \vec{V}_{bi} - \frac{1}{2\pi} \vec{e}_z \times \frac{\Gamma_t (\vec{r} - \vec{r}_t)}{|\vec{r} - \vec{r}_t|^2} \tag{2.7.2}$$

where $\vec{V}_{bi}$ is given by Equation (2.2.12) with $G_1 = G_{N+1} = 0$.

The total velocity in the flowfield is

$$\vec{V} = \vec{V}_b + \vec{V}_a + \vec{V}_w + \vec{V}_\infty \tag{2.7.3}$$

where $\vec{V}_b$, $\vec{V}_a$, $\vec{V}_w$ are respectively given by Equations (2.7.2), (2.3.1) and (2.5.3), and $\vec{V}_\infty$ is the velocity of the freestream.

It follows from Equations (2.4.6), (2.4.4), (2.7.1) and (2.5.1) that

$$\frac{1}{2} \sum_{i=1}^{i=N} (G_i + G_{i+1}) \Delta\ell_i + \Gamma_t - 2\dot{\theta} S_a + \sum_{k=1}^{M} \Gamma_k = \textit{Constant} \tag{2.7.4}$$

This equation is the principle of the total vorticity conservation in the flowfield, and is linear in the G_i and Γ_t.

The no-penetration condition on the surface of the airfoil is

$$(\vec{V} - \vec{v}_\ell) \bullet \vec{n} = 0 \tag{2.7.5}$$

where $\vec{V}$ is given by Equation (2.1.3) or (2.7.3), $\vec{v}_\ell$ is the velocity of the airfoil, and $\vec{n}$ is a vector normal to the contour of the airfoil.

Equation (2.7.5) is applied at the control point of each element (in the present model, control points are the midpoints of the elements as shown in Figures 1 and 3). Then the number of linear equations for the G_i and Γ_t that result from applying (2.7.5) is N. With Equation (2.7.4) which is the constraint on the circulation around both the airfoil and its wake, there are a total of $N + 1$ linear equations for N unknowns. Consequently, an optimal solution is obtained by minimizing the sum of the squares of the errors at the control points subject to the equality constraint [Equation (2.7.4)] imposed on the circulation. For the case of the flat plate, this is not needed because the number of equations matches the number of unknowns.

If there are more than one airfoil in the flow, Equation (2.7.5) should be applied on the surface of each airfoil, and the left-hand side of Equation (2.7.4) should be the circulation around the entire flowfield.

At every time t_k , a vortex with circulation $\Gamma_k = \Delta\Gamma_w$ is released from the trailing edge into the wake. The discrete vortices in the wake are convected at the local particle velocity while their strengths (circulations) remain unchanged. The procedure produces a continuous pressure field in an inviscid fluid; thus, the wake is modelled as a region that contains vorticity where viscous effects are ignorable. During the time interval Δt , the change in the position of a vortex is given by

$$\Delta\vec{r} = \vec{V}\Delta t \tag{2.7.6}$$

The numerical procedure can be summarized as follows:

1. The initial flow is specified. As examples, the flow may be steady for some specified angle of attack, or the fluid may be at rest, or the flow may start from a previously calculated unsteady condition.

2. The time is advanced one step.

3. The wake is convected and the splitting/combining procedure is implemented.

4. The position and velocity of the airfoil are computed from the prescribed motion.

5. The values of γ at the nodes and Γ_t are computed from the constrained-optimization scheme.

6. If desired, pressure and loads are computed.

7. The computation is returned to step 2.

To check the convergence of this method as the number of elements taken on the contour of the airfoil and the size of the time-step are varied, an impulsively started flow around an NACA 0012 airfoil at 10° angle of attack is tested by calculating the velocities at the trailing edge and the circulation around the wake at time $t = 1$. For such a case, the relative velocity at the upper trailing edge $\gamma_U = 0$ and the relative velocity at the lower trailing edge $\gamma_L \neq 0$.

In Table 1, the values of the relative velocity at the trailing edge, γ_L, at time $t = 1$ are listed for different sizes of the time step, Δt, and different numbers of elements, N.

Table 1. The velocity at the trailing edge as a function of the time step, Δt , and the number of elements, N

Δt	$N = 36$	$N = 72$	$N = 108$	$N = 144$
0.02	-0.4736			
0.01	-0.4762	-0.4801		
0.005	-0.4788	-0.4824	-0.4840	
0.0025	-0.4796	-0.4840	-0.4856	-0.4864
0.00125	-0.4800	-0.4846	-0.4865	-0.4876
0.000625	-0.4802	-0.4849	-0.4896	-0.4881

In Table 2, the values of the circulation around the wake, Γ_w, at time $t = 1$ are listed for different sizes of the time step, Δt, and different number of elements, N.

Table 2. The circulation around the wake a function of the time step, Δt , and the number of elements, N

Δt	$N = 36$	$N = 72$	$N = 108$	$N = 144$
0.02	-0.4819			
0.01	-0.4735	-0.4727		
0.005	-0.4678	-0.4660	-0.4753	
0.0025	-0.4653	-0.4620	-0.4711	-0.4764
0.00125	-0.4641	-0.4601	-0.4686	-0.4736
0.000625	-0.4635	-0.4592	-0.4674	-0.4722

The blank boxes in Table 1 and Table 2 indicate that the size of the time-step is too large to use with the corresponding number of elements. The smaller the elements are (the larger N is), the smaller the time step must be to obtain reasonable results. As Δt decreases by being cut in half, γ_L and Γ_w have only

slight changes. And for the same time step, the results obtained by using different numbers of elements are close. The present method gives convergent solutions as the number of the elements increases and the size of the time step decreases.

2.8 Summary

A two-dimensional aerodynamic model is developed, which is based on a vorticity-panel method and coupled with vortex dynamics. The vorticity is concentrated in the thin boundary layer, the wake, and the interior region of the rotating airfoil. The velocity in the flowfield induced by the vorticity is given by the Biot-Savart law. The thin boundary layer is approximated as a vortex sheet, and a vorticity-panel method is used to solve for the surface velocity on the airfoil. The wake is approximated as a system of discrete vortices. The rate at which the vorticity is shed into the wake is decided. The vortices in the wake are convected at the local velocity of the fluid. The method of computing the pressure on the airfoil is discussed, and there is a suction force acting at the leading edge of a flat airfoil. Some numerical tests show that the present aerodynamic model converges when the length of panels and the size of time steps decrease.

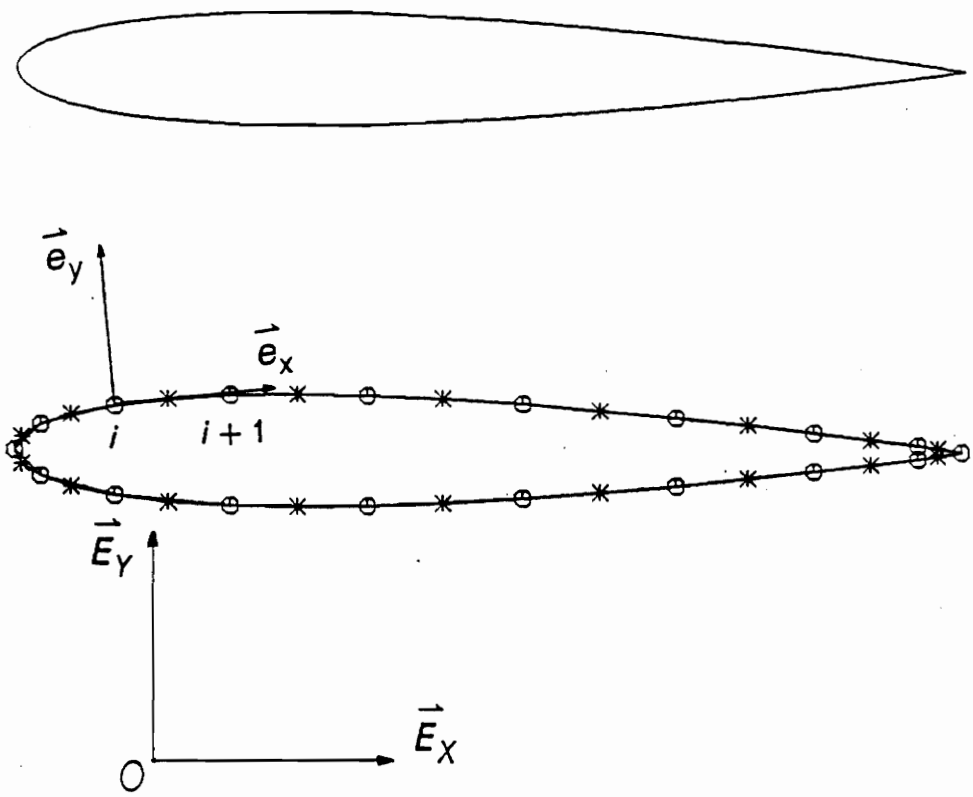

Figure 1. Airfoil and the coordinate systems: (a) before discretization; (b) after discretization. O represents a node point (where two panels join) and * is a control point (where the no-penetration condition is imposed). The spacing is nonuniform; smaller panels are used near the leading and trailing edge. $(\vec{e}_x, \vec{e}_y)$ are base vectors in the local frame, and $(\vec{E}_X, \vec{E}_Y)$ are those in the global frame.

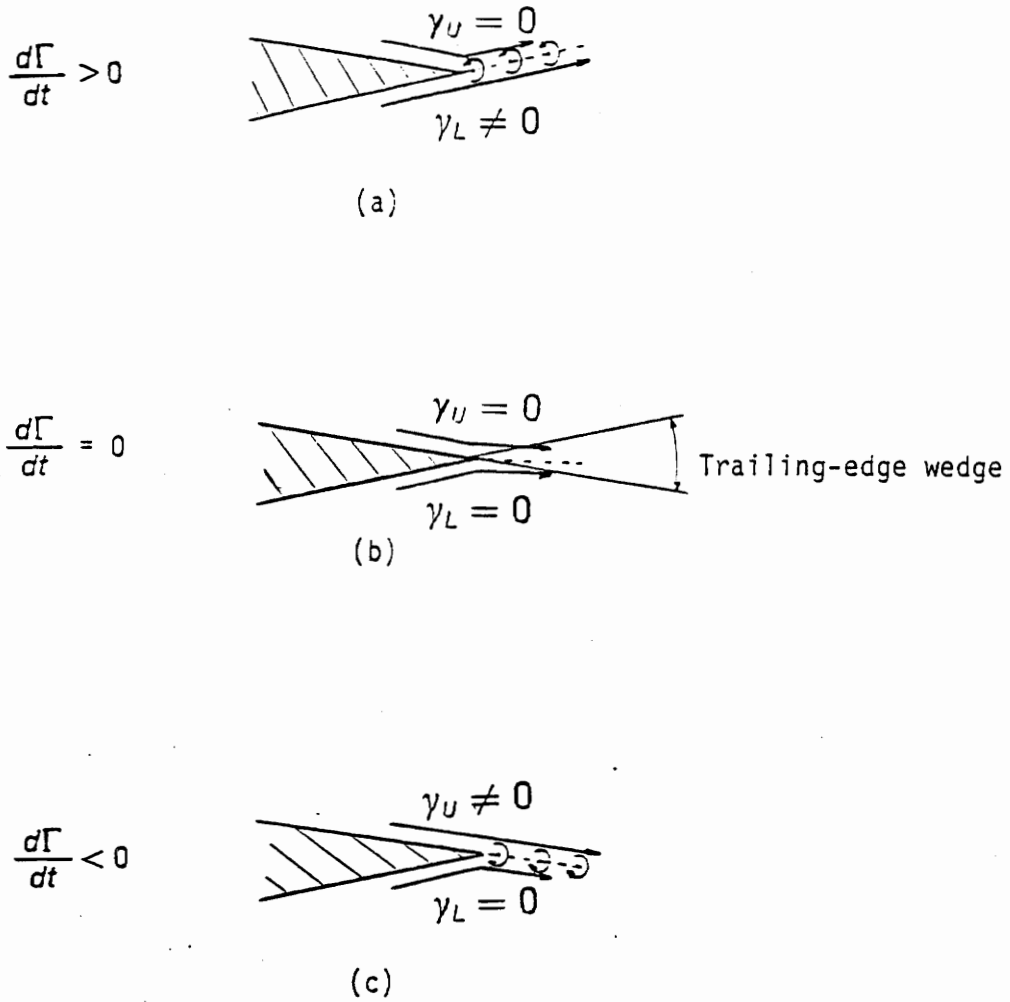

Figure 2. Physical model of the trailing-edge flow used in the numerical simulation: (a) clockwise circulation (Γ) around the airfoil is increasing; (b) the flow is steady; (c) clockwise circulation is decreasing. The direction of the vorticity being shed is indicated on the trailing-edge streamline. γ_U and γ_L refer to the relative velocities on the upper and lower surfaces at the trailing edge. The trailing edge streamline lies either on or within the trailing-edge wedge.

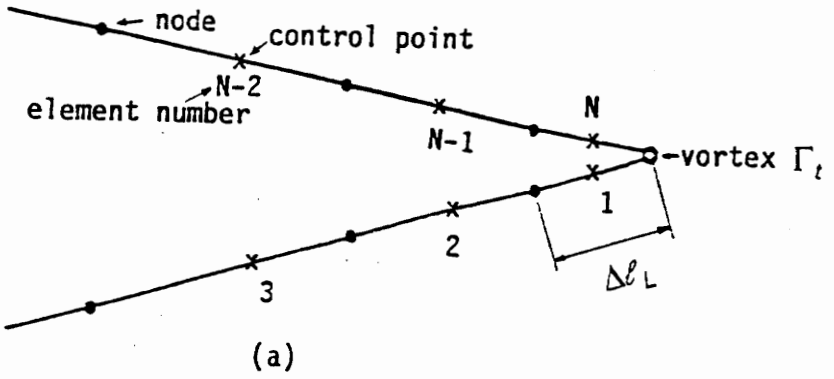

(a)

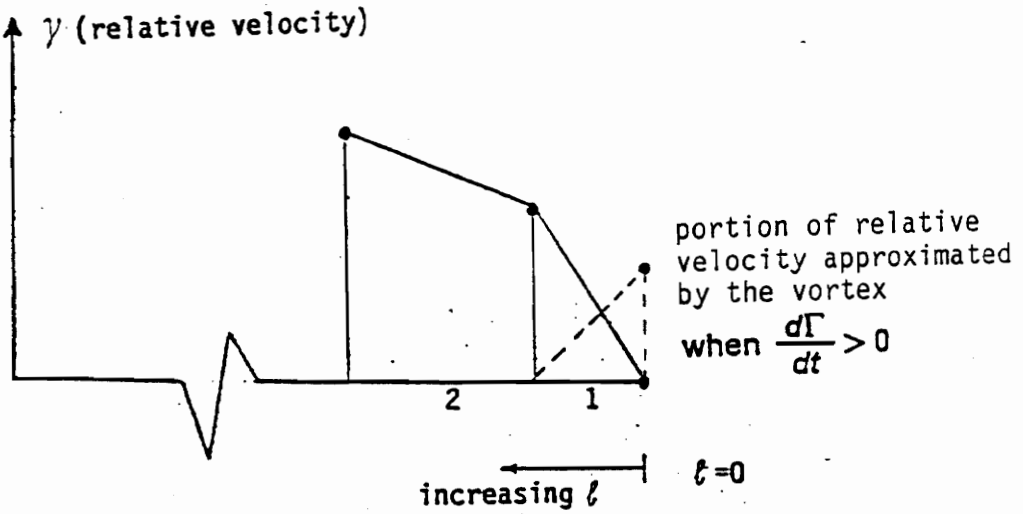

(b)

Figure 3. Numerical model of the trailing edge: (a) a vortex of circulation Γ_t is placed exactly on the trailing edge; (b) the piecewise linear continuous velocity distribution. For the case shown, $\frac{d\Gamma}{dt} > 0$ (Γ is the clockwise circulation around the airfoil), $\Gamma_t = \frac{1}{2}\gamma_L \Delta\ell_L$.

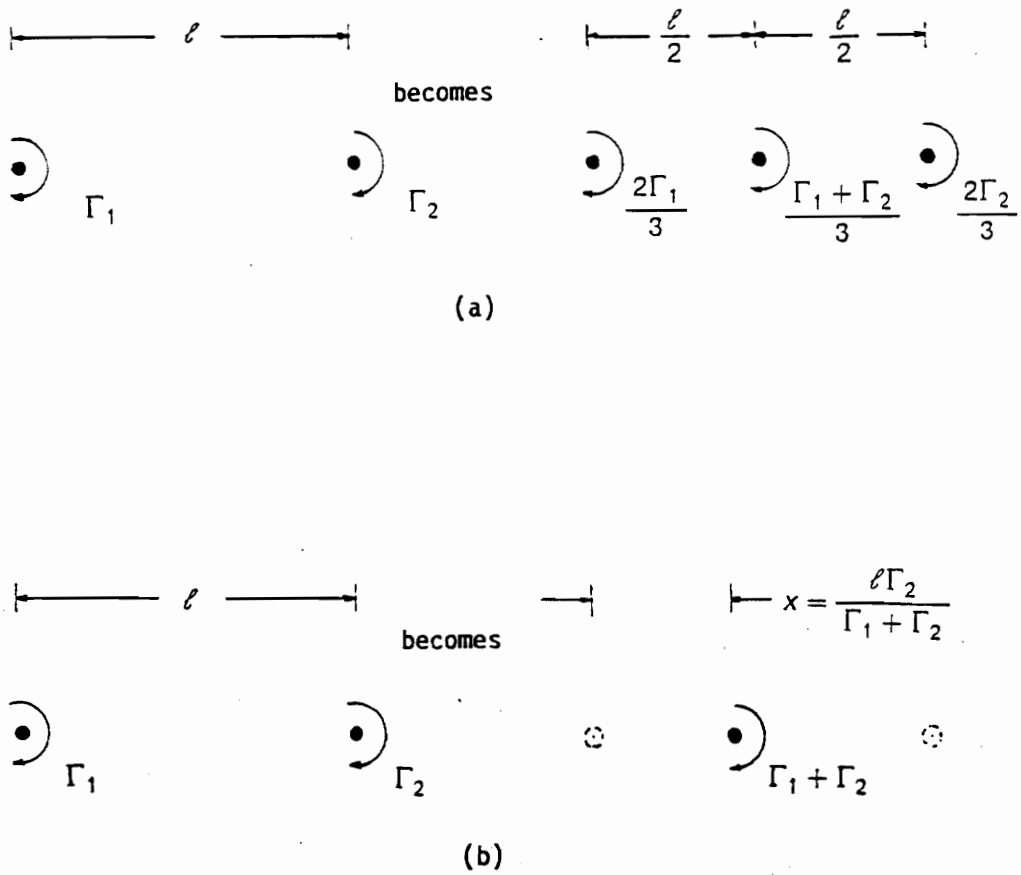

Figure 4. Splitting and combining schemes: (a) the original two vortices with circulations Γ_1 and Γ_2 separated by the distance ℓ, which is greater than a critical length for splitting, are divided into three vortices as indicated; (b) the original two vortices with circulations Γ_1 and Γ_2 separated by the distance ℓ, which is less than a critical length for combining, are merged into a single vortex as indicated.

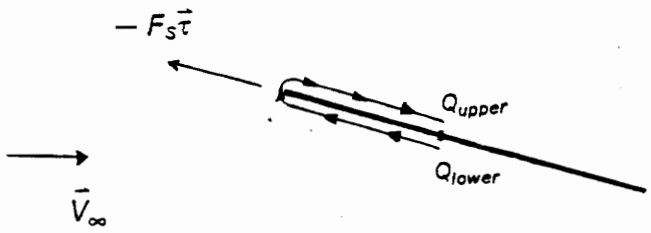

Figure 5. Integral path over a flat-plate airfoil.

Chapter 3. Examples of Numerical Simulations of Wakes and Blade-Vortex Interaction

In this section, some examples of numerical simulations of wakes and blade-vortex interaction are presented. In all calculations unless otherwise stated, NACA 0012 airfoils are used, and all variables have been nondimensionalized by the freestream speed, V_∞, and the chord length, C, of the airfoil.

3.1 Wakes of Airfoils

An airfoil pitching around its fixed quarter-chord point is represented in Figure 6. The pitch angle, θ_p (degrees), is given by

$$\theta_p = -10^\circ \cos(2kt) \tag{3.1.1}$$

where $k = \omega C/2V_\infty$ is the reduced frequency and ω is the dimensional frequency. As shown in Figure 6, the pitch angle θ_p is positive in the clockwise direction. Initially, the flow around the airfoil is steady. As soon as the pitching starts, the motion becomes unsteady and vorticity starts to shed from the trailing edge.

First the reduced frequency is chosen as $k = 2.77$, so that the present results can be compared with some experimental results. In Figure 7, the wake after one and a quarter cycles of pitching is shown. Each dot in the wake region gives the location of a vortex. In part (a) of Figure 7 the splitting and combining procedures are not used, and there are 250 vortices in the wake after 250 time steps. In part (b) of Figure 7, the splitting and combining procedures are used for the same time step used in part (a). The vortices are split (by using a critical length related to the shortest panel on the airfoil) and combined at each time step, and there are 512 vortices in the wake after 250 time steps. In part (c) of Figure 7, a smaller critical length for splitting is used, and there are 3818 vortices. Comparing the three wakes, one sees that the large-scale structures of the wake are about the same, but the splitting procedure provides more details. These results clearly show a strong trend to converge, which is typical of all cases treated by the present method.

The dark regions in parts (b) and (c) of Figure 7, which contain many vortices, are called regions of concentrated vorticity in this dissertation. The points in parts (b) and (c) of Figure 7 are not connected; however, they are so densely packed that the representation of the wake appears to be continuous.

The physical mechanism causing the regions of concentrated vorticity to form is illustrated in Figure 8. In part (a) an undisturbed sheet of clockwise vorticity is represented. in part (b) a small disturbance is present. The elements of the sheet above their original position are accelerated to the right under the influence of the velocity field induced by the elements of the sheet below their original position. Conversely, the elements below their original position are accelerated to the left. The effect is to stretch the sheet (requiring the addition of more vortices to maintain the spatial resolution when the sheet is represented by a system of discrete vortices) initially and to coil, or to wrap, the sheet causing the vorticity to collect. The direction of wrapping agrees with the direction of the vorticity. In parts (c) and (d) of Figures 8, the sheet

is represented at subsequent times. During the stretching/coiling process, vorticity is drawn into the region where the disturbance was introduced from the portions of the sheet on both sides; consequently, regions of rather concentrated vorticity form. The strength along the sheet connecting two successively shed regions of concentrated vorticity is very small, practically zero. The densely packed vorticity regions yield smooth velocity fields, as shown later in another example.

The importance of splitting discrete vortices is further illustrated in the case where the airfoil oscillates in plunge: the vertical displacement, y, is given by

$$y = A \sin \Omega t \tag{3.1.2}$$

where A is the amplitude of oscillation, $\Omega = \omega C/V_\infty$ is the reduced frequency and ω is the dimensional frequency. In part (a) of Figure 9, which is taken from Giesing's paper (1968), the wake computed by Giesing is shown, where $A = 0.3105$ and $\Omega = 17$. The dots represent the positions of the vortices shed previously at the trailing edge, and the line connecting the vortices was faired in by Giesing. The sequence in which the vortices were shed, some prior knowledge of the wake, and clearly some imagination were needed to draw the line. The wrapping/stretching mechanism is clearly evident and so is the need to add more vortices in order to preserve the spatial resolution. In part (b) of Figure 9, the flow visualization obtained by Bratt (1950) is shown. Bratt introduced smoke into the airstream upstream from the leading edge. Part (b) of Figure 9 served as a guide in the construction of part (a) of Fig 9. In part (c) Figure 9, the wake computed by implementing the splitting scheme is shown. The large-scale structures of the wake seem to be well predicted by the numerical results.

Ohashi and Ishikawa (1972) also studied the wakes behind plunging airfoils. They heated the air that passed over the upper surface of an NACA 65-010 airfoil. The resulting sharp gradient in the density of the air downstream from

the trailing edge was observed by means of a Schlieren apparatus. They observed three regions in the frequency-amplitude domain where the wakes have distinct structures. These regions are given in part (a) of Figure 10. The present numerically calculated wakes are shown in parts (b), (c) and (d) of Figure 10. In part (b), the amplitude of plunge ($A = 0.014$ chord) is small and the frequency ($\Omega = 5$) is high; the structures of the wake is similar to the one shown in Region I of part (a). In part (c), the amplitude of plunge (A = 0.05 chord) is larger and the frequency ($\Omega = 5$) is the same; the structure of the wake is similar to the one in Region II of part (a). In part (d) the amplitude of plunge (A = 0.05 chord) is kept the same as the previous and the frequency ($\Omega = 2.5$) is smaller; the structure of the wake is similar to the one in Region III of part (a). The calculated results follow the same trend as the observations, but the calculated boundaries between the regions are neither clear nor in the same approximate locations as the observed boundaries. The different airfoils used in the experiment and the numerical calculation (NACA 0012 airfoil is used in the numerical solution) is one of the reasons causing this discrepancy. It is also not known how much influence the buoyant forces caused by heating have on the wake geometry.

In Figure 11, the wakes behind an impulsively started airfoil are shown. In part (a), one frame from a well-known film loop (see Ref. 100) shown to beginning classes in fluid mechanics is given. The experiment was performed by placing powder on the surface of a fairly thin sheet of water flowing across a smooth, nearly level, plane surface. The results given in part (b) were obtained by considering the flow past a cambered Karman-Trefftz airfoil. In both cases, the airfoil has travelled about one chord. There is qualitative agreement. Shown in part (c) is a sequence of computed results for a different airfoil that experiences an impulsive start followed by an impulsive stop. Two counter-rotating regions of concentrated vorticity are clearly evident. These two regions are migrating downward. The region between these two large scale regions of concentrated vorticity is nearly devoid of vorticity because the

vorticity is being drawn in towards the center of each region, and the connecting vortex sheet is being stretched and weakened.

Now consider again the case of a pitching airfoil (the same case shown in Figure 7), where the pitch angle is given by Equation (3.1.1) and $k = 2.77$. During each cycle two regions of concentrated vorticity are created. In parts (a) and (b) of Figure 12 the wakes are shown after three and one quarter cycles and four and one quarter cycles, respectively. A comparison of parts (a) and (b) shows that after three and one quarter cycles the structure of the wake has nearly reached a steady state in the area from the trailing edge to approximately 2.75 chords downstream. The circulations around regions of concentrated vorticity 1 and 3 are negative (counterclockwise) while around regions 2 and 4 are positive. The disturbance flowfield corresponding to part (b), obtained by subtracting the freestream velocity from the total velocity field, is shown in part (c). Vorticity is obvious in the regions where the vortices are densely packed and there is practically no evidence of vorticity outside these regions. The centers of the regions of concentrated vorticity can be approximately located, and the horizontal spacing between two regions of the same sign of circulation (i.e., between 1 and 3 and between 2 and 4) is approximately 1.25 chords.

Part (a) of Figure 13 is a photograph by Wilder et al. (1990) of flow past a pitching airfoil in a water tunnel for the same reduced frequency and amplitude as in Figure 12. Part (b) of Figure 13 is the same as part (b) of Figure 12 and is put here for comparison. Comparing part (a) and part (b) of Figure 13 one sees that the numerical method simulates the wake structure very well, even in some of the finer scales. The distance between the centers of vortical structures of the same sign measured by Wilder et al. is 1.2 to 1.4 chords, very close to the present numerical result (about 1.25 chords). Although a dyed streakline between the regions of concentrated vorticity is evident, no experimental evidence of vorticity along the streakline was found

(that is, abrupt changes in velocity were not perceptible), which is consistent with the numerical simulation. The vortex layer has been stretched and in the process rendered thin; consequently, the velocity generated by this portion of the wake is quite weak. It should be noticed that, for both experimental and numerical results, there are some small spirals on the weak vortex layers connecting two adjacent big regions of concentrated vorticity. According to the numerical tests of Krasny (1986), the computer round-off caused those spirals, and they could be diminished by higher precision arithmetic. Here the splitting scheme might also be responsible for causing the spirals and the agreement with the flow visualization might be fortuitous. On the other hand, one cannot exclude the possibility that the present numerical model catches some disturbances that can cause those spirals in the experiment.

Next the pitch angel is given by Equation (3.1.1) and the reduced frequency is chosen as $k = \pi$ in order to simulate an experiment by Booth (1987), who used a pitching airfoil to generate wakes. In Figure 14, the wake with four regions of concentrated vorticity is shown; regions 1 and 2 were generated during the first cycle and 3 and 4 were generated during the second. The circulations around regions of concentrated vorticity 1, 2, 3 and 4 are, respectively, $\Gamma_1 = 1.0423$, $\Gamma_2 = -0.9290$, $\Gamma_3 = 1.0587$, and $\Gamma_4 = -1.1058$. $\Gamma_1 + \Gamma_2 = 0.1133$, $\Gamma_3 + \Gamma_4 = -0.0471$, and one can see that the vorticity distribution of the second cycle is more nearly symmetric than that of the first cycle. It is expected that if the calculation were continued the wake would continue to become more nearly symmetric. Booth measured the velocity behind an airfoil and numerically integrated his measurements to obtain the circulations around regions of concentrated vorticity. His results for the circulations, which are nondimensionalized here, are 1.12 and -0.992. The numerical predictions are in good agreement with Booth's observations.

Corresponding to another of Booth's experiments (1987), the pitch angle for one cycle of the motion is given by the following

$$\theta_p = \begin{cases} -10^\circ \cos(\pi t) & 0.0 \le t \le 1.05 \\ -25.1607^\circ(\frac{t}{T} - 0.6026) & 1.05 < t \le 5.0 \end{cases} \tag{3.1.3}$$

where the period $T = 5.0$. In Figure 15, the computed wakes are shown after one and a half cycles. The purpose of choosing θ_p as defined in Equation (3.1.3) is to create relatively isolated regions of concentrated vorticity. They are generated by the rapid sinusoidal variation of θ_p from -10° to 10° in the first 20% of the cycle. The vorticity that is generated when θ_p linearly returns to -10° during the remainder of the cycle is much weaker, and the corresponding portion of the wake does not roll up much. The vorticity generated during the first 20% of the cycle is negative (counterclockwise). As indicated in the figure, the centers of the regions of concentrated vorticity are about 5 chord lengths apart; this result agrees quite well with Booth's experimental results.

In Figure 16, the horizontal components of the total (computed) velocity are plotted as functions of vertical position for the three different locations shown in Figure 15. Because of the high density of vortices in the regions of concentrated vorticity, the computed velocity is smooth. The numerical simulation shows a rather concentrated vortical flow. The value of the nondimensional circulation for a path around the region of concentrated vorticity is 0.712 for the numerical solution and 0.707 for Booth's experimental results. Again, the agreement is quite good.

Another example is the comparison with the experimental results obtained by Straus et al. (1990). An NACA 0018 airfoil is used. Since only the frequency and amplitude of the pitch angle were given in the paper of Straus et al., we let the airfoil pitch about 0.136 chord point and the pitch angle vary in the following way

$$\theta_p = \begin{cases} -3.9^\circ \cos(7.8969t) & 0.0 \le t \le \dfrac{\pi}{7.8969} \\ 3.9^\circ & \dfrac{\pi}{7.8969} < t \end{cases} \qquad (3.1.4)$$

Similar to the previous case (the simulation of Booth's experiment), a relatively isolated region of concentrated vorticity is created as shown in Figure 17 where the center of this region of concentrated vorticity is downstream about 3.73 chords of the airfoil away from the pitching axis.

The profiles of the perturbed velocity obtained by subtracting the freestream velocity from the total velocity are shown in Figure 18. The experimental measurements are made at position 3.730 chords downstream of the pitching axis and the numerical results are calculated at positions 3.695 and 3.720 respectively. The good agreement between the experimental and numerical results in Figure 18 is obvious. It is interesting to note that the velocity profiles shown in Figure 16 and Figure 18 exhibit what is often thought to be a manifestation of the viscosity. But it can be quite accurately simulated by an entirely inviscid model. This implies that the evolution of a free shear layer may be mainly controlled by an inviscid mechanism.

Several numerical simulations of the wake have been presented and compared with experimental results. The numerical method accurately predicts the spacing and circulation of the regions of concentrated vorticity and the velocity distribution in those regions.

3.2 Blade-Vortex Interaction

First the interaction of an airfoil with a single passing vortex investigated. Second the interaction between a stationary airfoil and the wake generated by a pitching airfoil is simulated.

The quarter-chord point of the airfoil is chosen as the origin of the coordinate system, and the angle of attack is zero. At the beginning, the flow is steady. Then a single vortex with strength $\Gamma_v = 0.2$ is introduced at the position $x_v = -5.25$ and $y_v = -0.26$ (five chords upstream from and slightly below the origin) and convected downstream at the local particle velocity. The flow becomes unsteady. The variation of the lift coefficient C_L ($= L/\frac{1}{2}\rho V_\infty^2 C^2$) with the position of the vortex is shown in Figure 19. When the vortex is far from the airfoil, a small negative lift acts on the airfoil. As the vortex approaches the airfoil, the lift becomes more negative and reaches its maximum negative value just before the vortex reaches the leading edge. As the vortex passes under the airfoil, the lift increases, changing from negative to positive. After the vortex passes the trailing edge, the lift decreases gradually toward zero. As shown in Figure 19, the present solution is in very good agreement with the attached turbulent-boundary-layer solution obtained by Hsu and Wu (1986) (marked Turbulent Flow in the figure) and with the solution of the Euler equations for transonic flow obtained by Srinivasan et al. (1986) (marked Transonic Flow).

There have been several attempts to improve the model of blade-vortex interaction by considering the oncoming stream to contain a system of vortices. It appears that Hardin and Lamkin (1984) were the first to consider a spatial distribution of vorticity rather than a single vortex in the oncoming stream. Poling et al. (1987) extended the single-vortex model by sequentially releasing a series of discrete vortices from a fixed point upstream. Panaras (1987) modelled a finite, vorticity-bearing region by releasing a cloud of discrete vortices upstream from an airfoil. The initial deployment of the point vortices was prescribed, and all had the same prescribed circulation. Lee and Smith (1987) also released a cloud of point vortices upstream. Poling et al. (1988) considered the interaction between a cloud of vortices and an airfoil. They chose a distribution of circulations in the initial arrangement that produced a velocity field similar to their experimental observations [also

similar to the profile in Figure 16]. Both Panaras (1987) and Poling et al. (1988) considered flow past a Joukowski airfoil, both used conformal mapping to obtain their results, Poling et al. imposed the general unsteady Kutta condition, but Panaras did not. Lee and Smith used a source-panel method (instead of the vorticity-panel method used here) and imposed the general unsteady Kutta condition at the trailing edge.

The example of blade-vortex interaction computed by Panaras (1987) is given in Figure 20. The solid dots are the vorticity-bearing vortices; the hollow dots are simply markers to help visualize the motion. The cloud of point vortices is shown at six different times. The cloud is split by the airfoil, and the portion going along the upper surface arrives at the trailing edge a little before the portion moving along the lower surface. The plots under the airfoil give the pressures at three locations on the upper surface as functions of time.

Another example of blade-vortex interaction computed by Lee and Smith (1987) is given in Figure 21. In part (a), the cloud of vortices is shown at six different times. The cloud is divided by the airfoil, and the portion moving along the lower surface arrives at the trailing edge ahead of the portion moving along the upper surface. More details are shown in parts (b).

In Figure 22, the blade-vortex interaction computed by Poling et al. (1988) is shown. The vorticity-bearing region is divided by the airfoil. The wake generated at the trailing edge of the airfoil is also shown. In the cases shown in Figures 21 and 22, it appears that vorticity moving along the lower surface arrives at the trailing-edge slightly ahead of the vorticity moving along the upper surface, in contrast with Panaras's results. However, the airfoils and the initial distributions of circulations are different.

The present method is used in an attempt to achieve a partial numerical simulation of the BVI experiment conducted by Booth (1987). In the experiment, the wake generated by a pitching airfoil of chord length 0.75

interacts with a stationary airfoil of unit chord downstream. As shown in Figure 23, the quarter-chord point of the pitching airfoil is at (0.0, 0.0), and the quarter-chord point of the stationary one is at (1.5625, -0.094), i.e., the horizontal distance from the leading edge of the stationary airfoil to the trailing edge of the pitching airfoil is 0.75 when both airfoils are at zero angle of pitch. The case where the angle of attack of the stationary airfoil is zero is considered here. The pitch angle of the oscillating airfoil is given by Equation (3.1.3), which generates a relatively isolated region of concentrated vorticity of circulation 0.712 nondimensionalized by the velocity of the freestream and the length of the pitching airfoil which is 0.75 of the length of the stationary one. So when the length of the stationary airfoil is used, the circulation is $0.75 \times 0.712 = 0.534$.

In Figure 24, shown are the two airfoils with their wakes and the pressure distribution on the stationary one at different times. In part (a) of Figure 25, the history of the lift coefficient C_L is shown. At the beginning, there is positive (upward) lift acting on the stationary airfoil because the pitching airfoil upstream is at a negative angle of attack and deflects the oncoming stream upward. For this steady state, the airfoils and the calculated pressure distribution on the stationary one are shown in part (a) of Figure 24. The lift reaches its maximum value at $t = 1.37$ just before the strong concentrated vorticity generated in the first 20 % of the cycle reaches the leading edge of the stationary airfoil as shown in part (b) of Figure 24, where the wake of the pitching airfoil is plotted with and without the stationary airfoil present. In part (c) of Figure 24, the wakes and the pressure distribution are shown at $t = 2$. From the view of the wake without the stationary airfoil present, one can see that the vortex sheet generated by the pitching airfoil is enveloping the stationary airfoil and is stretching. The more this vortex sheet is stretched, the weaker its strength is. The pressure distribution on the upper surface is very rough in the region close to the strong vorticity. For the unsteady problem evaluating the pressure through Equation (2.6.1) involves the relative surface

velocity γ and both its spatial and temporal derivatives. When the wake is close to the surface, the gradient of the surface velocity can be very large. Maskew (1980) suggested that additional subpanels be put on the surface to capture the resolution of the velocity, but no subpanels are added in the present model. As a result, the pressure distribution is rough, this roughness moves towards the trailing edge as the concentrated vorticity convects. In part (d) of Figure 24, the pressure and the wakes are shown at time $t = 3$. The pressure distribution is very smooth. The very weak vortex sheet (as the result of stretching) covers almost the entire airfoil except a small portion near the lower trailing edge. In part (e) of Figure 24, the pressure and the wakes are shown at time $t = 4.5$.

In Figure 25, the history of the lift coefficient is shown for several different studies. In part (a), C_L is obtained by the present numerical method for the case shown in Figure 24. In part (b), a sample of the result computed by Lee and Smith (1987) is shown; in part (c), the result computed by Poling et al. (1988) is given; and in part (d), the experimental result of Booth (1987) is presented. The results in parts (b) and (c) were computed by releasing a cloud of vortices upstream. The one in part (a) was computed by actually modelling the interaction between two airfoils as in the case of the experiment in part (d), the one in part (c) was computed with the conditions chosen in such a way to imitate the experiment in part (d).

In the case (computed by Lee and Smith) shown in part (b) of Figure 25, the direction of the vorticity is opposite to that in the other cases shown in parts (a), (c) and (d) of Figure 25. When the sign is changed the result of Lee and Smith is similar to the present result shown in part (a). The jagged regions of the curve in part (a) of Figure 25 correspond to the times when the wake actually brushes along the surface of the stationary airfoil. Apparently, the re-distribution of panels nearly eliminated this feature from the results of Lee and Smith. The mean-value curve (i.e., the curve faired through the jagged

regions) for the present result converged rapidly as the number of panels is increased and the time step is decreased, which is typical of all the present results. Point *A* in part (a) of Figure 25, corresponds to the end of the sinusoidal portion of the cycle defined by Equation (3.1.3).

The result of Poling et al. (1987) has the best qualitative agreement with the experimental result of Booth. Booth gives only the increment in lift in part (d) of Figure 25; the lift created by the initial negative angle of attack of the forward airfoil has been subtracted.

The difference between Booth's experiment and the present numerical simulation is most likely due to the separation caused by the strong and close vortex interaction. Separation can occur when the strong vortex is close to the airfoil. Telionis and co-workers (1990) have observed in some experiments a significant separation bubble that moves along the surface with the passing region of concentrated vorticity. In Booth's experiment, the Reynolds number was first given as 85,300 (Booth, 1986) based on the flow speed 20 ft/sec. But later he found that the mean flow speed was about 15 ft/sec when the flow reached the stationary airfoil (Booth, 1987), then the Reynolds number should be 63,975. Under this Reynolds number, the boundary layer was likely laminar when the separation occurred. The calculation of BVI for viscous flow by Hsu and Wu (1986) showed that when separation occurs the lift differs considerably from that corresponding to attached flow. The numerical results obtained here are based on the assumption that the flow is always attached.

The next example is the numerical simulation of another BVI experiment conducted by Straus et al. (1990), which is similar to Booth's experiment. Here an NACA 0018 airfoil of chord length 0.5435, which pitches about its 0.15-chord point, is used to generate the wake which interacts with a stationary NACA 0012 airfoil of unit chord downstream. The 0.15-chord point of the pitching airfoil is at (0.0, 0.0), and the quarter-chord point of the stationary airfoil is at (4.045, -0.24), i.e., the horizontal distance from the trailing edge of the pitching

airfoil to the leading edge of the stationary airfoil is $3\frac{1}{3}$ when the both airfoils are at zero angle of attack. The angle of attack of the stationary airfoil is zero, and the angle of the pitching airfoil is given as the following

$$\theta_p = \begin{cases} -4.0^\circ \cos(7.8969t) & 0.0 \le t \le \frac{\pi}{7.8969} \\ 4.0^\circ & \frac{\pi}{7.8969} < t \end{cases} \qquad (3.2.1)$$

which is about the same as Equation (3.1.4) except the amplitude here is 4.0 . The concentrated vorticity generated by the above arrangement is counterclockwise.

At nine different times $t_1 = 1.59$, $t_2 = 3.38$, $t_3 = 3.58$, $t_4 = 3.78$, $t_5 = 3.98$, $t_6 = 4.18$, $t_7 = 4.38$, $t_8 = 4.58$ and $t_9 = 6.17$ during the interaction, both airfoils and their wakes are shown in Figure 26. When $t = 1.59$, the center of the region of concentrated vorticity generated by the pitching airfoil is 0.24 above the chord line of the stationary airfoil as shown in part (a) and the circulation around the concentrated vorticity is about -0.15 , and they are in agreement with the arrangement of the experiment. As shown in parts (b) through (g), from t_2 to t_7 the concentrated vorticity generated by the pitching airfoil is passing the stationary airfoil (close vortex interaction). At t_8 the vorticity has just passed the trailing edge as shown in part (h), and at t_9 the wake of the pitching airfoil has started to mix up with that of the stationary one as shown in part (i).

Corresponding to the times t_2, through t_8, when the concentrated vorticity is approaching, passing by, and leaving the stationary airfoil, the surface velocities γ are shown in Figure 27, the pressure distributions are shown in Figure 28, and the pressure gradients (from the leading edge to the trailing edge) on the upper surface are shown in Figure 29.

As shown in Figure 27, the passing vorticity influences only slightly the velocity on the lower surface while it has a stronger effect on the velocity on

the upper surface: there is a bump on the velocity curve as if there were a bump on the surface which moved from the leading edge to trailing edge as the concentrated vorticity passes by. A bump can also be observed in the pressure distributions shown in Figure 28. As shown in Figure 29, the region of favorable pressure gradient (negative one) near the leading edge on the upper surface increases from t_2 to t_4, and from t_4 to t_8 it almost does not change. This is in agreement with the experiment of Straus et al.. It should be mentioned here that the adverse pressure gradient (positive one) decreases from t_2 to t_8.

The histories of the lift, drag, and moment (positive when clockwise about the leading edge as defined by Straus et al., 1990) coefficients, compared with the experimental results of Straus et al., are shown in Figure 30. In part (a), at the initial time ($t = 0$) there is an initial difference between the numerical curve of C_L and the experimental one. In part (a′), the numerical curve is shifted up 0.017 (the initial difference between the numerical result and the experimental result). Then the numerical curve agrees with the experimental one very well. In part (b), when $t = 0$, the initial difference between the numerical C_D and the experimental C_D is 0.003. And in part (b′), the numerical curve of C_D is shifted up 0.003. Again the the numerical curve fits the experimental one very well. Those initial differences partially are attributable to the numerical error rooted in the number of the elements used to represent the profile of the airfoil. Here the number of elements on the surface of the stationary airfoil is 108. When the angle of attack is zero and the flow is steady, the drag is zero for ideal flows. But the numerically calculated drag coefficient is about -0.003, which is about the magnitude of the initial difference shown in part (b) of Figure 30. Some numerical tests showed that the magnitude of drag coefficient decreased as the number of the elements increased at the expense of more computing time. On the other hand, the experimental error might also be responsible for the difference.

The nine different times t_1, t_2, t_3, t_4, t_5, t_6, t_7, t_8 and t_9 are marked in parts (a′), (b′) and (c) of Figure 30. At t_2, the concentrated vorticity is approaching the leading edge of the stationary airfoil as shown in part (b) of Figure 26, and the lift coefficient reaches its maximum value as shown in part (a′) of Figure 30, and the drag and moment coefficients reach their minimum values as shown in parts (b′) and (c) of Figure 30. The numerical and the experimental results agree well for the lift except when the concentrated vorticity is leaving the trailing edge of the stationary airfoil. For the drag and moment, the discrepancies are observed when the region of concentrated vorticity approaches and leaves the stationary airfoil. As shown in Figure 31, similar discrepancies occurred when Straus et al. compared their experimental results with their own numerical results obtained by using a single point vortex and with the linear results of Sears (1969).

Another simulation of the experiment of Straus et al. (1990) is presented next, in which the sign of the concentrated vorticity is clockwise, opposite to the one in the previous experiment. The arrangement is the same as the previous one except the angle of the pitching airfoil is given as follows

$$\theta_p = \begin{cases} 4.12^\circ \cos(7.8969t) & 0.0 \le t \le \dfrac{\pi}{7.8969} \\ -4.12^\circ & \dfrac{\pi}{7.8969} < t \end{cases} \qquad (3.2.2)$$

The concentrated vorticity generated by the above arrangement is clockwise.

At nine different times $t_1 = 1.59$, $t_2 = 3.38$, $t_3 = 3.58$, $t_4 = 3.78$, $t_5 = 3.98$, $t_6 = 4.18$, $t_7 = 4.38$, $t_8 = 4.58$ and $t_9 = 6.17$ during the vortex interaction, both airfoils and their wakes are shown in Figure 32. When $t = 1.59$, the center of the region of concentrated vorticity generated by the pitching airfoil is 0.19 chords above the chord line of the stationary airfoil as shown in part (a) and the dimensionless circulation around the concentrated vorticity is about 0.16. The position and circulation are in good in agreement with the observations of the experiment. As shown in parts (b) through (h), from t_2 to t_8 the

concentrated vorticity generated by the pitching airfoil is passing the stationary airfoil (close vortex interaction). Comparing part (h) of Figure 26 and part (h) of Figure 32, one can see that the counterclockwise vorticity moves faster than clockwise vorticity because the latter slows the flow between the vorticity and the surface of the airfoil during the interaction. At t_9 the wake of the pitching airfoil has started to mix with that of the stationary one as shown in part (i) of Figure 32.

Corresponding to the moments t_2 through t_8, when the concentrated vorticity is approaching, passing by, and leaving the stationary airfoil, the surface velocities are shown in Figure 33, the pressure distributions are shown in Figure 34, and the pressure gradients (from the leading edge to the trailing edge) on the upper surface are shown in Figure 35.

As shown in Figure 33, the passing vorticity influences only slightly the velocity on the lower surface, while it has a stronger effect on the velocity on the upper surface: there is a dip on the velocity curve as if there were a dip on the surface which moved from the leading edge to trailing edge as the concentrated vorticity passes by. This bump can also be observed in the pressure distributions shown in Figure 34. Comparing Figure 33 with Figure 27, one can observe that the clockwise vorticity noticeably slows the velocity on the surface of the stationary airfoil at the locations close to it. As shown in Figure 35, the region of the favorite pressure gradient near the leading edge on the upper surface decreases from t_2 to t_4, and from t_4 to t_8 it almost does not change. This is in agreement with the experiment of Straus et al.. The adverse pressure gradient increases from t_2 to t_8.

The histories of the lift, drag, and moment coefficients, compared with the experimental results of Straus et al., are shown in Figure 36, where the nine different moments t_1, t_2, t_3, t_4, t_5, t_6, t_7, t_8 and t_9 are marked. Similar to parts (a′) of Figure 30, the numerical calculated curve of C_L in part (a′) of Figure 36 is shifted down 0.017 (because the lift is negative at $t = 0$) from its position as

shown in part (a) of Figure 36. At t_2, the concentrated vorticity is approaching the leading edge of the stationary airfoil as shown in part (b) of Figure 32, and the lift and drag coefficients reach their minimum values at moment t_2 as shown in parts (a) and (b) of Figure 36, and the moment coefficient reaches its maximum value as shown in part (c) Figure 36.

The agreement between the numerical and the experimental results is good, but not as good as in the previous case where the passing vorticity is counterclockwise. As shown in Figure 37, similar discrepancies occurred when Straus et al. compared their experimental results with their own numerical results obtained by using a single point vortex and the linear results of Sears (1969). Straus et al. (1990) attributed this discrepancy to the flow separation on the upper surface of the airfoil, which was not taken into account in the numerical models. Straus et al. pointed out that the Reynolds number was 375,000 in their experiments and that separation was quite possible. Because the adverse pressure gradient decreases as the counterclockwise vorticity passes the airfoil and it increases as the clockwise vorticity passes the airfoil, the separation is more likely to happen in the latter case than in the former. It should also be mentioned that the clockwise vorticity locally slows down the velocity retarding the flow on the surface facing the vorticity and increasing the possibility of a large separation occurring.

The comparisons the present results and the experimental results of Straus et al. are much closer than between the the present results and the experimental results of Booth, even for the case of clockwise vorticity, because the vortex interaction in the Booth's experiment was much stronger and closer than the one in the experiment of Straus et al.

3.3 Summary

The numerical simulations of the wake clearly reveal a coiling or wrapping process that, qualitatively at least, is in good agreement with flow visualizations done in a water tunnel. The vorticity in the wake is drawn into relative isolated regions, call regions of concentrated vorticity. The velocity distribution through such a region appears to have a viscous-core region, but the flowfield is developed entirely by an inviscid model. The process resembles diffusion, but happens much too rapidly to be explained by viscous effects. So the present numerical results strongly support the argument of Wilder et al. (1990) that the evolution of the wake is mainly controlled by an inviscid mechanism.

When the dimension of a region of concentrated vorticity is much smaller than the distance between the vorticity and the airfoil, the single vortex is a good model of the relatively concentrated vorticity. But when the dimension of a region of concentrated vorticity is large compared with the distance between the vorticity and the airfoil, the present model of blade-vortex interaction is necessary for a better numerical simulation.

The present inviscid panel method coupled with vortex dynamics for numerically simulating the flowfield has potential as a model of blade-vortex interactions under the circumstance that no serious separation occurs. If a large separation region is involved, the present numerical model fails to predict blade-vortex interaction, and a new numerical model that considers separation is needed.

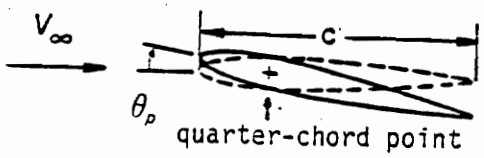

Figure 6. Airfoil pitching about its quarter-chord point.

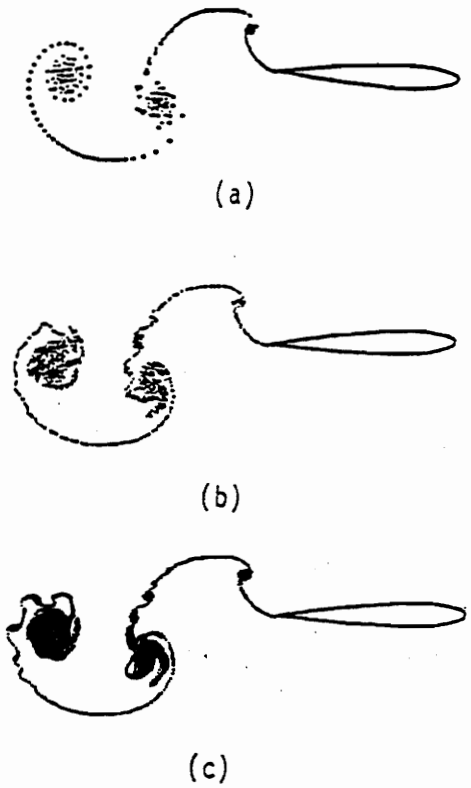

Figure 7. Computed wakes of a pitching airfoil: the pitch angle is given by Equation (3.1.1) with $k = 2.77$. After one and one quarter cycles (250 time steps), the airfoil is rotating counter-clockwise at this instant. Each point shows the location of a vortex blob: (a) without splitting, 250 vortex blobs, (b) with splitting and combining, 512 vortex blobs, and (c) with splitting for a smaller critical length, 3818 vortex blobs.

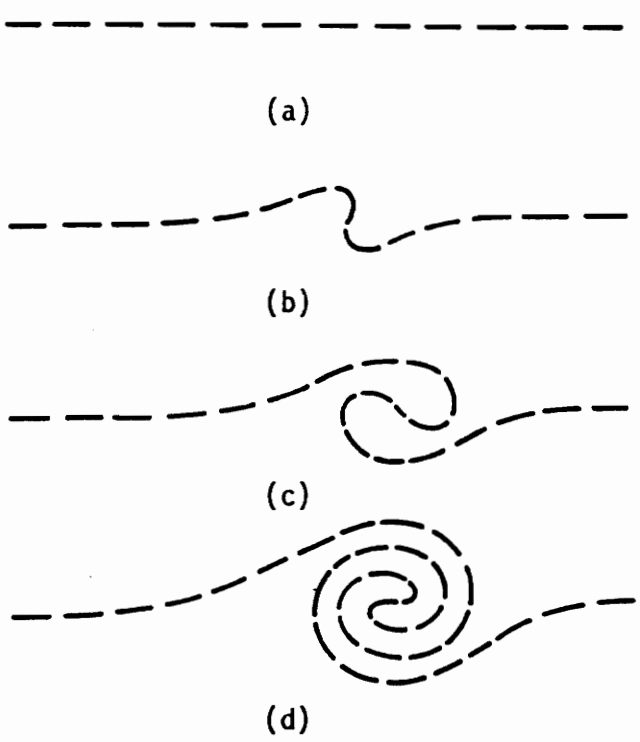

Figure 8. Physical mechanism for coiling of the free shear layer under the influence of the velocity it induces on itself: (a) undisturbed layer of clockwise vorticity; (b) the layer after the introduction of a small disturbance; (c) and (d) the subsequent coiling.

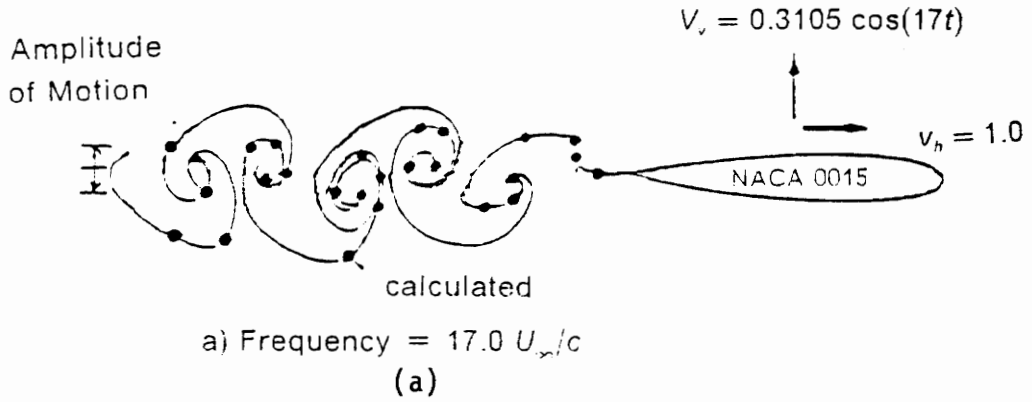

(b)

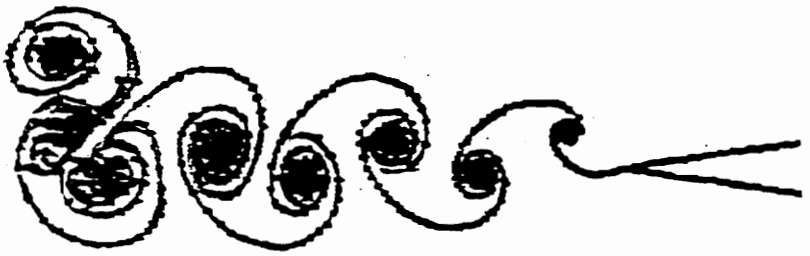

(c)

Figure 9. Wakes of a plunging airfoil: (a) the numerical result calculated by Giesing (1968) where V_v and V_h are respectively the vertical and horizontal velocity components, (b) the flow visualization obtained by Bratt (1950), and (c) the numerical result obtained by the present method.

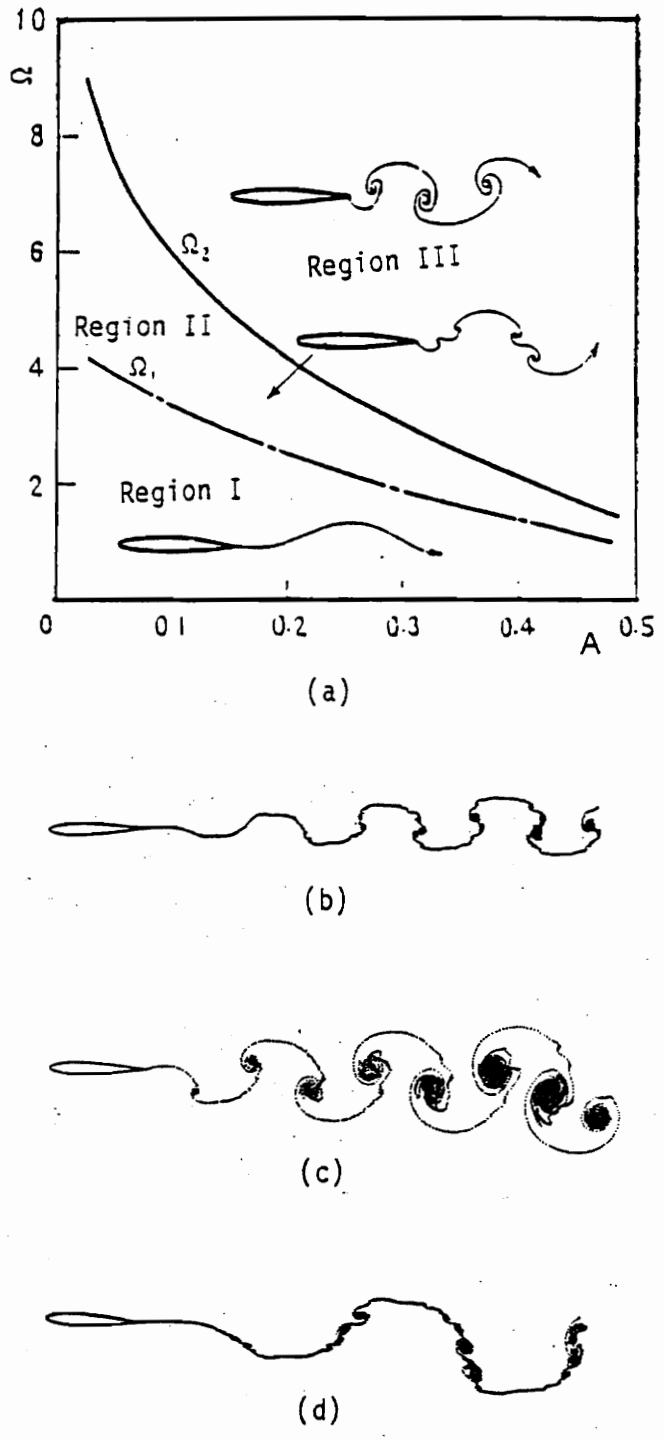

Figure 10. Wake structures of a plunging airfoil: (a) the three regions observed by Ohashi and Ishikawa (1972) in the frequency-amplitude space where the wakes have distinct structures The numerical results are shown in (b), (c) and (d). (b) A = 0.014, $\Omega = 5$; (c) A = 0.05 , $\Omega = 5$; (d) A = 0.05, $\Omega = 2.5$.

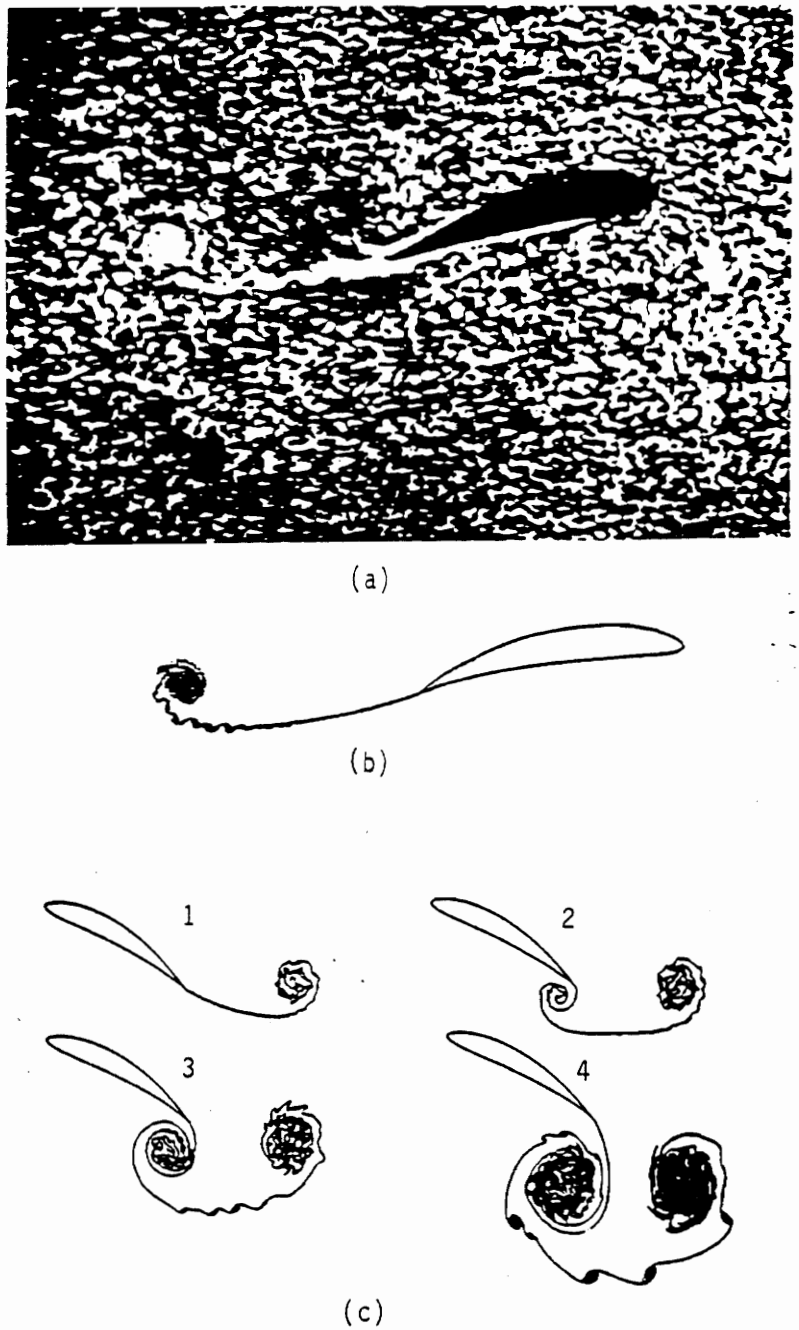

Figure 11. Wakes behind an impulsively started airfoil: (a) visualization from the film loop (Ref. 100); (b) numerical result; (c) a time sequence of computed wakes behind an airfoil experiencing an impulsive start followed by an impulsive stop.

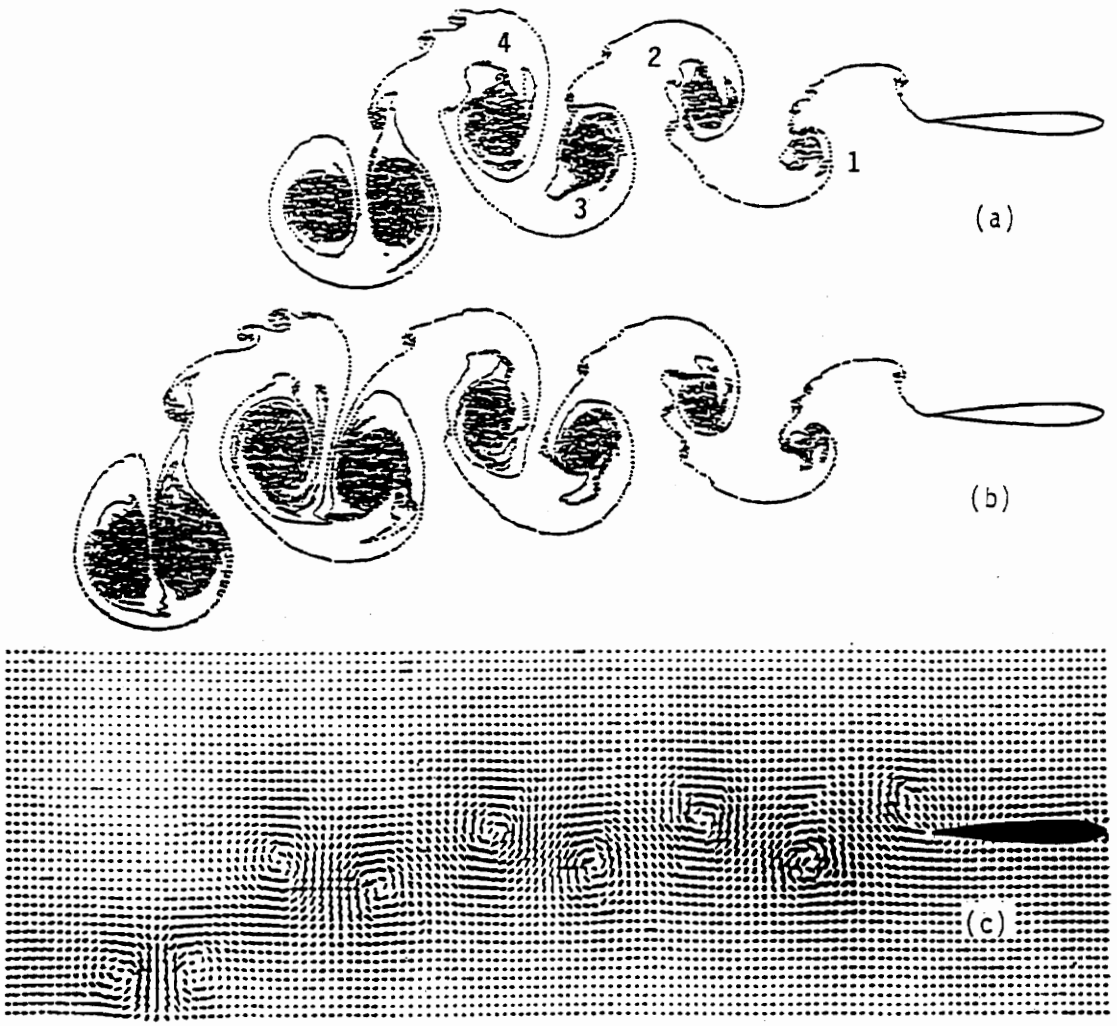

Figure 12. Computed wakes of a pitching airfoil: the same case as in Figure 7. (a) After three and one quarter cycles; (b) after four and one quarter cycles; (c) the disturbance-velocity field corresponding to the wake in (b) above. Frequency and amplitude of the motion agree with those in the experiment represented in Fig. 13.

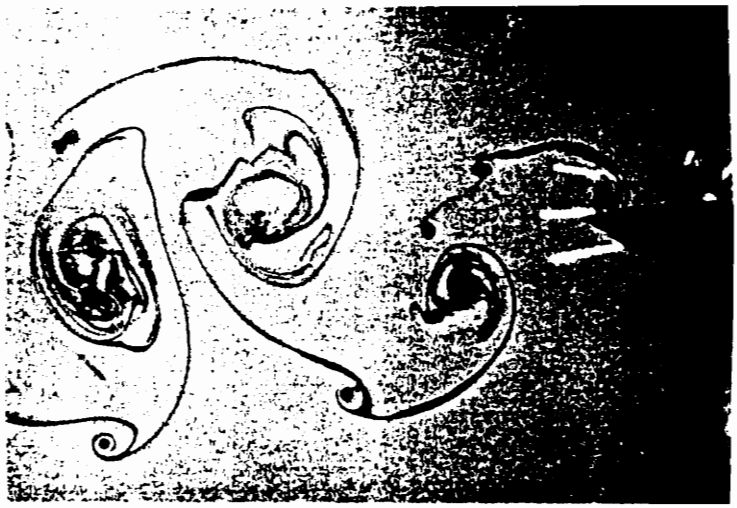

(a)

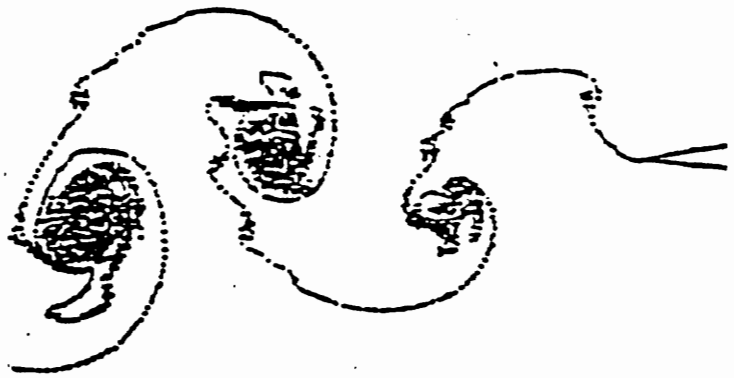

(b)

Figure 13. Comparison between experimental and simulated wakes: pitching frequency and amplitude agree with those in Figures 7 and 12. (a) Photograph of the wake behind a pitching airfoil in a water tunnel (Wilder et al., 1990); (b) the same as in part (b) of Figure 12.

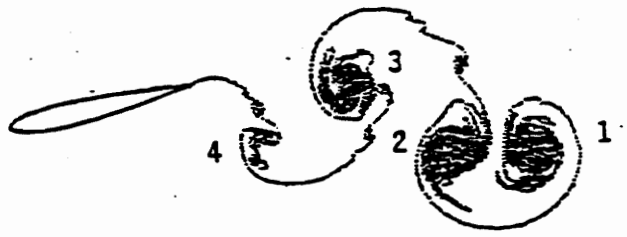

Figure 14. Computed wake behind a pitching airfoil: the pitch angle is given by Equation (3.1.1) with $k = \pi$, and the amplitude and frequency agree with those in the experiment of Booth (1987).

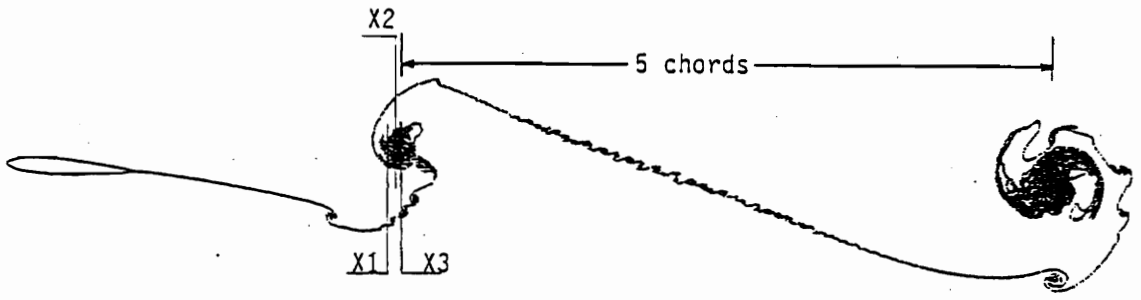

Figure 15. Computed wake behind a tailored pitching airfoil: the pitch angle is given by Equation (3.1.3). The numerical result agrees with the observation in the experiment by Booth (1987).

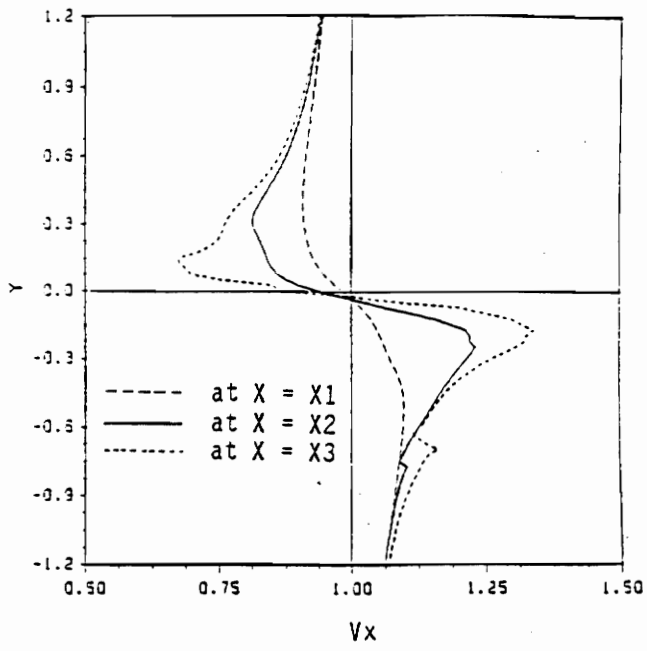

Figure 16. Computed profiles of the horizontal velocity component at the three stations indicated in Figure 15: as a result of the high density of vortices in the wake, the profiles are smooth. The profiles are computed by an inviscid model of the flowfield but exhibit what is often thought to be a viscous vortex core.

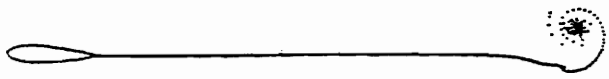

Figure 17. Computed wake: simulation of the experiment of Straus et al. (1990). The pitch angle is given by Equation (3.1.4).

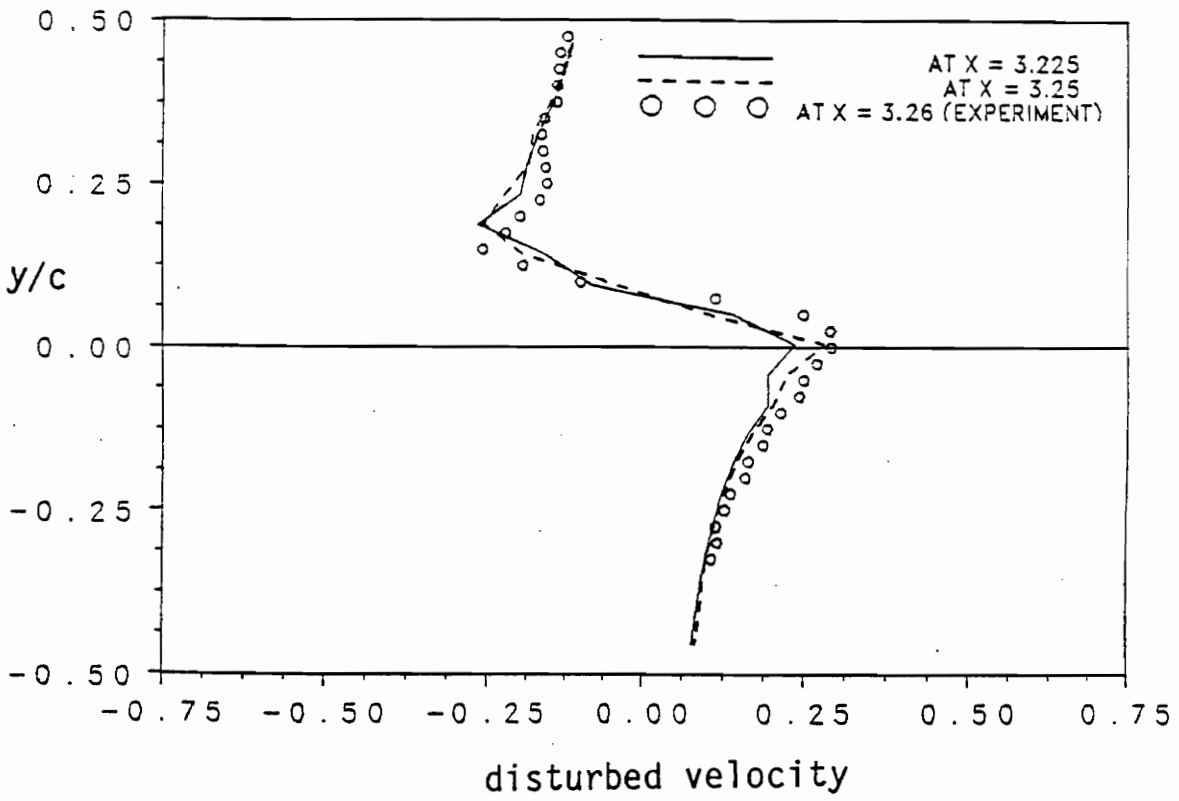

Figure 18. Comparison between the numerical and experimental velocity profiles for the same case as in Figure 17.

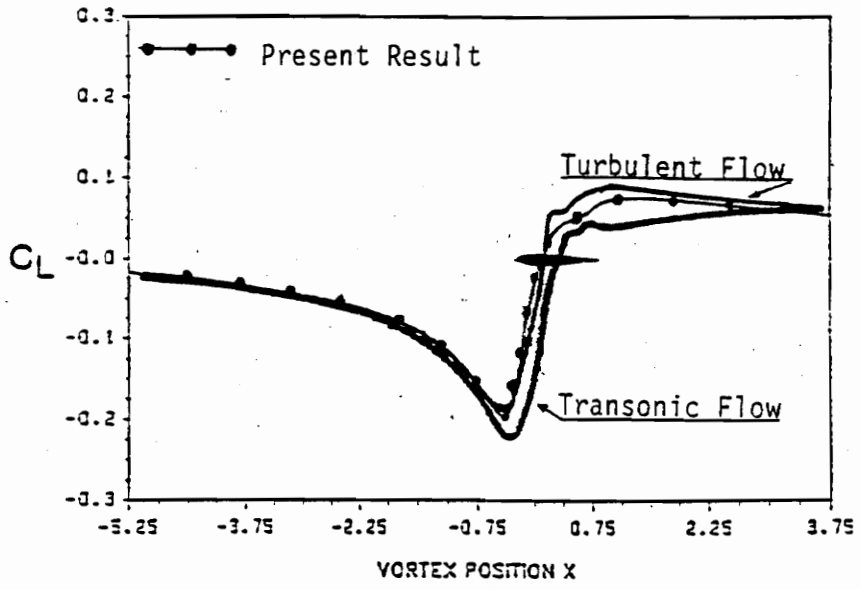

Figure 19. Lift coefficient for the interaction between a point vortex and an airfoil: the present numerical result, the result of turbulent flow was computed by Hsu and Wu (1986), and the result of transonic flow was computed by Srinivasan et al. (1986).

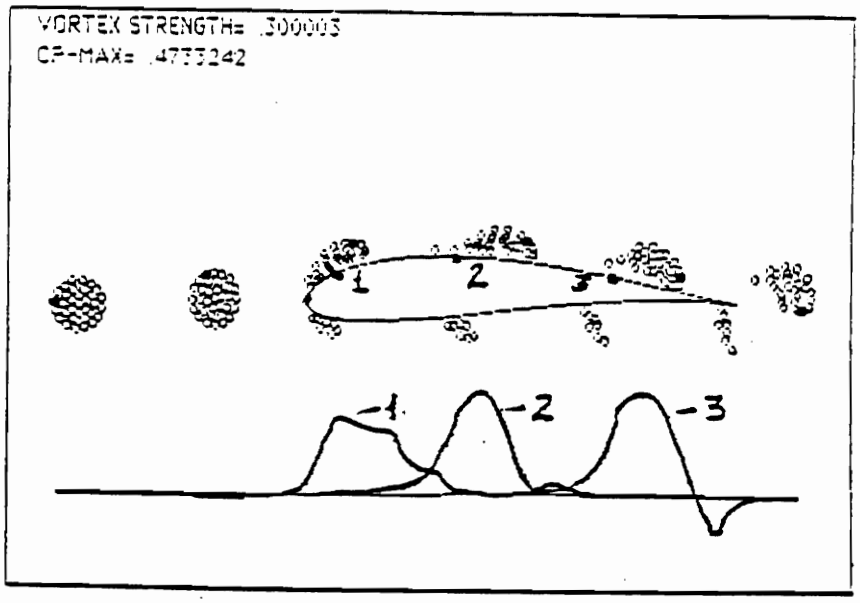

Figure 20. **Blade-vortex interaction computed by Panaras (1987) at six different times:** the curves at the bottom show the pressure at points 1, 2, and 3 on the airfoil surface as functions of time.

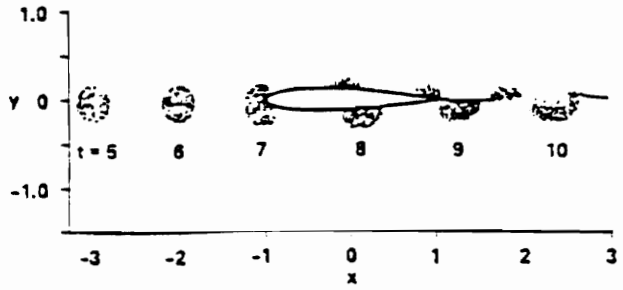

(a)

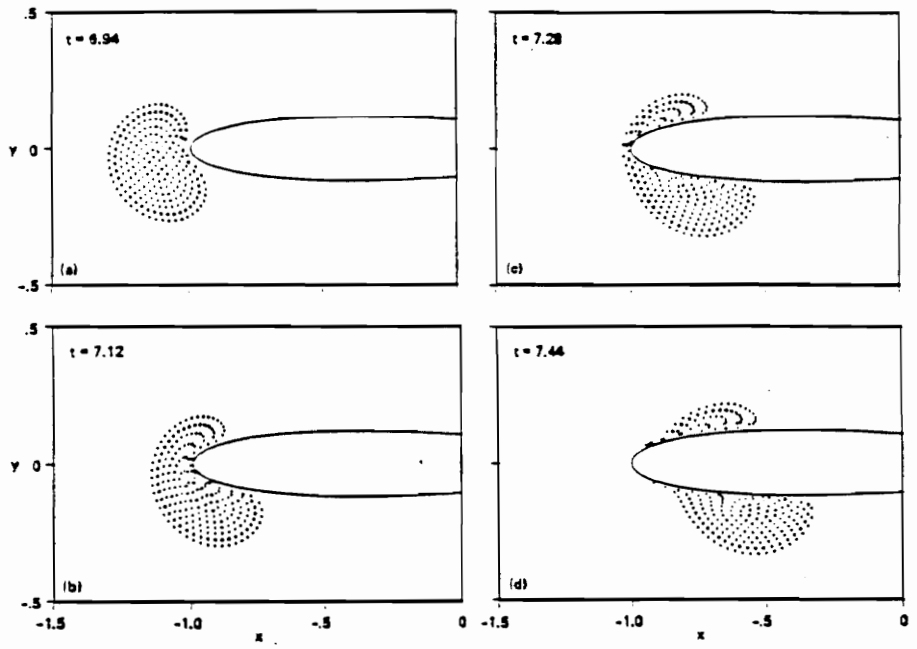

(b)

Figure 21. Blade-vortex interaction computed by Lee and Smith (1987): (a) cloud of point vortices at six different times; (b) details of the interaction near the leading edge while the cloud is being split.

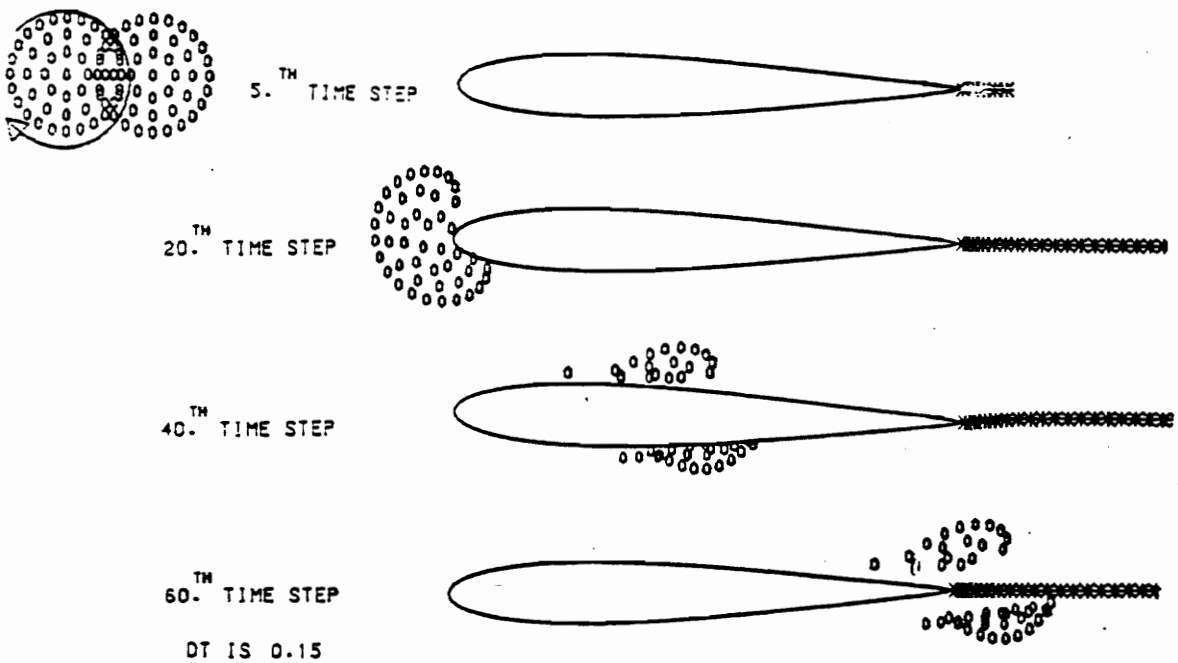

Figure 22. Blade-vortex interaction computed by Poling et al. (1988) at four different times.

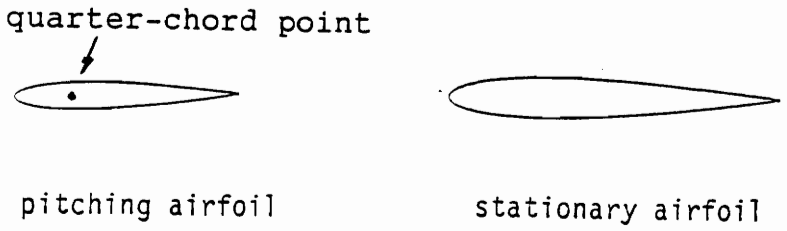

Figure 23. Setup of blade-vortex interaction.

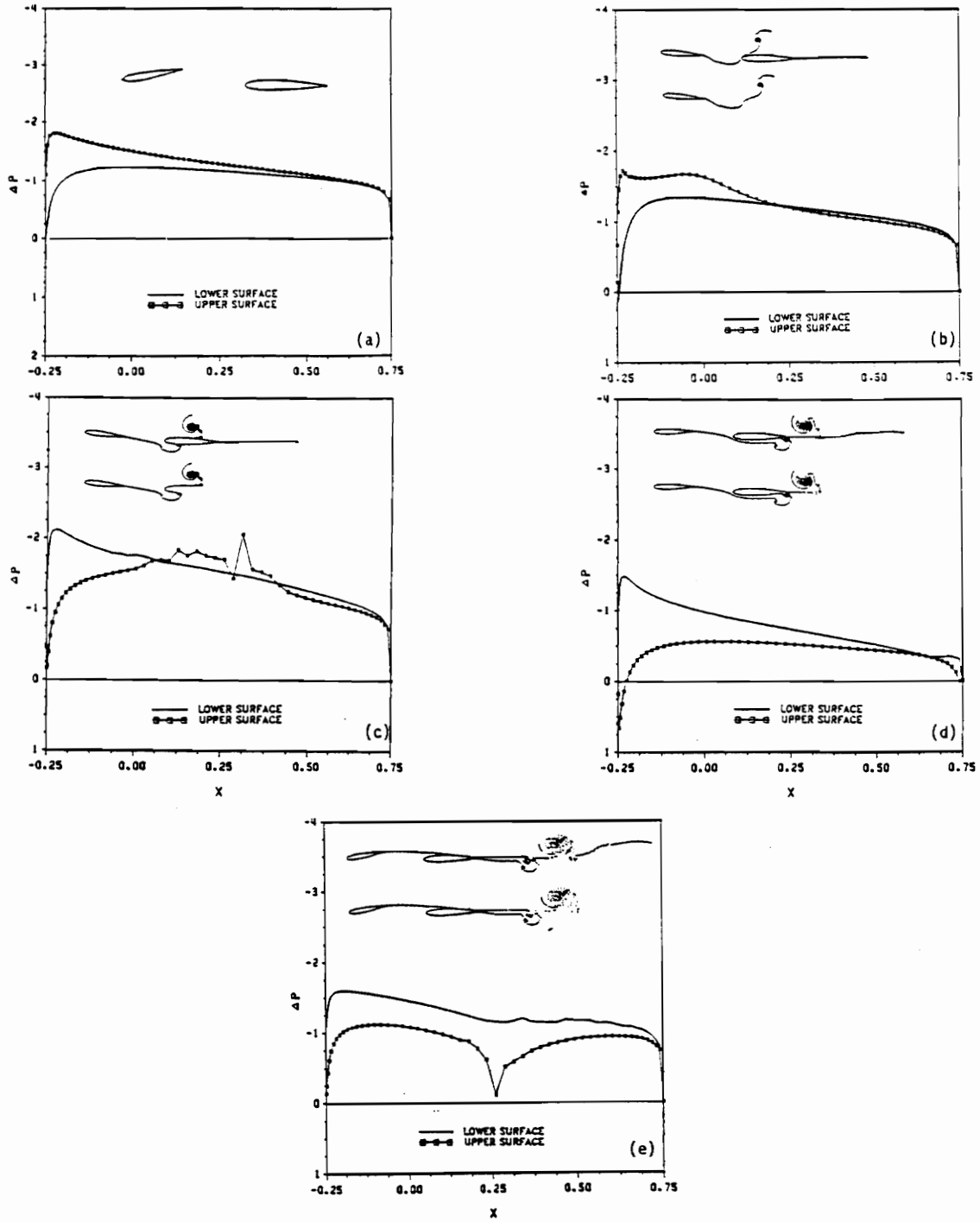

Figure 24. Pressure distributions on the stationary airfoil during blade-vortex interaction: the pitch angle is given by Equation (3.1.3). (a) Steady state before the pitching airfoil starts pitching; (b) at time $t = 1.37$; (c) at time $t = 2$; (d) at time $t = 3$; (e) at time $t = 4.5$. The inserts show both the airfoils and their wakes in the upper view, and only the pitching airfoil and its wake in the lower view.

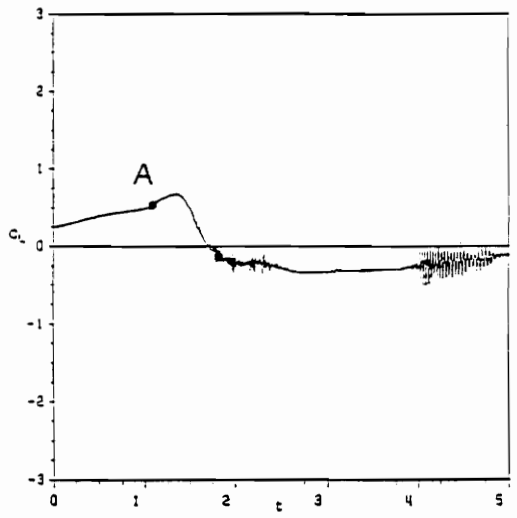

(a)

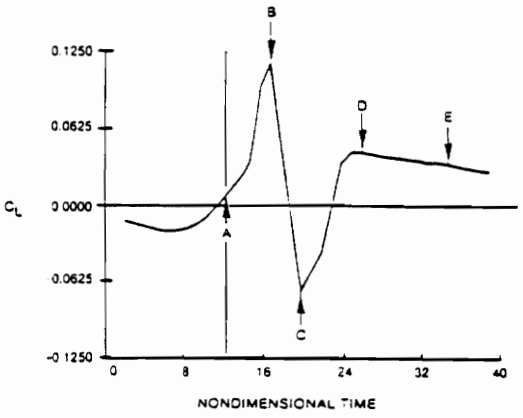

(c)

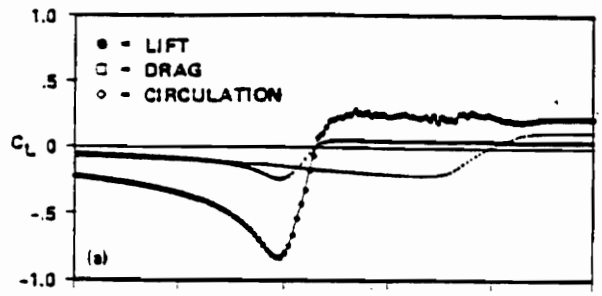

(b)

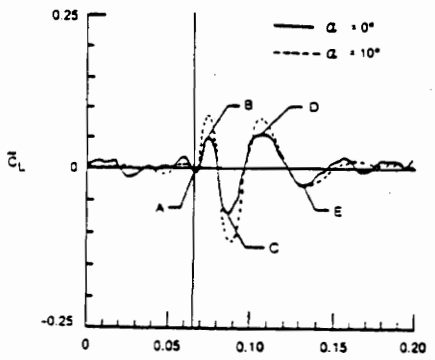

(d)

Figure 25. Lift coefficient as a function of time: (a) computed by the author; (b) computed by Lee and Smith (1987); (c) computed by Poling et al. (1988); (d) measured by Booth (1987).

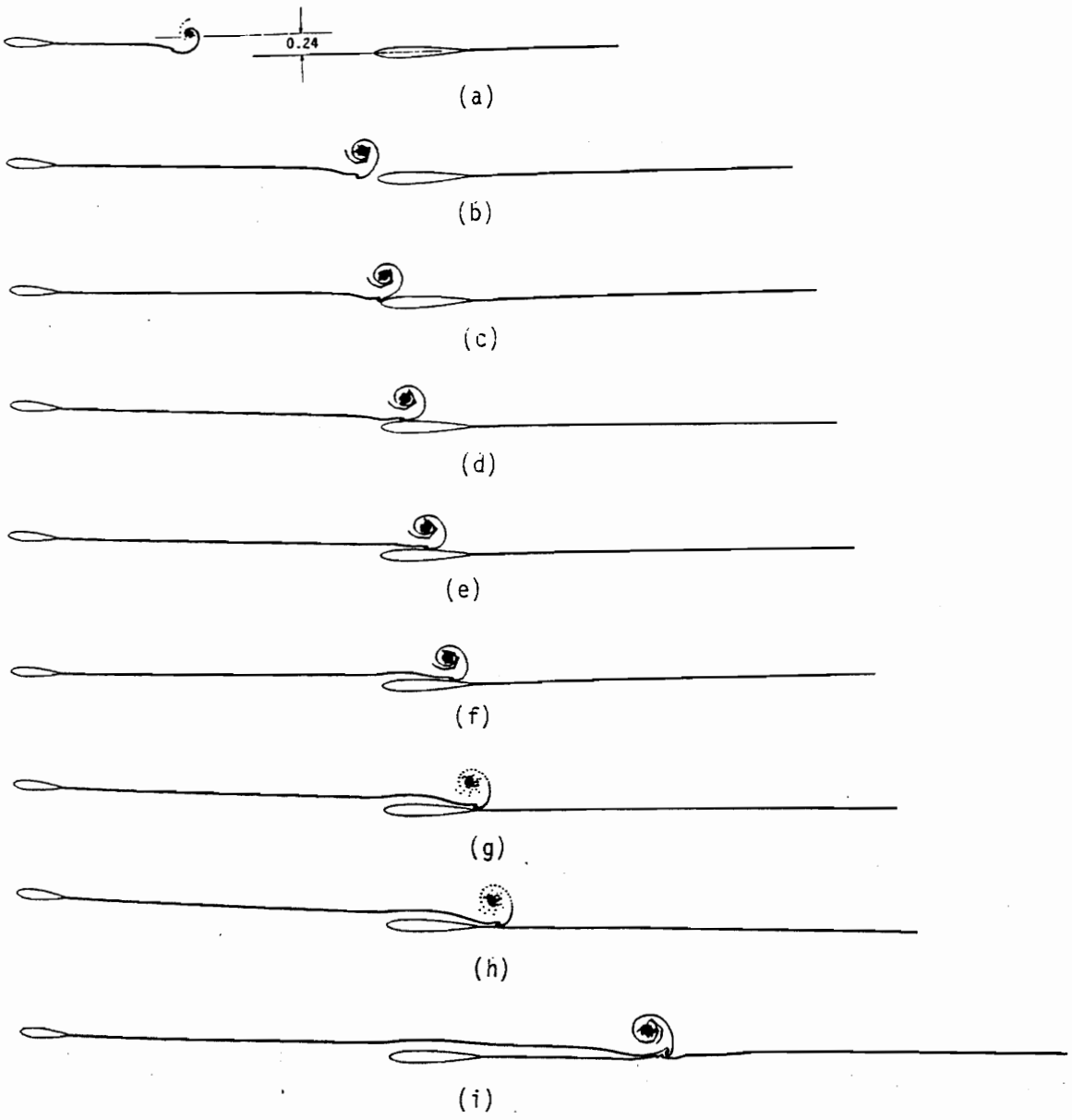

Figure 26. Blade-vortex interaction: numerical simulation of the experiment of Straus et al. (1990), and the pitch angle is defined in Equation (3.2.1). (a) at $t_1 = 1.59$; (b) at $t_2 = 3.38$; (c) at $t_3 = 3.58$; (d) at $t_4 = 3.78$; (e) at $t_5 = 3.98$; (f) at $t_6 = 4.18$; (g) at $t_7 = 4.38$; (h) at $t_8 = 4.58$; (i) at $t_9 = 6.17$.

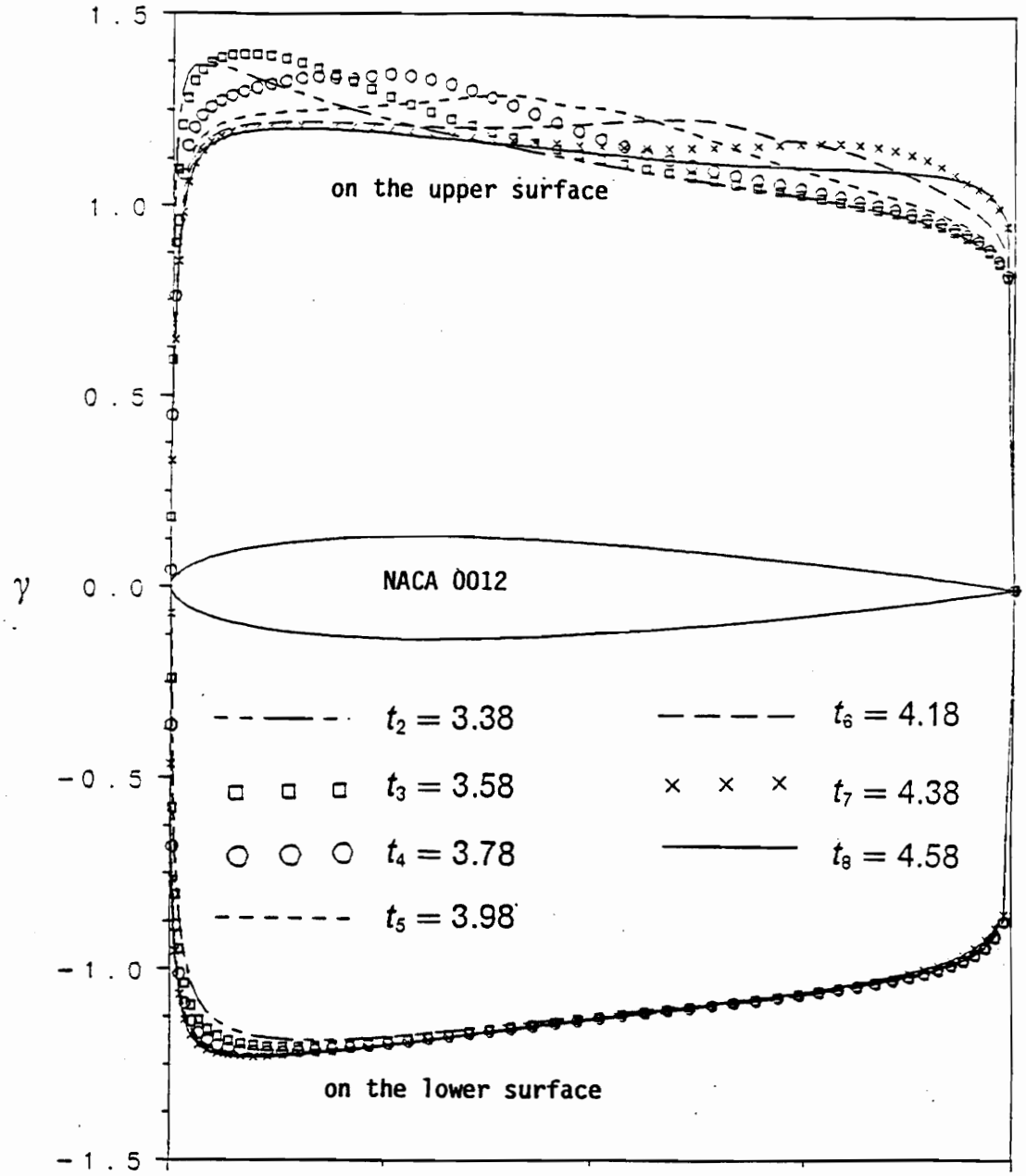

Figure 27. Surface velocities during the interaction for the same case as in Figure 26: at times t_2, t_3, t_4, t_5, t_6, t_7, t_8.

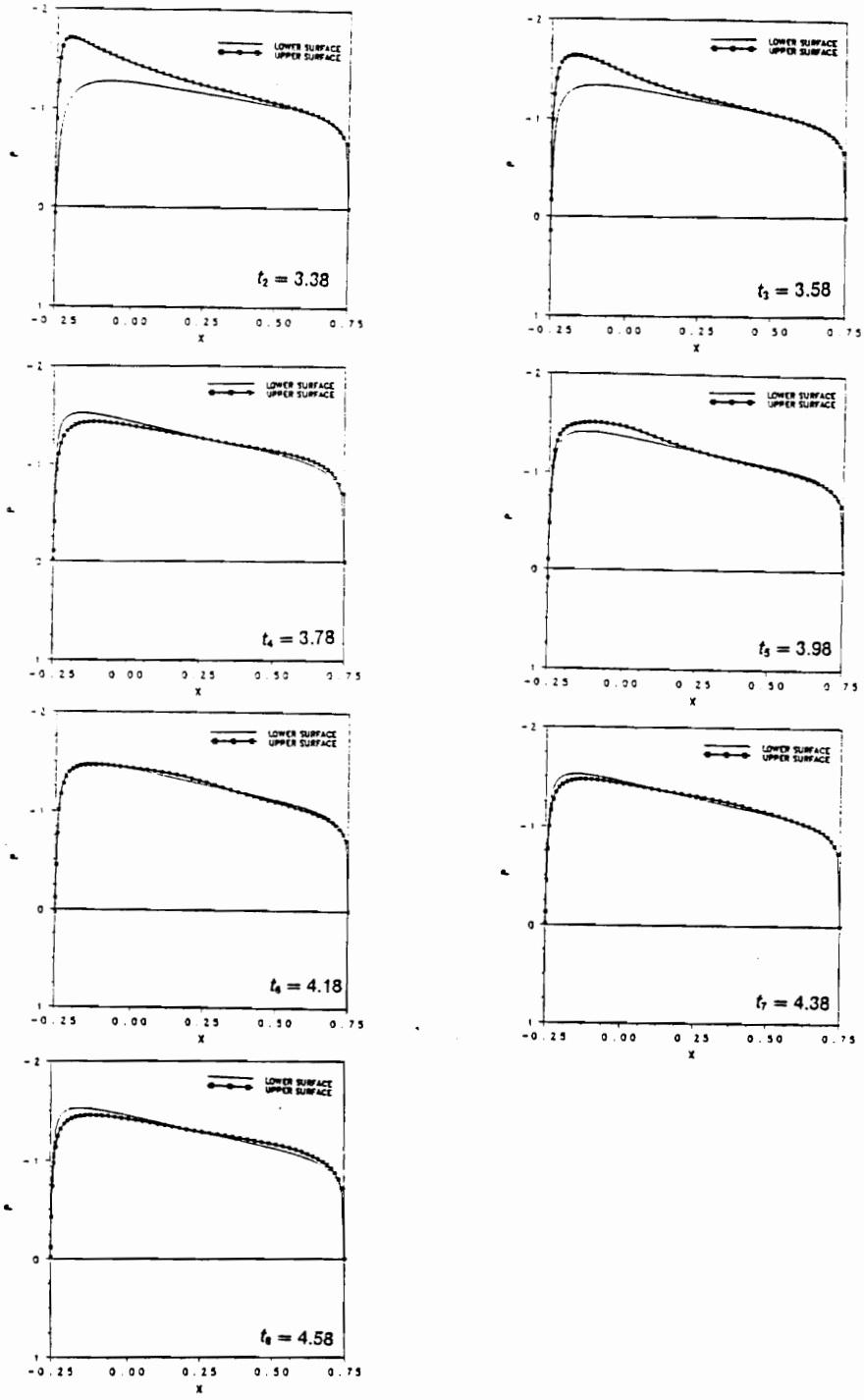

Figure 28. Pressure distributions on the stationary airfoil during the interaction for the same case as in Figure 26: at times t_2, t_3, t_4, t_5, t_6, t_7, t_8.

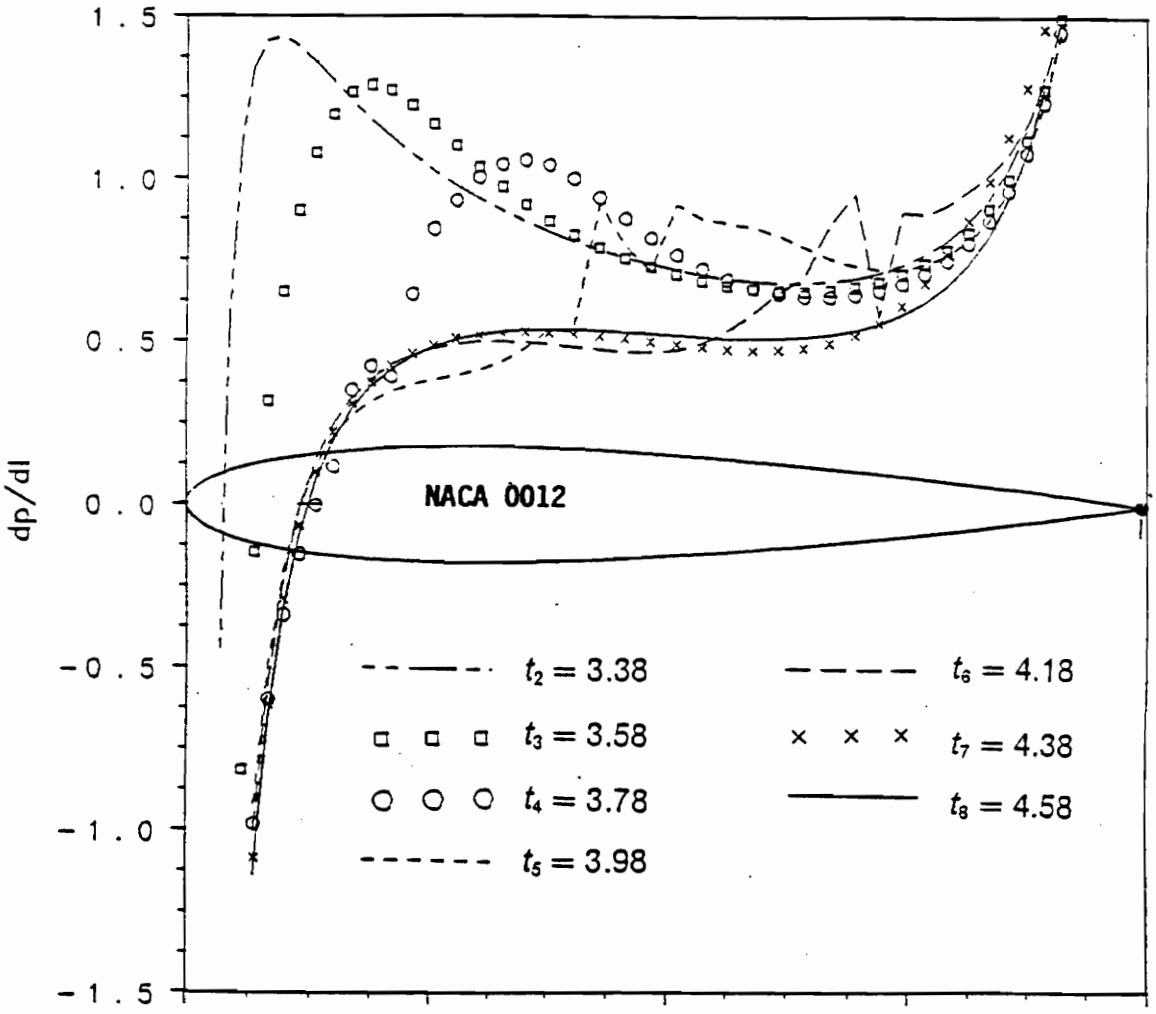

Figure 29. **Pressure gradients on the stationary airfoil during the interaction for the same case as in Figure 26:** at times t_2, t_3, t_4, t_5, t_6, t_7, t_8.

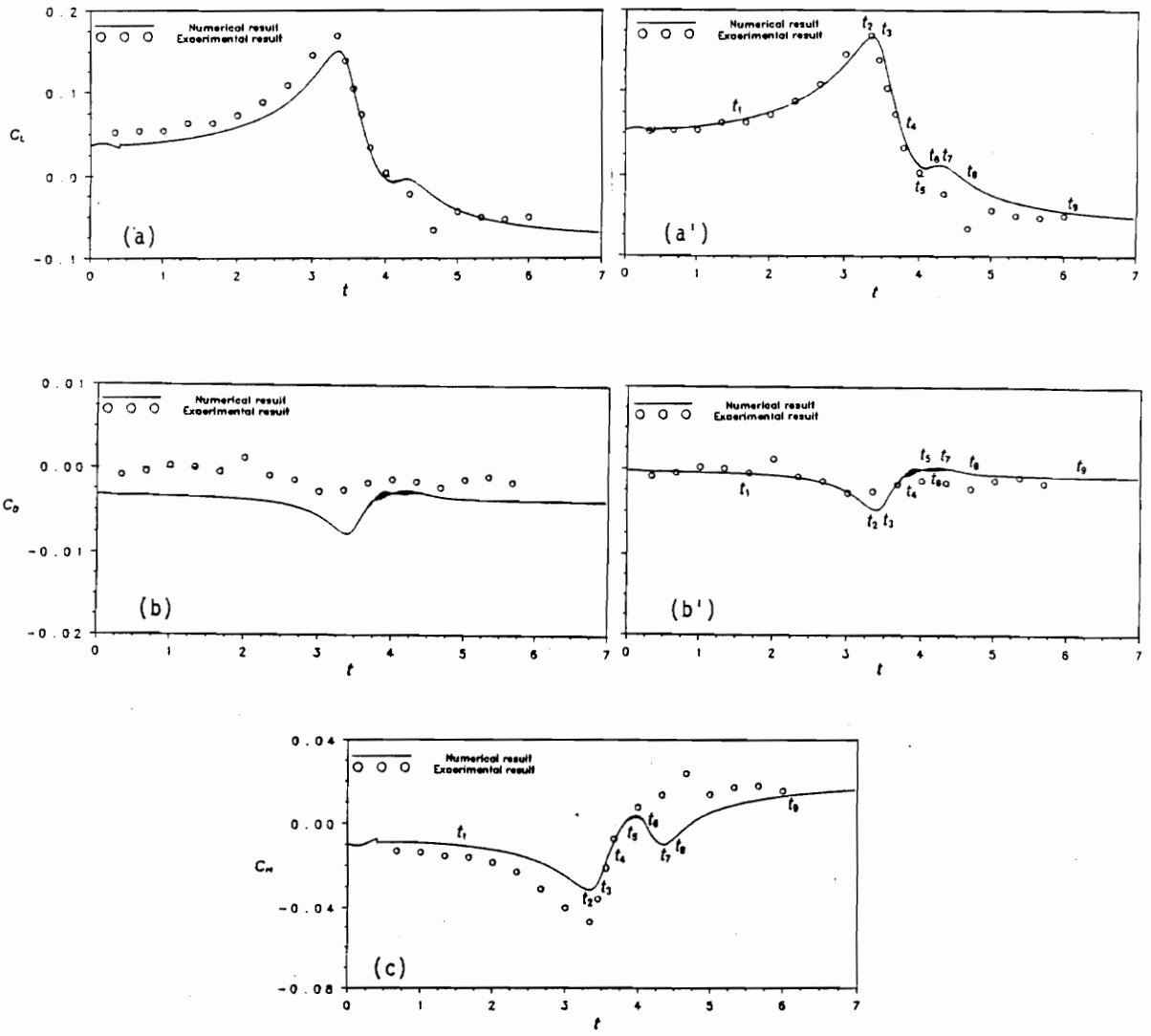

Figure 30. Histories of the aerodynamic loads on the stationary airfoil for the same case as in Figure 26: comparison between the numerical and experimental results. (a) Lift coefficient; (a') the computed lift coefficient is shifted up 0.017; (b) drag coefficient (b') the computed drag coefficient is shifted up 0.003; (c) moment coefficient (positive when clockwise about the leading edge).

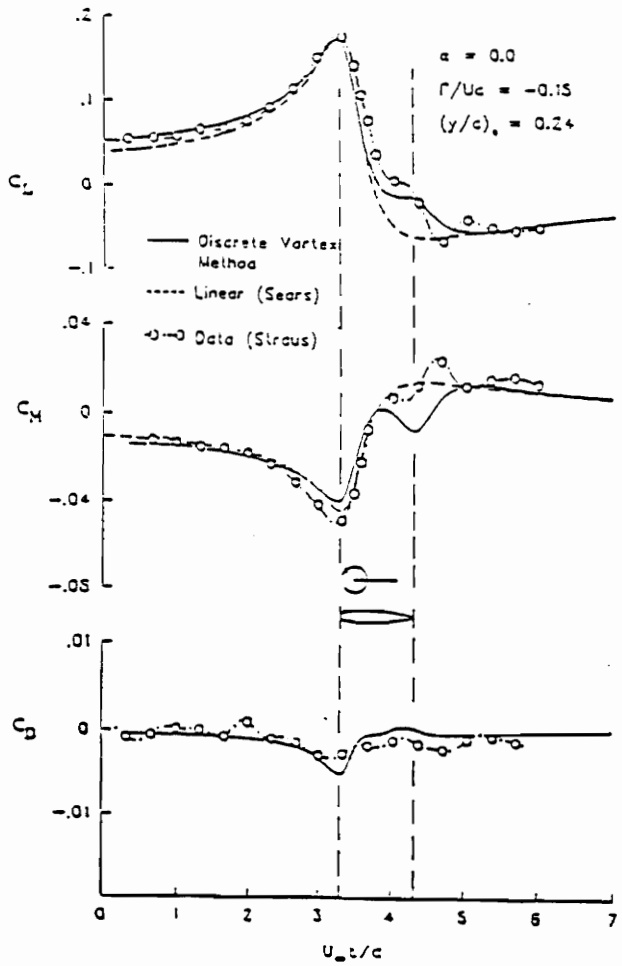

Figure 31. Comparison between experimental and numerical results given by Straus et al. (1990) for the same case as the one in Figure 30.

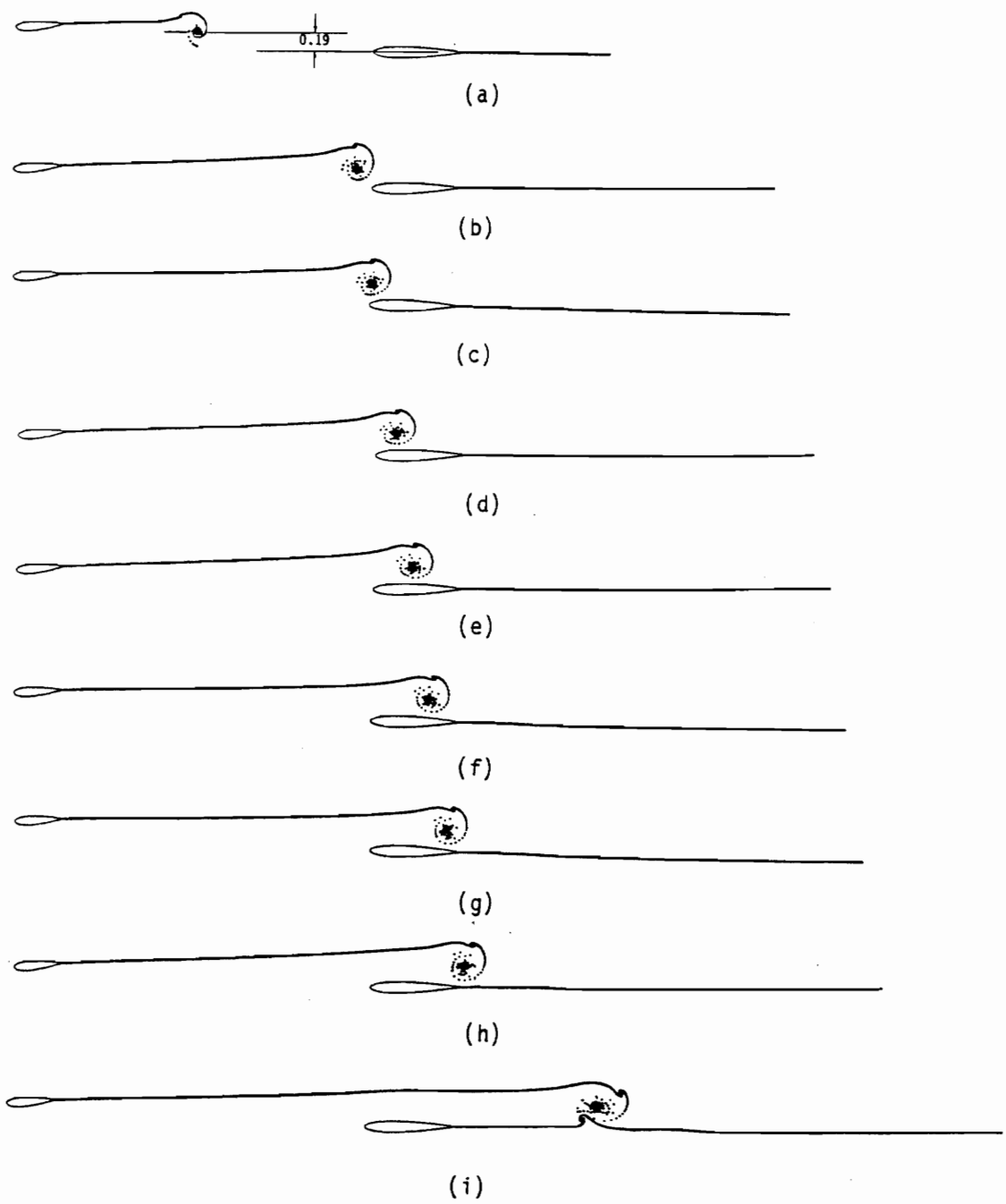

Figure 32. **Blade-vortex interaction:** numerical simulation of the experiment of Straus et al. (1990), and the pitch angle is defined in Equation (3.2.2). (a) at $t_1 = 1.59$; (b) at $t_2 = 3.38$; (c) at $t_3 = 3.58$; (d) at $t_4 = 3.78$; (e) at $t_5 = 3.98$; (f) at $t_6 = 4.18$; (g) at $t_7 = 4.38$; (h) at $t_8 = 4.58$; (i) at $t_9 = 6.17$.

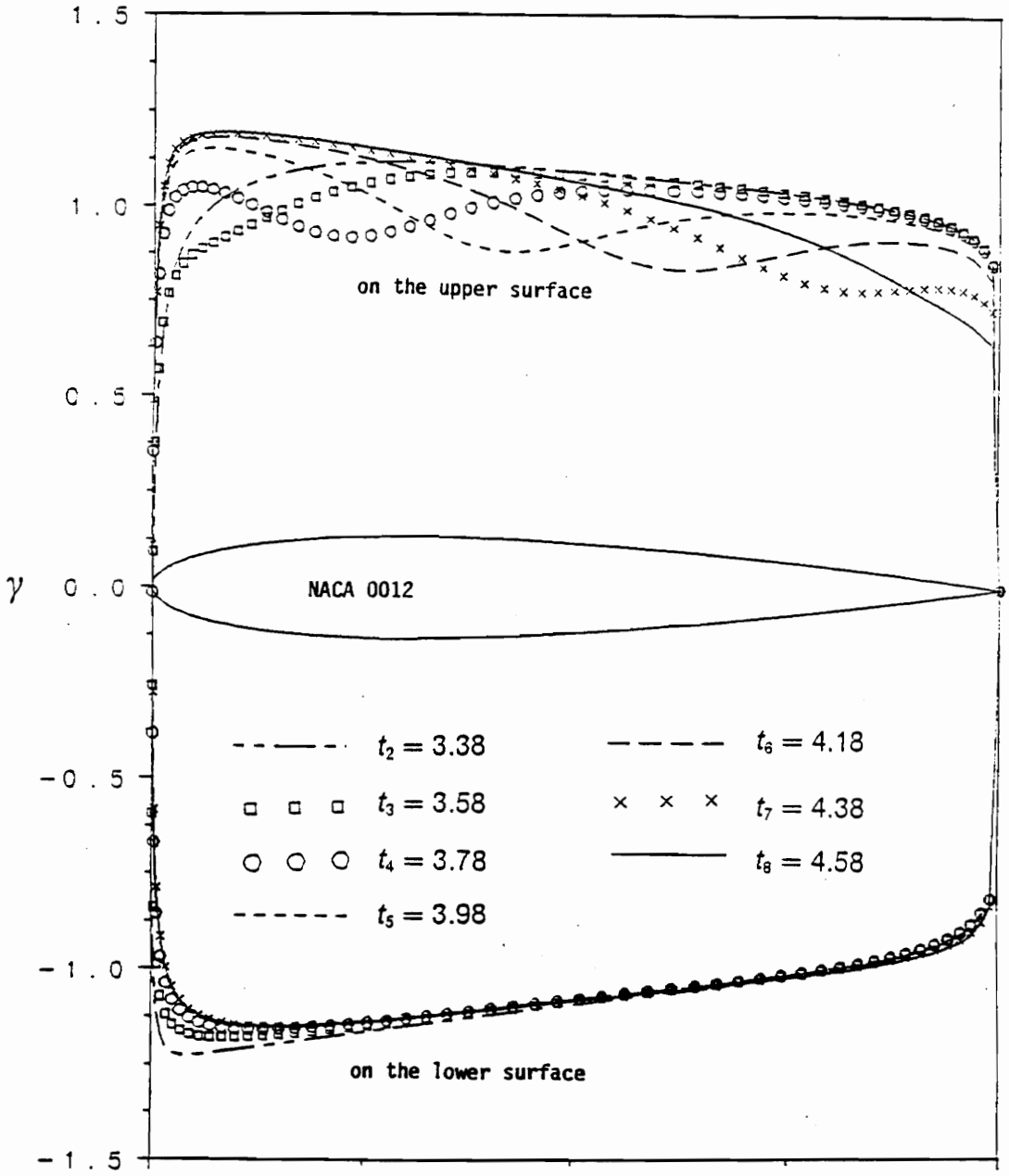

Figure 33. Surface velocities during the interaction for the same case as in Figure 32: at times t_2, t_3, t_4, t_5, t_6, t_7, t_8.

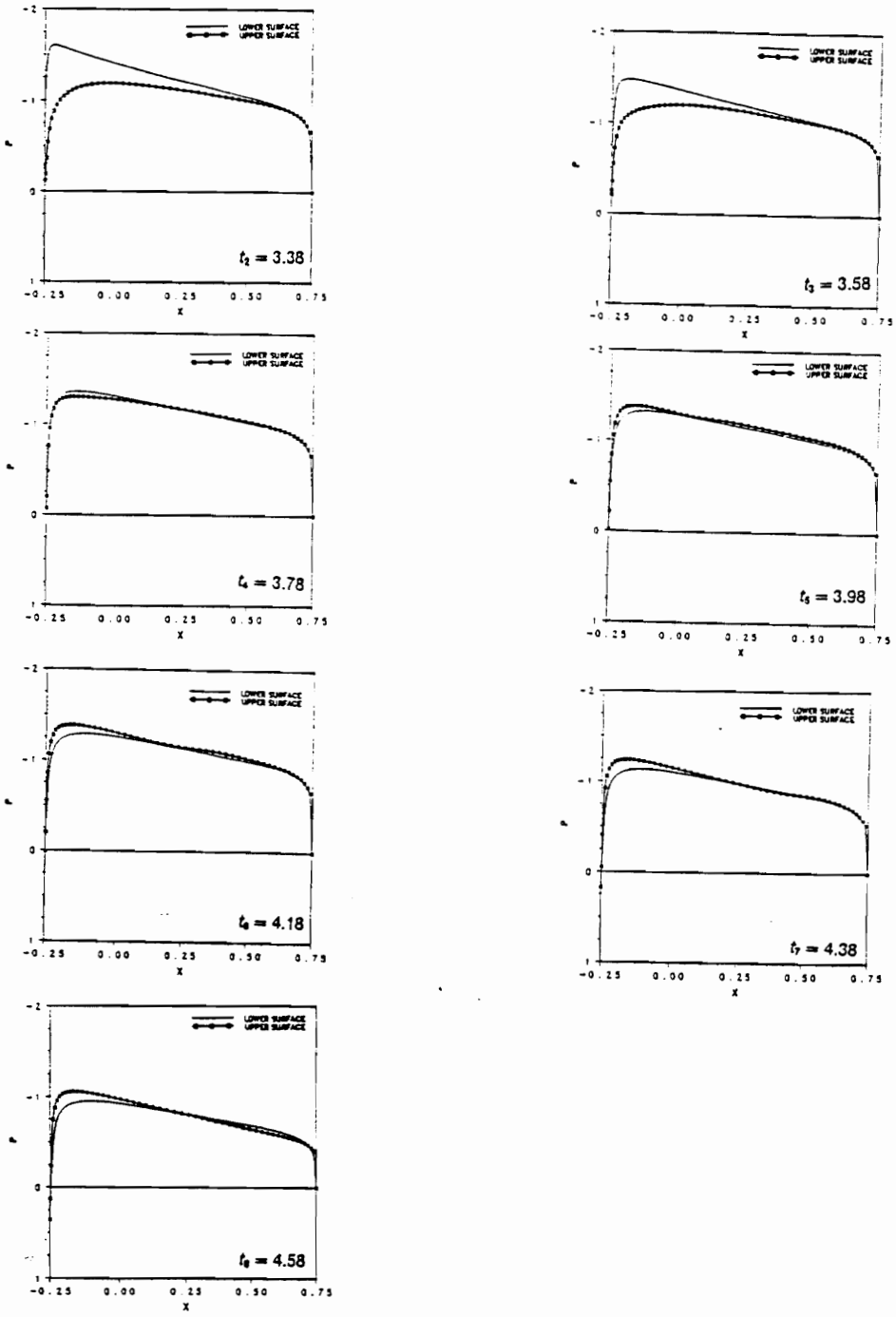

Figure 34. **Pressure distributions on the stationary airfoil during the interaction for the same case as in Figure 32:** at times t_2, t_3, t_4, t_5, t_6, t_7, t_8.

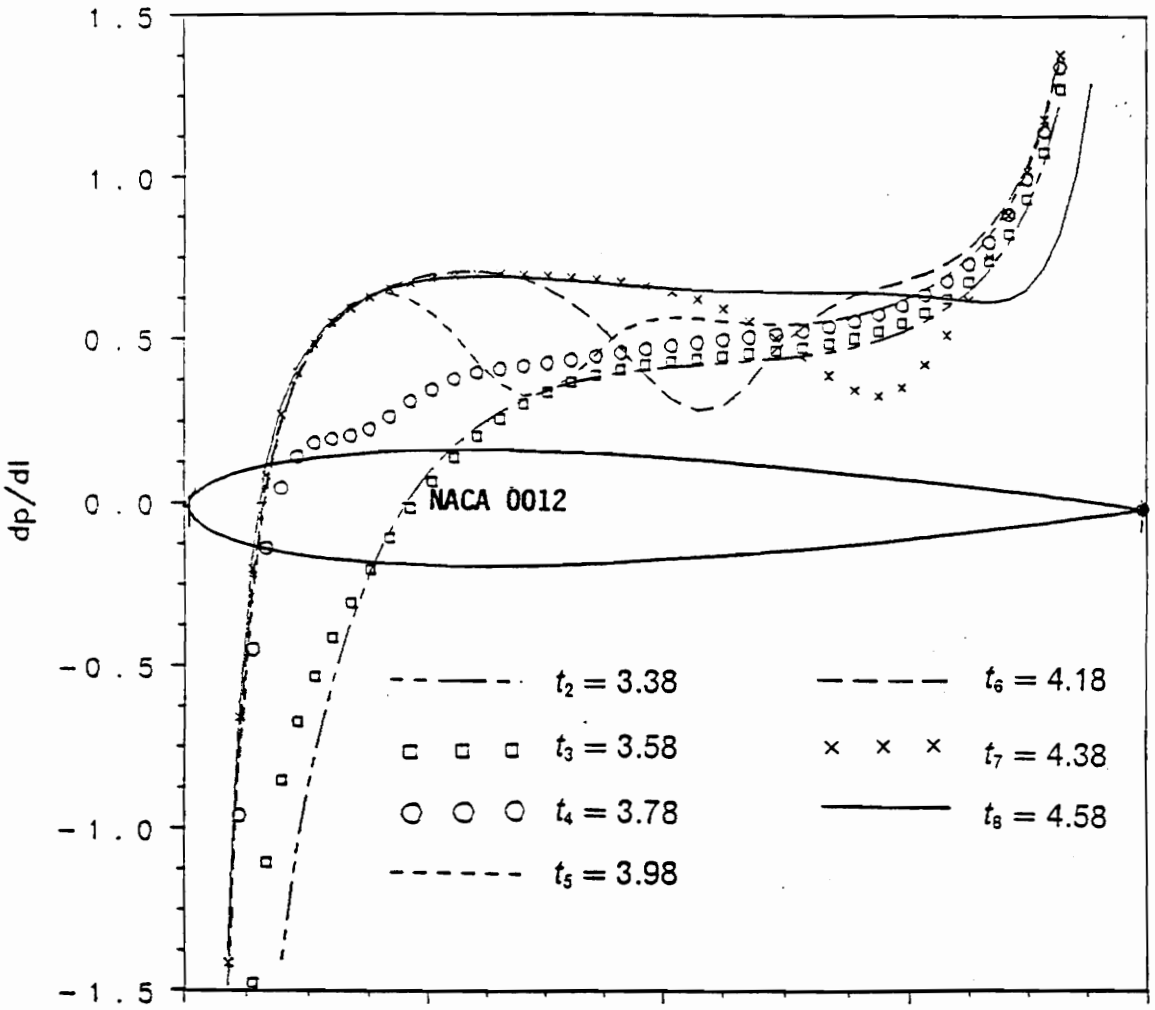

Figure 35. Pressure gradients on the stationary airfoil during the interaction for the same case as in Figure 32: at times t_2, t_3, t_4, t_5, t_6, t_7, t_8.

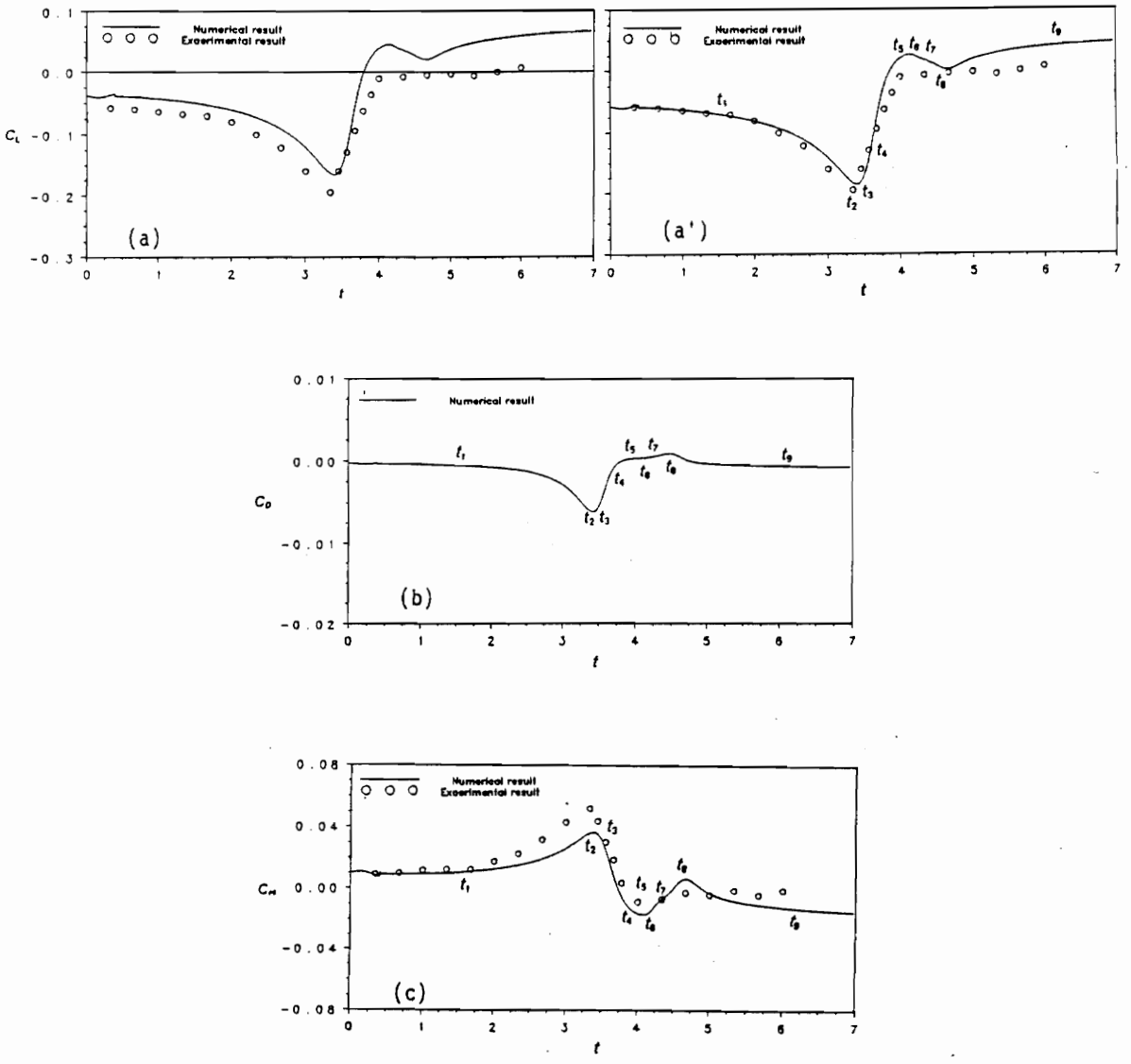

Figure 36. Histories of the aerodynamic loads on the stationary airfoil for the same case as in Figure 32: comparison between the numerical and experimental results. (a) Lift coefficient and the numerical curve is shifted up 0.017 in (a'); (b) drag coefficient; (c) moment coefficient (positive when clockwise about the leading edge).

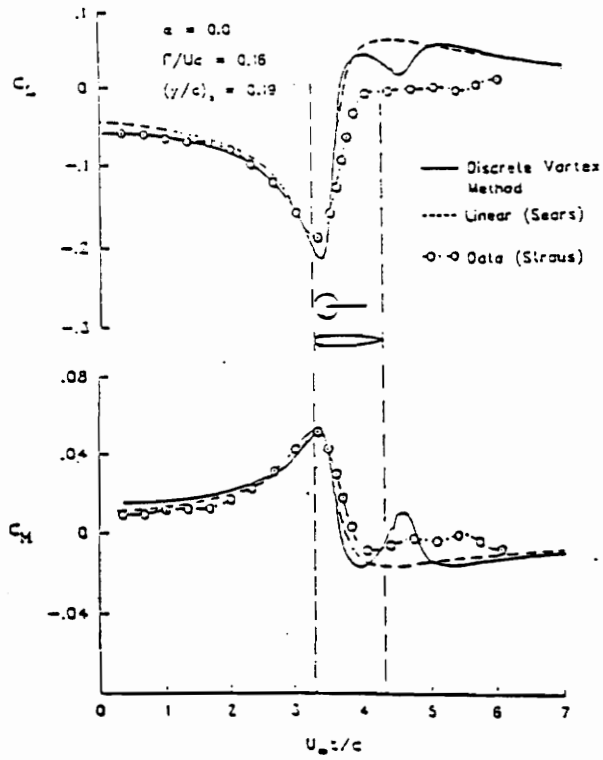

Figure 37. Comparison between experimental and numerical results given by Straus et al. (1990) for the same case as the one in Figure 36.

Chapter 4. Equations of Motion and Feedback Control

In this chapter, the dynamic model for the motion of a large-aspect-ratio (the flow is treated as 2-D) rigid wing with a trailing-edge flap mounted on a elastic support is developed. And then feedback control is added to the system to manipulate the trailing-edge flap for the purpose of flutter suppression. In Chapter 5, it is demonstrated that the present model can imitate a wing in flutter. Then it is shown that a control law can be developed to command the flap and suppress the flutter motion as well as the response to a wind gust. Consideration is limited to incompressible, attached flows.

In classical flutter analyses of 2-D airfoils, the differential equations of motion are derived by assuming that the pitch angle is small, linearizing the inertial terms, treating the airfoil as a flat plate, and approximating the aerodynamic loads by Wagner's function. In the present work, the nonlinear equations of motion are used, and the aerodynamic loads are obtained by a general unsteady vorticity-panel method for incompressible flow. It is emphasized that with the present approach the aerodynamic loads, the motion of the airfoil, the deflections of the flap (control surface at the trailing edge), and the wake are predicted simultaneously and interactively by the solution.

4.1 Coordinate Systems

The system is modelled as shown in Figure 38: an airfoil with two degrees of freedom can move in plunge and pitch. The half chord length is b . The elastic axis is located at point E, and the mass center is located at point C. If both points E and C are on the chord line, then $a_h b$ is the distance from the point of midchord to point E, and $x_\alpha b$ is the distance from point E to point C; a_h and x_α are positive when measured toward the trailing edge of the airfoil.

As shown in Figure 38, a global coordinate system (X, Y) is set up with unit vectors $\vec{E}_X$ and $\vec{E}_Y$. Point E has no motion in the X-direction, and the plunging displacement of point E is denoted by y, positive in the upward direction. The time-dependent pitch angle measured from the static angle of attack α is denoted by θ, positive with the nose down (counterclockwise direction).

For convenience, a local coordinate system (ξ, η) fixed on the airfoil is introduced with unit vectors $\vec{e}_x$ and $\vec{e}_y$. Its origin is located at point E, and the ξ-axis points toward the trailing edge and is parallel to the chord line. The relation between the global and local systems is

$$\begin{Bmatrix} \vec{e}_x \\ \vec{e}_y \end{Bmatrix} = \begin{bmatrix} \cos(\alpha - \theta) & -\sin(\alpha - \theta) \\ \sin(\alpha - \theta) & \cos(\alpha - \theta) \end{bmatrix} \begin{Bmatrix} \vec{E}_X \\ \vec{E}_Y \end{Bmatrix} \tag{4.1.1}$$

The angular velocity and angular acceleration of the airfoil are

$$\begin{aligned} \vec{\omega}_a &= \dot{\theta}\vec{e}_z = \dot{\theta}\vec{E}_Z \\ \dot{\vec{\omega}}_a &= \ddot{\theta}\vec{e}_z = \ddot{\theta}\vec{E}_Z \end{aligned} \tag{4.1.2}$$

where $\vec{e}_z = \vec{e}_x \times \vec{e}_y$, $\vec{E}_Z = \vec{E}_X \times \vec{E}_Y$, and they are parallel.

The acceleration of point E is

$$\vec{a}_a = \ddot{y}\,\vec{E}_Y \tag{4.1.3}$$

where y is the vertical displacement of point E.

4.2 Aerodynamic Loads

In the present model, it is assumed that the flow always remains attached. Then the aerodynamic loads are calculated by using the method discussed in Chapter 2. For the 2-D problem considered here, using Equations (4.1.2) and (4.1.3), and one can rewrite Equation (2.6.1) as

$$p(\ell) - p_t(t) = p_0 + p_1\ddot{y} + p_2\ddot{\theta} + p_3\dot{\theta}^2 \tag{4.2.1}$$

where

$$p_0 = -\rho\left[\frac{d}{dt}\int_0^{\ell}\gamma d\ell + \frac{\gamma(\ell)^2 - \gamma_L^2}{2}\right] \tag{4.2.2a}$$

$$p_1 = -\rho\int_0^{\ell}(\vec{E}_Y \bullet \vec{e}_\ell)\,d\ell \tag{4.2.2b}$$

$$p_2 = -\rho\int_0^{\ell}[(\vec{E}_Z \times \vec{r}) \bullet \vec{e}_\ell]\,d\ell \tag{4.2.2c}$$

$$p_3 = -\rho\int_0^{\ell}(-\vec{r} \bullet \vec{e}_\ell)\,d\ell \tag{4.2.2d}$$

where $\vec{e}_\ell$ and $\vec{r}$ are the same as defined in Equations (2.4.1) and (2.6.1), and p_t is the pressure at the trailing edge. It is noted that p_1, p_2, and p_3 are time independent.

When the relative velocity γ on the surface of the airfoil and the position of the airfoil, y and θ, are known, p_0, p_1, p_2 and p_3 can be evaluated and the aerodynamic loads, F_Y^a (lift) and F_θ^a (moment) can be written as the following form

$$\begin{Bmatrix} F_Y^a \\ F_\theta^a \end{Bmatrix} = \begin{Bmatrix} F_{0Y}^a \\ F_{0\theta}^a \end{Bmatrix} + \ddot{y}\begin{Bmatrix} F_{1Y}^a \\ F_{1\theta}^a \end{Bmatrix} + \ddot{\theta}\begin{Bmatrix} F_{2Y}^a \\ F_{2\theta}^a \end{Bmatrix} + \dot{\theta}^2\begin{Bmatrix} F_{3Y}^a \\ F_{3\theta}^a \end{Bmatrix} \tag{4.2.3}$$

where

$$\begin{aligned}
F_Y^a &= -\oint_C p\, n_y\, d\ell\,, \quad & F_\theta^a &= -\vec{E}_Z \cdot [\oint_C p\, (\vec{r} \times \vec{n}) d\ell] \\
F_{0Y}^a &= -\oint_C p_0\, n_y\, d\ell\,, \quad & F_{0\theta}^a &= -\vec{E}_Z \cdot [\oint_C p_0\, (\vec{r} \times \vec{n}) d\ell] \\
F_{1Y}^a &= -\oint_C p_1\, n_y\, d\ell\,, \quad & F_{1\theta}^a &= -\vec{E}_Z \cdot [\oint_C p_1\, (\vec{r} \times \vec{n}) d\ell] \\
F_{2Y}^a &= -\oint_C p_2\, n_y\, d\ell\,, \quad & F_{2\theta}^a &= -\vec{E}_Z \cdot [\oint_C p_2\, (\vec{r} \times \vec{n}) d\ell] \\
F_{3Y}^a &= -\oint_C p_3\, n_y\, d\ell\,, \quad & F_{3\theta}^a &= -\vec{E}_Z \cdot [\oint_C p_3\, (\vec{r} \times \vec{n}) d\ell]
\end{aligned} \tag{4.2.4}$$

where $\vec{n} = n_X \vec{E}_X + n_Y \vec{E}_Y$ is the unit outward-pointing normal vector on the surface of the airfoil and the line integral is carried out around the contour of the airfoil, C, in clockwise direction. It is noted that $\oint_C p_t \vec{n} d\ell$ and $\oint_C p_t (\vec{r} \times \vec{n}) d\ell$ are always zero; hence the actual value of p_t has no influence on the lift and moment. Consequently, one can put $p_t(t) \equiv 0$.

If the airfoil is a flat plate, one has

$$\begin{Bmatrix} F_Y^a \\ F_\theta^a \end{Bmatrix} = -\begin{Bmatrix} \int_0^{\ell_{lea.}} \Delta p n_y\, d\ell - F_S\, \tau_y \\ \vec{K} \cdot \int_0^{\ell_{lea.}} \Delta p (\vec{r} \times \vec{n})\, d\ell \end{Bmatrix} \tag{4.2.5}$$

where Δp is given by Equation (2.6.4), F_S is given by Equation (2.6.6), the integral is carried out from the trailing edge to the leading edge along the flat airfoil, $\tau_x\vec{E}_X + \tau_y\vec{E}_Y$ is the unit vector pointing toward the trailing edge, and $\vec{n} = -\tau_y\vec{E}_X + \tau_x\vec{E}_Y$ is the unit vector pointing from the lower surface to the upper surface of the flat airfoil.

4.3 Equations of Motion

The equations of motion are as follows

$$m\{\ddot{y} + [\xi_C \cos(\alpha - \theta) + \eta_C \sin(\alpha - \theta)]\ddot{\theta}\} = F_Y \\ - m\,[\xi_C \sin(\alpha - \theta) - \eta_C \cos(\alpha - \theta)]\dot{\theta}^2 \tag{4.3.1}$$

$$m\,[\xi_C \cos(\alpha - \theta) + \eta_C \sin(\alpha - \theta)]\ddot{y} + I_E\,\ddot{\theta} = F_\theta \tag{4.3.2}$$

where m is the mass of the airfoil per unit span, (ξ_C, η_C) are the coordinates of the mass center in the body-fixed system, I_E is the moment of inertia about point E, F_Y is the total force on the airfoil in the Y-direction (plunge), positive in the upward direction, and F_θ is the total moment acting about point E, positive in the counterclockwise direction.

Equations. (4.3.1) and (4.3.2) can be solved numerically when the loads are given. In the absence of structural damping, the loads are composed of three parts

$$\begin{Bmatrix} F_Y \\ F_\theta \end{Bmatrix} = \begin{Bmatrix} F_Y^g \\ F_\theta^g \end{Bmatrix} + \begin{Bmatrix} F_Y^e \\ F_\theta^e \end{Bmatrix} + \begin{Bmatrix} F_Y^a \\ F_\theta^a \end{Bmatrix} \tag{4.3.3}$$

where the superscript g represents gravitational forces, the superscript e represents the elastic restoring forces and the superscript a represents the aerodynamic loads given in Equation (4.2.3) or (4.2.5).

The gravitational forces are nonlinear and given by

$$\begin{Bmatrix} F_Y^g \\ F_\theta^g \end{Bmatrix} = - \begin{Bmatrix} mg \\ mg[\xi_C \cos(\alpha - \theta) + \eta_C \sin(\alpha - \theta)] \end{Bmatrix} \tag{4.3.4}$$

where g is the acceleration due to gravity

The elastic forces are taken in the form

$$\begin{Bmatrix} F_Y^e \\ F_\theta^e \end{Bmatrix} = - \begin{Bmatrix} k_1^y y \\ k_1^\theta \theta \end{Bmatrix} + \ldots \tag{4.3.5}$$

which can include arbitrary nonlinear terms in both y and θ . Two frequencies are defined as follows

$$\omega_y = \sqrt{\frac{k_1^y}{m}} \quad \text{and} \quad \omega_\theta = \sqrt{\frac{k_1^\theta}{I_E}} \tag{4.3.6}$$

It is obvious that ω_y and ω_θ are, respectively, the natural frequencies of the vibration described by the following two uncoupled equations of motion

$$m\,\ddot{y} + k_1^y\, y = 0 \tag{4.3.7}$$

$$I_E\,\ddot{\theta} + k_1^\theta\,\theta = 0 \tag{4.3.8}$$

With Equation (4.3.3) and Equation (4.2.3), Equation (4.3.1) and Equation (4.3.2) can be rewritten in matrix form

$$\begin{bmatrix} m - F_{1Y}^a & m[\xi_C \cos(\alpha - \theta) + \eta_C \sin(\alpha - \theta)] - F_{2Y}^a \\ m[\xi_C \cos(\alpha - \theta) + \eta_C \sin(\alpha - \theta)] - F_{1\theta}^a & I_E - F_{2\theta}^a \end{bmatrix} \begin{Bmatrix} \ddot{y} \\ \ddot{\theta} \end{Bmatrix}$$

$$= \begin{Bmatrix} F_Y^g \\ F_\theta^g \end{Bmatrix} + \begin{Bmatrix} F_Y^e \\ F_\theta^e \end{Bmatrix} + \begin{Bmatrix} F_{0Y}^a \\ F_{0\theta}^a \end{Bmatrix} + \dot{\theta}^2 \begin{Bmatrix} F_{3Y}^a + m[\eta_C \cos(\alpha - \theta) - \xi_C \sin(\alpha - \theta)] \\ F_{3\theta}^a \end{Bmatrix} \tag{4.3.9}$$

4.4 Numerical Procedure

To calculate the motion of the airfoil, one must know the loads, while one must know the motion to calculate the loads. Therefore, the problem should be solved simultaneously and interactively.

Hamming's fourth-order predictor-corrector method (Carnahan et al. 1969) is chosen to integrate Equation (4.3.9). The choice was motivated by the fact that the method requires calculations at only integral values of the time step, which is important for the aerodynamic model of the wake. Equation (4.3.9) can be rewritten as four first-order ordinary-differential equations as follows

$$\dot{y}_i = f_i(y_1, y_2, y_3, y_4) \qquad for \quad i = 1, 2, 3, 4 \tag{4.4.1}$$

where $y_1 = y$, $y_2 = \dot{y}$, $y_3 = \theta$, $y_4 = \dot{\theta}$. The method needs information from the four previous steps to predict the solution of Equation (4.3.9) at the current step. This predicted solution is used to evaluate the right-hand side of the equations. Then with the new right-hand side and the information from the four previous steps, the solution is corrected. The correction is repeated until the difference between two successive iterations is less than a specified bound. The vortices in the flowfield are convected at the speed of local fluid particles at the beginning of each time step. Each time the current aerodynamic loads are needed, the algorithm calls the subroutine that contains the aerodynamic model and the flowfield is recalculated. The details of the numerical procedure are given next:

1. Let t_j denote the time at the j^{th} step, and

$$\begin{aligned} y_{i,j} &= y_i(t_j) \\ f_{i,j} &= f_i(y_{1,j}, y_{2,j}, y_{3,j}, y_{4,j}) \end{aligned} \tag{4.4.2}$$

For $i = 1, 2, 3, 4$, it is assumed that $y_{i,j}$, $y_{i,j-1}$, $y_{i,j-2}$, $y_{i,j-3}$, $f_{i,j}$, $f_{i,j-1}$, $f_{i,j-2}$ are already known from calculations at previous time steps, and that the local truncation errors, $e_{i,j}$, which will be given later, are also available.

2. The predicted solutions at the next step are given by the predictor equations

$$y^p_{i,j+1} = y_{i,j-3} + \frac{4}{3}\Delta t(2f_{i,j} - f_{i,j-1} + 2f_{i,j-2}) \quad \text{for } i = 1, 2, 3, 4 \quad (4.4.3)$$

where Δt is the time-step size

3. The predicted solutions are modified by the local truncation errors:

$$y^1_{i,j+1} = y^p_{i,j+1} + \frac{112}{9} e_{i,j} \quad (4.4.4)$$

4. The modified-predicted solutions are corrected by the corrector equations

$$y^{k+1}_{i,j+1} = \frac{1}{8}[9y_{i,j} - y_{i,j-2} + 3\Delta t(f^k_{i,j+1} + 2f_{i,j} - f_{i,j-1})] \quad \text{for } k \leq 1 \quad (4.4.5)$$

where k is the iteration number, and

$$f^k_{i,j+1} = f_i(y^k_{1,j+1}, y^k_{2,j+1}, y^k_{3,j+1}, y^k_{4,j+1}) \quad (4.4.6)$$

In Equation (4.4.6), the aerodynamic loads are those computed for the latest estimates of positions and velocities of the airfoil by using the aerodynamic model discussed in Chapter 2.

5. The Equations (4.4.5) and (4.4.6) are repeatedly applied until all of the $|y^{k+1}_{i,j+1} - y^k_{i,j+1}|$ (for $i = 1, 2, 3, 4$) are less than a prescribed error tolerance.

6. The local truncation errors are estimated for use in the current and next step

$$e_{i,j+1} = \frac{9}{121}\,(y^{k+1}_{i,j+1} - y^{p}_{i,j+1}) \qquad \text{for } i = 1, 2, 3, 4 \qquad (4.4.7)$$

7. Then the final solutions at the current step are

$$y_{i,j+1} = y^{k+1}_{i,j+1} - e_{i,j+1} \qquad \text{for } i = 1, 2, 3, 4 \qquad (4.4.8)$$

The entire procedure is based on the availability of the solutions at four previous time steps. In the calculation of the first four steps the local truncation error is not used, i.e. $e_{i,j} = 0$. With the numerical scheme used by Nuhait (1988), the equations to compute the solutions at the first four steps are given as follows:

1. When $j = 1$, $y_{i,1}$ and $f_{i,1}$ (for $i = 1, 2, 3, 4$) are evaluated by the initial conditions.

2. When $j = 2$, the predicted solutions are computed by the Euler method

$$y^{1}_{i,2} = y_{i,1} + \Delta t\, f_{i,1} \qquad (4.4.9)$$

   The corrected solutions are computed by the modified Euler method

$$y^{k+1}_{i,2} = y_{i,1} + \frac{\Delta t}{2}\,(f^{k}_{i,2} + f_{i,1}) \qquad (4.4.10)$$

   where k is the iteration number.

3. When $j = 3$, the predicted solutions are computed by Adams-Bashforth two-step predictor method

$$y^{1}_{i,3} = y_{i,2} + \frac{\Delta t}{2}\,(3f_{i,2} - f_{i,1}) \qquad (4.4.11)$$

   The corrected solutions are computed by the Adams-Moulton two-step method

$$y_{i,3}^{k+1} = y_{i,2} + \frac{\Delta t}{12}\,(5f_{i,3}^{k} + 8f_{i,2} - f_{i,1}) \tag{4.4.12}$$

where k is the iteration number.

4. When $j = 4$, the predicted solutions are computed by Adams-Bashforth three-step predictor method

$$y_{i,4}^{1} = y_{i,3} + \frac{\Delta t}{12}\,(23f_{i,3} - 16f_{i,2} + 5f_{i,1}) \tag{4.4.13}$$

The corrected solutions are computed by the Adams-Moulton three-step method

$$y_{i,4}^{k+1} = y_{i,3} + \frac{\Delta t}{24}\,(9f_{i,4}^{k} + 19f_{i,3} - 5f_{i,2} + f_{i,1}) \tag{4.4.14}$$

where k is the iteration number.

5. For $j = 2,\ 3,\ 4$, after $|y_{i,j}^{k+1} - y_{i,j}^{k}|$ is less than a specified tolerance, the iteration stops and

$$y_{i,j} = y_{i,j}^{k+1} \tag{4.4.15}$$

6. The error for $j = 4$ is set equal to zero

$$e_{i,4} = 0 \tag{4.4.16}$$

for use in the integration when $j = 5$.

The aerodynamic model developed in Chapter 2 is coupled with the dynamic model, and then both are solved interactively and simultaneously. The procedure is given as follows:

1. The initial flow is specified, and all the loads on the airfoil are evaluated.

2. The time is advanced one step.

3. The wake is convected.

4. The predicted solutions for the motion of the airfoil at the new step are computed by Equation (4.4.3).

5. The predicted solutions are modified by Equation (4.4.4). The iteration number $k = 1$.

6. The values of γ at the nodes on the airfoil and Γ_t are computed.

7. All the loads on the airfoil are evaluated.

8. The corrected solutions for the motion of the airfoil are computed by Equation (4.4.5). The iteration number is $k = k + 1$.

9. The computing tolerance between the iterations $k + 1$ and k is checked. If it is not satisfied, the calculation is returned to step 6. If yes, the calculation moves to the step 10.

10. The final solutions at the current time step are obtained from Equation (4.4.8).

11. The values of γ at the nodes on the airfoil and Γ_t are updated.

12. All the loads on the airfoil are updated.

13. If the computation is to continue, the procedure returns to step 2. If it is not, the computation is stopped.

4.5 Feedback Control

As demonstrated later by some examples in Chapter 5, the critical flutter speed varies little when the airfoil is replaced by a flat plate. Then for the convenience of numerical calculation, a flat-plate airfoil is used in the study of flutter suppression.

To suppress the motions of the airfoil, a flap is added at the trailing edge as shown in Figure 39. The airfoil is approximated by a flat plate for computational convenience, and δ is the angle of the control flap relative to the airfoil and positive in the counterclockwise direction.

The control flap oscillates in a tailored manner governed by a control law. In general, it is assumed that the commanded angle δ_c is a function of the displacements and velocities of the airfoil:

$$\delta_c = \delta_e + a_1(y - y_e) + a_2\dot{y} + a_3(\theta - \theta_e) + a_4\dot{\theta} \tag{4.5.1}$$

where δ_e represents the equilibrium positions, which may or may not be stable. Here δ_c is a linear function of the displacements and velocities, but any nonlinear function could have been used.

For the problem of instantaneous control, the flap angle satisfies

$$\delta = \delta_c \tag{4.5.2}$$

This means that flap angle δ reaches the commanded angle δ_c in no time.

And for the delayed control, δ satisfies the following servo equation

$$\ddot{\delta} + c_1\dot{\delta} + c_2(\delta - \delta_c) = 0 \tag{4.5.3}$$

where c_1 and c_2 are constants. The larger c_2 is, the faster δ approaches δ_c. In this sense, instantaneous control is the extreme case when c_2 goes to infinity. In this dissertation, the range over which δ varies is limited to $\pm \delta_{max}$. In other words, when Equation (4.5.3) calls for a δ such that $|\delta| > \delta_{max}$, it is imposed that $|\delta| = \delta_{max}$ and $\dot{\delta} = 0$. This servo equation and the control law are solved only by using the solution of Equation (4.4.1) at the previous step, in the same way that the vortices are convected.

4.6 Summary

A model capable of simulating the arbitrary motion of a rigid 2-D airfoil mounted on a nonlinear elastic support was developed. The aerodynamic model for calculating loads acting on the airfoil is nonlinear, and the equations of motion are nonlinear. To suppress the motions of the airfoil responding to some disturbances as well as flutter, a feedback control model was developed. The dynamic system, which includes airfoil, wake, elastic support and control devices, is considered integrally, i.e., the coupled aerodynamic-dynamic-control problems are solved simultaneously and interactively.

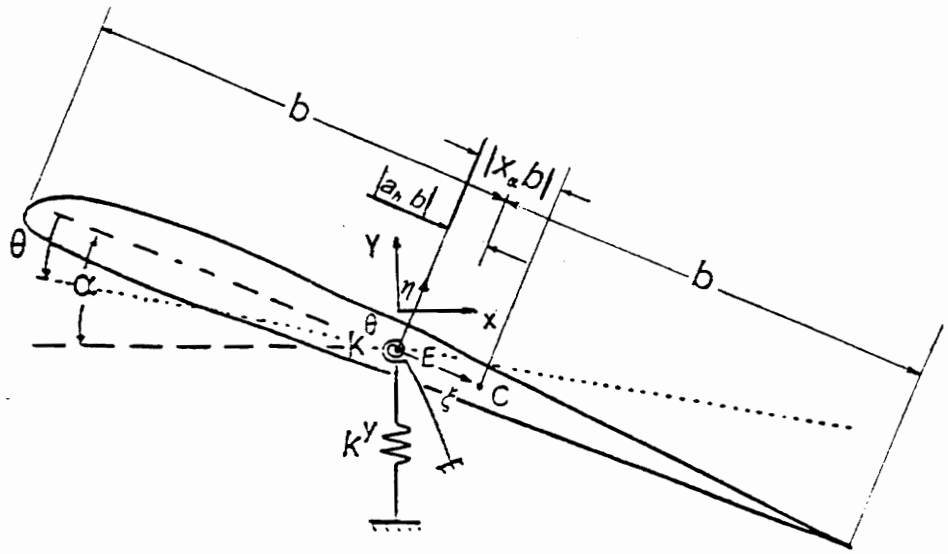

Figure 38. Setup for the two-degree-of-freedom dynamic system: airfoil and elastic supports.

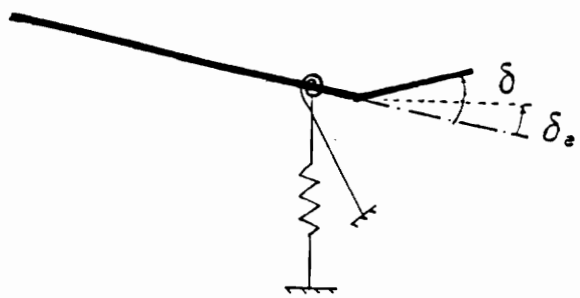

Figure 39. Setup for feedback control: flat-plate airfoil with a flap (control surface) hinged at the trailing. edge.

Chapter 5. Examples of Numerical Simulations of Flutter and Flutter Suppression by Feedback Control

In this chapter, numerical examples of flutter and flutter suppression by feedback control are presented.

When the equation of motion (4.3.9) is nondimensinalized, the following two dimensionless parameters appear:

$$r_\alpha = \sqrt{\frac{I_E}{mb^2}} = \text{radius of gyration about the elastic axis}$$

$$\mu = \frac{m}{\pi\rho b^2} = \text{mass ratio}$$

Throughout this chapter, some of the parameters defined in Chapter 4 are as follows: $b = 5$ in, $a_h = -0.15$, $x_\alpha = 0.25$, $r_\alpha^2 = 0.388$, $\mu = 76$, $\omega_y = 55.9$ rad/sec, and $\omega_\theta = 64.1$ rad/sec. The values of these parameters are taken from Fung's textbook (1969). As he calculated, the natural frequencies of the system (the case where the freestream speed V_∞ is zero) are $\omega_1 = 49.76$ rad/sec and $\omega_2 = 77.72$ rad/sec.

5.1 Simulation of Flutter

To check the present method of simulating unsteady aeroelastic behavior of 2-D airfoils, the present results are compared with those given by Fung (1969). Fung considered a flat plate and solved the linearized equations of motion with the aerodynamic loads being approximated by Wagner's function. The springs are linear, and there is no structural damping. For the cases where the static angle of attack $\alpha = 0$, and the initial conditions are $y(0) = 0$, $\dot{y}(0) = 0$, $\theta(0) = -5°$ and $\dot{\theta}(0) = 0$, y and θ as functions of time are shown in Figure 40. In part (a) of Figure 40, the freestream speed (V_∞) is 88 ft/sec. Both y and θ appear to be decaying with time to the values $y = y_e = 0.0093$ and $\theta = \theta_e = -0.93°$, which correspond to the static equilibrium position. The slow decay is due to the fact that V_∞ is near the flutter speed. In part (b) of Figure 40, $V_\infty = 89$ ft/sec, and y and θ appear to be neither growing nor decaying with time. Limit-cycle motions are possible for linear elastic restoring forces because the aerodynamic loads are inherently nonlinear. The fast Fourier transform shows that both y and θ have the same frequency $\omega_f = 63$ rad/sec, which satisfies the condition $\omega_1 \leq \omega_f \leq \omega_2$, a characteristic of flutter motion. In part (c) of Figure 40, $V_\infty = 90$ft/sec, and both y and θ are growing. Fung's analysis gives the flutter-onset speed as 90.1 ft/sec and the flutter frequency as 59.82 rad/sec. The agreement between the two sets of results is very close. The slight discrepancy between Fung's results and the present results is most likely due to the following: (1) Fung used Wagner's function to obtain the aerodynamic loads, and in the present analysis the general unsteady vorticity-panel method is used. (2) Fung considered oscillations around $\theta = 0°$, and in the present analysis the oscillations are approximately centered at an "equilibrium" position where $\theta \simeq 1°$.

Whether the oscillations decay, stay neutral, or grow depends on the energy exchange between the flow and the airfoil. For the motion of two degrees of freedom, the work done by the aerodynamic loads is

$$W = \int (F_L \, dy + F_M \, d\theta) \tag{5.1.1}$$

where F_L is the lift force and F_M is the moment.

According to Fung's discussion (1969), the airfoil with only one degree of freedom in plunge does not flutter because the lift always does negative work, and that, with only one degree of freedom in pitch, flutter happens only when the angle of attack is at or near the stalling angle or for some special mass distributions and positions of elastic axis. Here are two examples in which the airfoil is only allowed to move in plunge or in pitch and $V_\infty = 90$ ft/sec. In part (a) of Figure 41, the dimensionless lift is plotted as a function of vertical displacement y for the case where only the vertical motion is allowed, static angle of attack $\alpha = 5°$, and $y(0) = \dot{y}(0) = 0$. And in part (b) of Figure 41, the dimensionless moment is plotted as the function of θ for the case where only the motion in θ direction is allowed, $\alpha = 0$, $\theta(0) = -5°$ and $\dot{\theta}(0) = 0$. For both cases, the oscillations decay. The points representing the solution move in a counterclockwise direction, indicating that the work done by the aerodynamic loads is negative; hence the flow extracts energy from the motion of the airfoil, and the loads damp the motion.

For the two-degree-of-freedom motion, the phase difference between y and θ is the mechanism for the energy exchange between the airfoil and the flow (Fung, 1969; Niblett, 1988). Using the quasi-steady aerodynamic loads, Niblett showed that the sign of the work done by the lift depends on the sign of sin ψ per cycle

$$\int F_L \, dy = \pi \rho V_\infty^2 b \frac{dC_L}{d\alpha} \theta_0 y_0 \sin \psi \qquad (5.1.2)$$

where $\frac{dC_L}{d\alpha}$ is the rate of change of lift coefficient with angle of attack and is positive, θ_0 and y_0 are the magnitudes of θ and y, and ψ is the phase difference by which θ lags y. According to Equation (5.1.2), the lift can do either positive work or negative work depending on the phase difference ψ.

For $V_\infty = 88$ ft/sec, the plots of θ vs. y, lift vs. y, moment vs. θ and work vs. time are shown in Figure 42. In part (a), the motion decays, the points representing the solution move in the counterclockwise direction, and there is a phase difference between y and θ ($0 < \psi < \pi$). According to Equation (5.1.2), instead of doing negative work like in the case of only one degree of freedom in plunge shown in part (a) of Figure 41, the lift does positive work as shown in part (b) because the direction of the curve is clockwise, indicating the motion extracts energy through the lift. But as shown in part (c) of Figure 42, the moment does negative work because the direction of the curve is counterclockwise. As shown in part (d) Figure 42, the net work calculated by Equation (5.1.1) (the work done by both the lift and moment) is negative and decreases as the time proceeds. This indicates that the negative work prevails over the positive one and that the energy stored in the elastic supports initially is being dissipated by the aerodynamic damping until the motion of the airfoil stops.

Similar plots for $V_\infty = 89$ ft/sec and 90 ft/sec are shown in Figures 43 and 44, respectively. For both cases, there is a phase difference, and the lift does positive work while the moment does the opposite. When $V_\infty = 89$ ft/sec, as shown in part (d) of Figure 43, the work is negative initially but after t = 300 the work done over one period is zero, and on average, no more energy is extracted from or given to the airfoil. Hence, a limit cycle is reached as shown in parts (a), (b) and (c) of Figure 43. For $V_\infty = 90$ ft/sec, it is shown in part (d) of Figure 44 that, shortly after the motion starts, the work increases indicating

that the energy is extracted from the flow. Hence, the combined potential and kinetic energies continue to increase. Then the amplitude of the oscillations grows as shown in part (a) of Figure 44.

So whether the oscillation decays or grows depends on the balance between the negative and positive work done by the aerodynamic loads when the structural damping is absent.

The counterclockwise rotation in the state planes as shown in parts (a) of Figures 42, 43 and 44 illustrates that θ lags y by an angle ψ that is between 0° and 180°. According to Equation (5.1.2), this ψ makes the lift do positive work.

The motions of an NACA 0012 airfoil are shown in Figure 45: In part (a), $V_\infty = 80$ ft/sec; in part (b), $V_\infty = 85$ ft/sec; and in part (c), $V_\infty = 90$ ft/sec. When 80 ft/sec $\leq V_\infty < 90$ ft/sec, the motions are neither decaying nor diverging. The amplitudes of the motions vary with V_∞: the higher the velocity is, the larger the amplitude is. When $V_\infty = 90$ ft/sec, slight growth of the amplitudes is observed. When the freestream speed is above 90 ft/sec, the amplitudes grow rapidly as shown in part (a) of Figure 46 where $V_\infty = 95$ ft/sec. For the NACA 0012 airfoil, the critical speed is not defined as clearly as it is for the flat plate, but the behaviors of the NACA 0012 airfoil and the flat plate are quite similar, and for computational convenience in the discussion of flutter and flutter suppression only the flat-plate airfoil is used.

The oscillation of an NACA 0012 airfoil on nonlinear elastic supports is an example of how the present method can be applied. The elastic moment in Equation (4.3.5) takes the form $F_\theta^e = k_1^\theta(\theta + \beta\theta^3)$, and $V_\infty = 95$ ft/sec. The spring in the y-direction remains linear. The motions of the NACA 0012 airfoil are shown in Figure 46 in part (a) $\beta = 0$ (linear moment spring); in part (b) $\beta = 1$; and in part (c) $\beta = 5$. For the case of the linear spring, the motions are

divergent. For the cases of the nonlinear moment spring, the motions develop limit cycles. Limit cycles appear because, when θ is large, the cubic term in the moment causes the elastic support to harden (stiffen). The larger β is, the smaller the amplitudes of the bounded motion are. If $\beta < 0$, the cubic term softens the spring, and unbounded, instead of limit-cycle, motions develop.

The effect of the static angle of attack α is investigated next for the flat-plate airfoil. The initial condition is $y(0) = 0$, $\dot{y}(0) = 0$, $\theta(0) = -2°$, $\dot{\theta}(0) = 0$.

The motions for the case where $\alpha = 0°$ are shown in Figure 47. As shown in parts (a) and (b) of Figure 47, the motions decay when $V_\infty = 88$ ft/sec and 89 ft/sec. And as shown in parts (c) and (d), the motions grow when $V_\infty = 90$ ft/sec and 95 ft/sec. So the critical flutter speed is about 90 ft/sec, the same as the case shown in Figure 40 where the initial conditions are $y(0) = 0$, $\dot{y}(0) = 0$, $\theta(0) = -5°$, $\dot{\theta}(0) = 0$.

The motions for the case where $\alpha = 2°$ are shown in Figure 48. In parts (a), (b) and (c) of Figure 48, the velocity of freestream $V_\infty = 88$ ft/sec, 89 ft/sec, 90 ft/sec, respectively. The flutter speed is still about 90 ft/sec.

The motions for the case where $\alpha = 5°$ are shown in Figure 49. In parts (a), (b) and (c) of Figure 49, the velocity of freestream $V_\infty = 89$ ft/sec, 90 ft/sec, 91 ft/sec. The flutter speed is about 91 ft/sec.

The motions for the case where $\alpha = 8°$ are shown in Figure 50. In parts (a), (b) and (c) of Figure 50, the velocity of freestream $V_\infty = 90$ ft/sec, 90.3 ft/sec, 91 ft/sec. The flutter speed is still about 91 ft/sec.

From the cases shown in Figure 47 through Figure 50, the effect of increasing the static angle of attack α from 0° to 8° is very limited on the flutter speed: the larger α makes the the flutter speed just slightly higher. For the cases

concerned here, the flutter speed lies between 90 ft/sec and 91 ft/sec when $0° \leq \alpha \leq 8°$.

5.2 Suppression of Flutter

Next the system is extended by adding a flap to the trailing edge of flat-plate airfoil. Then control strategies for the flap that will lead to flutter suppression is considered. The length of the flap is 5.4% of the total chord and its deflection relative to the airfoil is δ. The equilibrium position for δ is labelled as $\delta_e = 0$ (see Figure 39).

When $\alpha = 0°$ and $V_\infty = 90$ft/sec, the motions diverge as shown in part (c) of Figure 40 and part (a) of Figure 44. To suppress this divergent oscillation, instantaneous feedback control defined by Equation (4.5.2) is applied, and the gains in Equation (4.5.1) are $a_1 = 102$, $a_2 = 102$, $a_3 = 2.4$, and $a_4 = 99$. The initial condition is $y(0) = 0$, $\dot{y}(0) = 0$, $\theta(0) = -5°$, $\dot{\theta}(0) = 0$. The cases where the bound on δ is $\delta_{max} = 15°$ and $20°$ are shown in parts (a) and (b) of Figure 51, respectively. When the maximum flap deflection is restricted to 15°, the flutter is not suppressed; however, when the maximum flap deflection is increased to 20°, then the flutter is eliminated. With $\delta_{max} = 20°$, y and θ are both converging to their equilibrium positions $y_e = -0.0091$ and $\theta_e = -0.95°$. The flap angle δ converges to $\delta_e = 0$.

The above problem can also be considered from the energy point of view. For the case where $\delta_{max} = 20°$, the plots of θ vs. y, the lift vs. y, the hinge moment (acting on the flap about the hinge) vs. flap angle δ, the total moment vs. θ and work vs. time are shown in Figure 52. As shown in part (a), the rotation in the state space is now in the clockwise direction instead of the counterclockwise direction as in the uncontrolled cases, and θ lags y an angle ψ that is between

180° and 360°. Therefore, the lift does negative work [as shown in part (b)] according Equation (5.1.2). As shown in part (c) of Figure 52, the total moment acting on the airfoil does positive work. This is different from the one without control shown in part (c) of Figure 44. The feedback control performed by the flap makes the flow around the airfoil different from the one without feedback control. Consequently the way in which the aerodynamic loads act on the airfoil is changed. As shown in part (d) of Figure 52, the hinge moment does negative work, and this means that the motion of the airfoil loses the energy to the flow. If the mass of the flap can be neglected, the hinge moment needed to operate the flap is the opposite of the hinge moment applied by the aerodynamic loads. Almost no work is done by the aerodynamic loads after the oscillations have nearly decayed as shown in part (e) of Figure 52.

In the following examples in this section, the initial disturbance is: $y(0) = 0$, $\dot{y}(0) = 0$, $\theta(0) = -2°$, $\dot{\theta}(0) = 0$.

Without any control, the oscillations diverge when $\alpha = 0°$ and $V_\infty \geq 90$ ft/sec as shown in parts (c) and (d) of Figure 47. When $V_\infty = 90$ ft/sec, and the gains defined in Equation (4.5.1) are $a_1 = 114$, $a_2 = 172$, $a_3 = 0$, $a_4 = 0$, and $\delta_{max} = 5°$, the suppressed oscillations are shown in parts (a), (b) and (c) of Figure 53. With this kind of control, only the motion in y is used as the feedback instead of the motions in both y and θ as in the previous case of control. With Equation (4.5.2), the instantaneous control is used as shown in part (a) of Figure 53: y and θ reach their equilibrium positions $y_e = -0.0091$ and $\theta_e = -0.95°$ very fast. With Equation (4.5.3), two cases of delayed control are shown in parts (b) and (c) of Figure 53: in part (b) the coefficients in Equation (4.5.3) are $c_1 = 4$, $c_2 = 40$; in part (c) $c_1 = 4$, $c_2 = 10$. The larger c_2 is, the sooner δ reaches the command angle δ_c and the faster the oscillation is suppressed. When $a_1 = 0$, $a_2 = 172$, $a_3 = 0$, $a_4 = 0$ (i.e. only $\dot{y}$ is used as the feedback), results for instantaneous control are shown in part (d) of Figure 53. Comparing part (d)

with part (a), one can see that, y is suppressed faster and θ is suppressed more slowly by using only $\dot{y}$ as the feedback than by using both y and $\dot{y}$.

It is interesting to look at the wakes for the cases without and with the control. Corresponding to part (c) of Figure 47, the wake at time t = 200 is shown in part (a) of Figure 54. The vortex sheet behind the airfoil stretches and rolls up forming regions of concentrated-vorticity, which are not very obvious, but shown enlarged in the insert, because the amplitude of the oscillation is still small at time t = 200. Corresponding to part (a) of Figure 53, the wake at time t = 25 is shown in part (b) of Figure 54. The vortex sheet only stretched without rolling up because the motions have been mostly suppressed at time t = 25 as shown in part (a) of Figure 53.

Corresponding to the case shown in part (d) of Figure 47, where $\alpha = 0°$, $V_\infty = 95$ ft/sec, $y_e = -0.0086$ and $\theta_e = -0.99°$, the oscillations suppressed by the instantaneous feedback control with $\delta_{max} = 5°$ are shown in Figure 55. In part (a) the gains are $a_1 = 114$, $a_2 = 172$, $a_3 = a_4 = 0$; in part (b) the gains are $a_1 = 0$, $a_2 = 172$, $a_3 = a_4 = 0$. Again, y is suppressed faster and θ is suppressed slower by using only $\dot{y}$ as the feedback than by using both y and $\dot{y}$.

Corresponding to the case shown in part (c) of Figure 48, where $\alpha = 2°$, $V_\infty = 90$ ft/sec, $y_e = 0.00018$ and $\theta_e = -1.68°$, the oscillations suppressed by the instantaneous feedback control with $\delta_{max} = 5°$ are shown in Figure 56. In part (a) the gains are $a_1 = 114$, $a_2 = 172$, $a_3 = a_4 = 0$; in part (b) the gains are $a_1 = 0$, $a_2 = 172$, $a_3 = a_4 = 0$.

Corresponding the case shown in part (c) of Figure 49, where $\alpha = 5°$, $V_\infty = 91$ ft/sec, $y_e = 0.0015$ and $\theta_e = -2.79°$, the oscillations suppressed by the instantaneous feedback control are shown in Figure 57. In part (a) the gains are $a_1 = 114$, $a_2 = 172$, $a_3 = a_4 = 0$, and $\delta_{max} = 5°$; in part (b) the gains are

$a_1 = 0$, $a_2 = 172$, $a_3 = a_4 = 0$, and $\delta_{max} = 10°$ (using $\delta_{max} = 5°$ failed to suppress the divergent oscillations).

Corresponding to the case shown in part (c) of Figure 50, where $\alpha = 8°$, $V_\infty = 91$ ft/sec, $y_e = 0.0028$ and $\theta_e = -3.83°$, the oscillations suppressed by the instantaneous feedback control are shown in Figure 58. In part (a) the gains are $a_1 = 114$, $a_2 = 172$, $a_3 = a_4 = 0$, and $\delta_{max} = 5°$; in part (b) the gains are $a_1 = 0$, $a_2 = 172$, $a_3 = a_4 = 0$, and $\delta_{max} = 10°$ (again using $\delta_{max} = 5°$ failed to suppress the divergent oscillations).

With the two groups of gains used in the cases shown in Figures 55 through 58, the divergent oscillations can be successfully suppressed for $0° \leq \alpha \leq 8°$. y is suppressed faster and θ is suppressed slower by using only $\dot{y}$ as the feedback than using both y and $\dot{y}$. And using only $\dot{y}$ needs larger δ_{max} than using both y and $\dot{y}$ when α is larger.

Attempts at using only the motion in θ as the feedback (i.e., $a_1 = a_2 = 0$, but a_3 and $a_4 \neq 0$) failed.

5.3 Suppression of the Response to a Wind Gust by Feedback Control

Now the response to a wind gust is studied, and the dimensionless velocity of the freestream is given as the following

$$\frac{\vec{V}_\infty}{V_\infty} = \begin{cases} \vec{i} + (v_d \sin \omega_d t)\vec{j} & \text{for } 0 \leq t \leq \dfrac{2\pi}{\omega_d} \\ \vec{i} & \text{for } t < 0 \text{ and } t > \dfrac{2\pi}{\omega_d} \end{cases} \tag{5.3.1}$$

where $v_d = 0.1$ and $\omega_d = 0.4\pi$. The freestream is disturbed in the vertical direction.

In the examples of this section, the initial conditions are the equilibrium positions of the airfoil in the undisturbed freestream, and $\delta_{max} = 5°$.

When $\alpha = 0°$ and $V_\infty = 85$ ft/sec, the equilibrium position is $y_e = -0.0096$ and $\theta_e = -0.92°$ in the undisturbed flow. The responses to the wind gust without any attempt at suppression are shown in part (a) Figure 59. The oscillations decay gradually because $V_\infty = 85$ ft/sec is below the flutter speed and the equilibrium position is stable. To make the motions die out more rapidly, feedback control is applied to the flap. Both instantaneous and delayed controls are used. For the delayed control, $c_1 = 4$ and $c_2 = 10$ are used in the servo equation (4.5.3). Two sets of gains are used. First, $a_1 = 114$, $a_2 = 172$, $a_3 = 0$, $a_4 = 0$, and the suppressed oscillations are shown in part (b) (using instantaneous control) and part (c) (using delayed control). Second, $a_1 = 0$, $a_2 = 172$, $a_3 = 0$, $a_4 = 0$, and the suppressed oscillations are shown in part (d) (using instantaneous control) part (c) (using delayed control). The motions die out much faster than those without the feedback control, and the instantaneous control is more effective than delayed control. Similar to the results of Section 5.2, y is suppressed faster and θ is suppressed more slowly by using only $\dot{y}$ as the feedback than by using both y and $\dot{y}$.

When $\alpha = 0°$ and $V_\infty = 90$ ft/sec, the equilibrium position is $y_e = -0.0091$ and $\theta_e = -0.95°$ in the undisturbed flow. The responses to the wind gust without any attempt at suppression are shown in part (a) Figure 60. The motions grow because $V_\infty = 90$ ft/sec is the flutter speed and the equilibrium position is unstable. The instantaneous control is used. Two sets of gains are used. First, $a_1 = 114$, $a_2 = 172$, $a_3 = 0$, $a_4 = 0$, and the suppressed oscillations are shown in part (b) Figure 60. Second, $a_1 = 0$, $a_2 = 172$, $a_3 = 0$, $a_4 = 0$, and the

suppressed oscillations are shown in part (c) Figure 60. The divergent response to the wind gust is suppressed by the feedback control.

When $\alpha = 5°$ and $V_\infty = 91$ ft/sec, the equilibrium position is $y_e = 0.015$ and $\theta_e = -2.79°$ in the undisturbed flow. The responses to the wind gust without any attempt at suppression are shown in part (a) Figure 61. The motions grow because $V_\infty = 91$ ft/sec is the flutter speed and the equilibrium position is unstable. For this case, instantaneous control is used. Two sets of gains are chosen. First, $a_1 = 114$, $a_2 = 172$, $a_3 = 0$, $a_4 = 0$, and the suppressed oscillations are shown in part (b) Figure 61. Second, $a_1 = 0$, $a_2 = 172$, $a_3 = 0$, $a_4 = 0$, and the suppressed oscillations are shown in part (c) Figure 61. Again the divergent response to the wind gust is suppressed by the feedback control.

Both the decaying and growing responses to the prescribed wind gust can be suppressed by the same feedback control as the one used to suppress the flutter motion.

5.4 Summary

For the linear spring, the critical flutter speed obtained here is close to the result of Fung (1969). Nonlinear, hardening springs can greatly reduce the amplitude of the flutter motions, but have practically no influence on the critical flutter speed.

Whether flutter happens or not depends on the net work done by the lift force and moment. Motion decays when the net work is negative, and motion grows when the net work is positive. In the cases studied, lift does positive work and moment does negative work when no control device (a flap at the trailing edge) is used. When a flap is added and the motion is suppressed, lift does negative work and moment does positive work.

Feedback control successfully suppressed the flutter motion and the response to a wind gust. Using the motion in y as the feedback variable appears to be more effective than using the motion in θ. The bound flap angle δ_{max} needed for effective flutter suppression depends on the variables used in control laws.

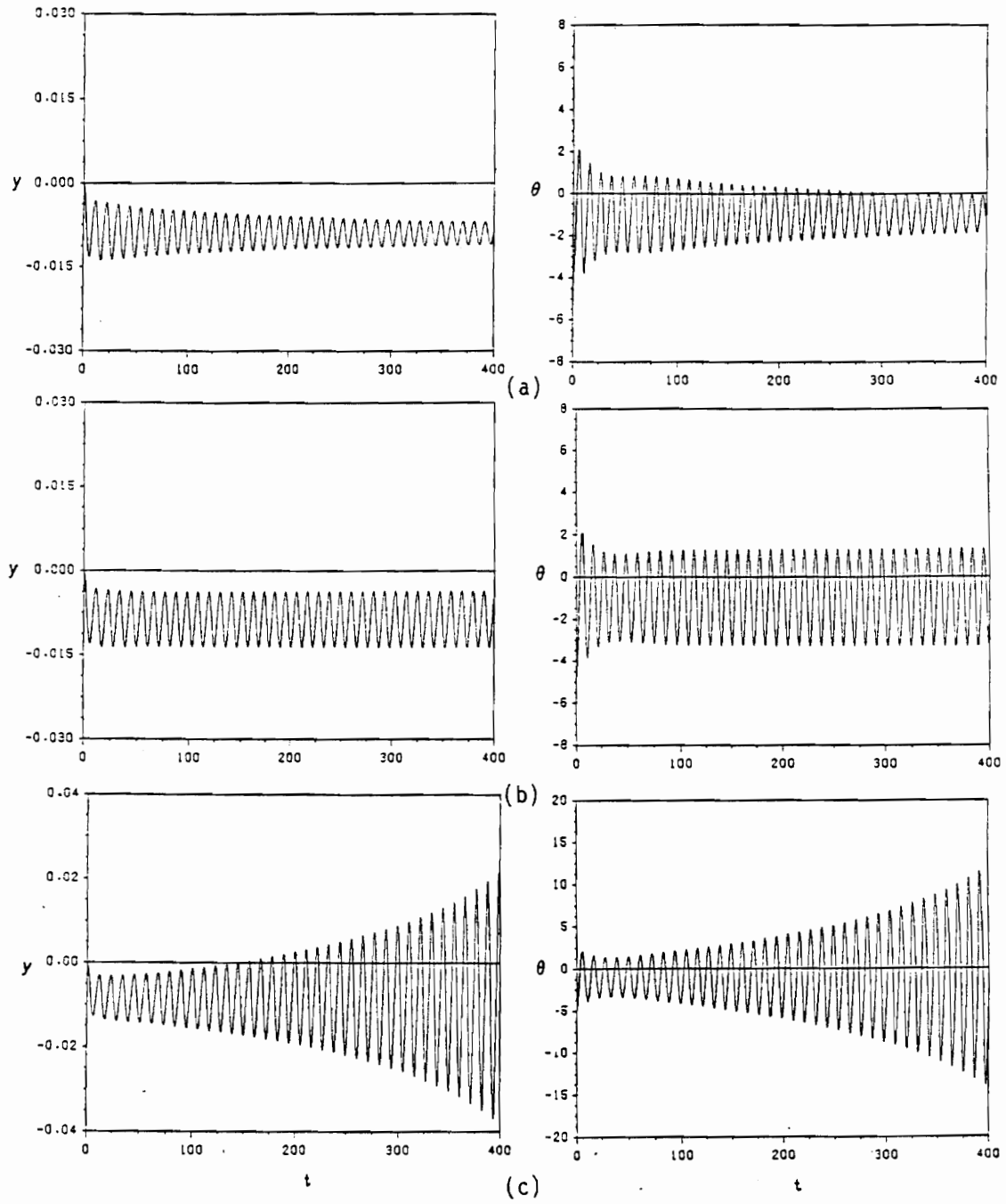

Figure 40. Motion of the flat airfoil: $\alpha = 0$, and the initial conditions are $y(0) = 0$, $\dot{y}(0) = 0$, $\theta(0) = -5°$ and $\dot{\theta}(0) = 0$. (a) $V_\infty = 88$ ft/sec; (b) $V_\infty = 89$ ft/sec; (c) $V_\infty = 90$ ft/sec.

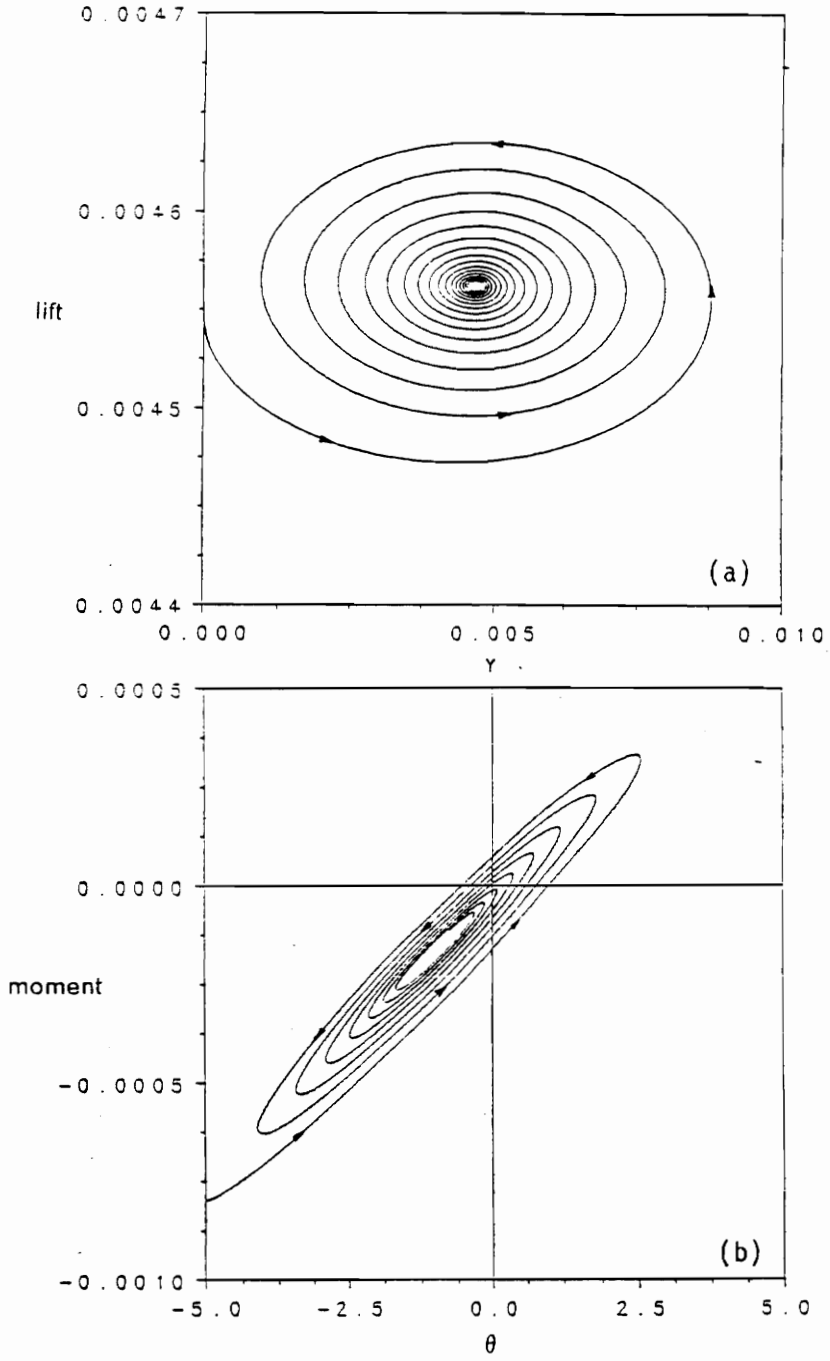

Figure 41. Motions of one-degree-of-freedom systems: $V_\infty = 90$ ft/sec, (a) only motion in plunge (y direction) is allowed; (b) only motion in pitch (θ direction) is allowed.

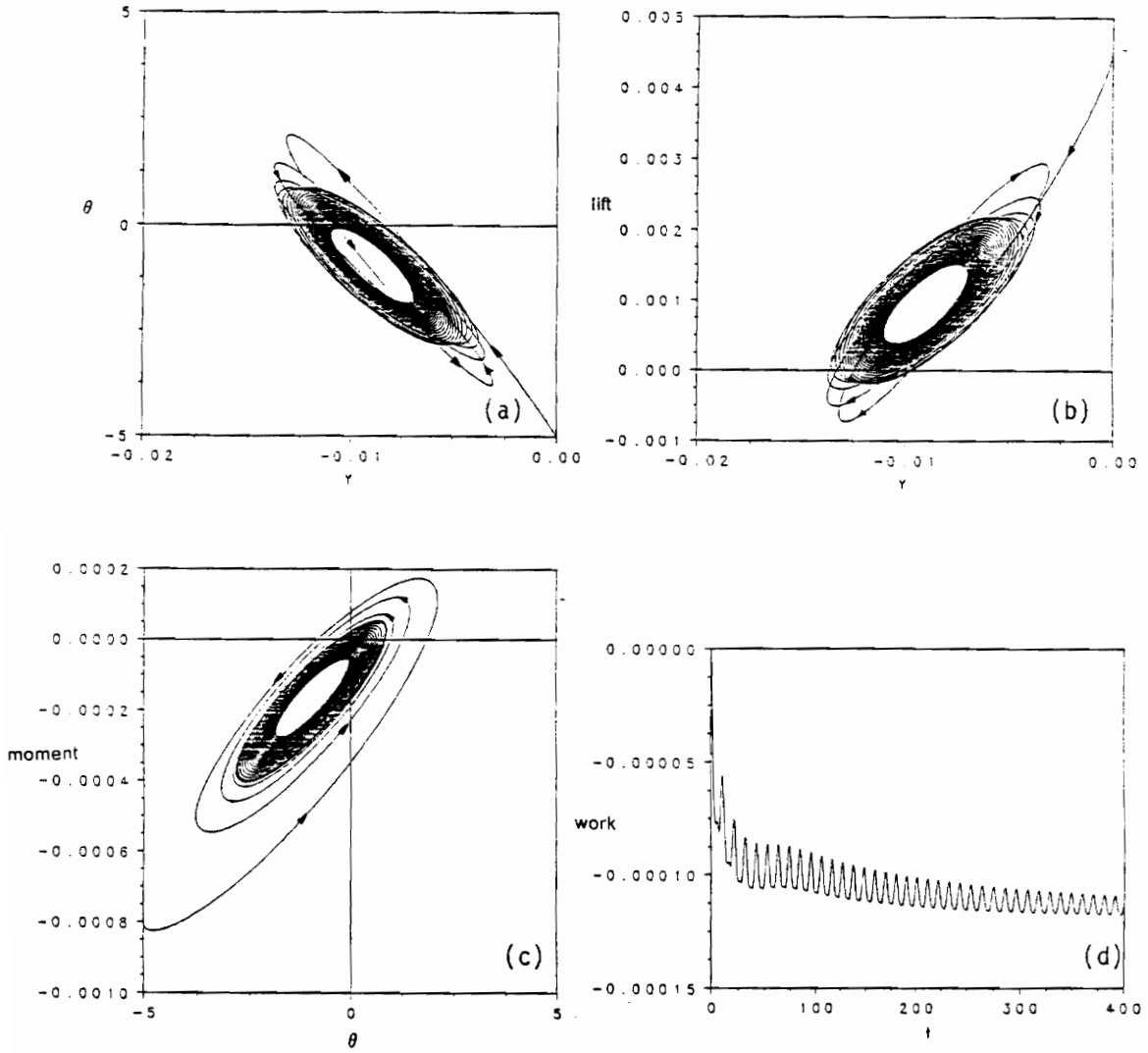

Figure 42. **State plane, lift, total moment, hinge moment and net work for the same case as in part (a) of Figure 40:** $V_\infty = 88$ ft/sec, (a) y vs. θ, the direction of the curve is counterclockwise; (b) the lift vs. y, the direction of the curve is clockwise and the work is positive; (c) the moment vs. θ, the direction of the curve is counterclockwise and the work is negative; (d) the net work vs. the time.

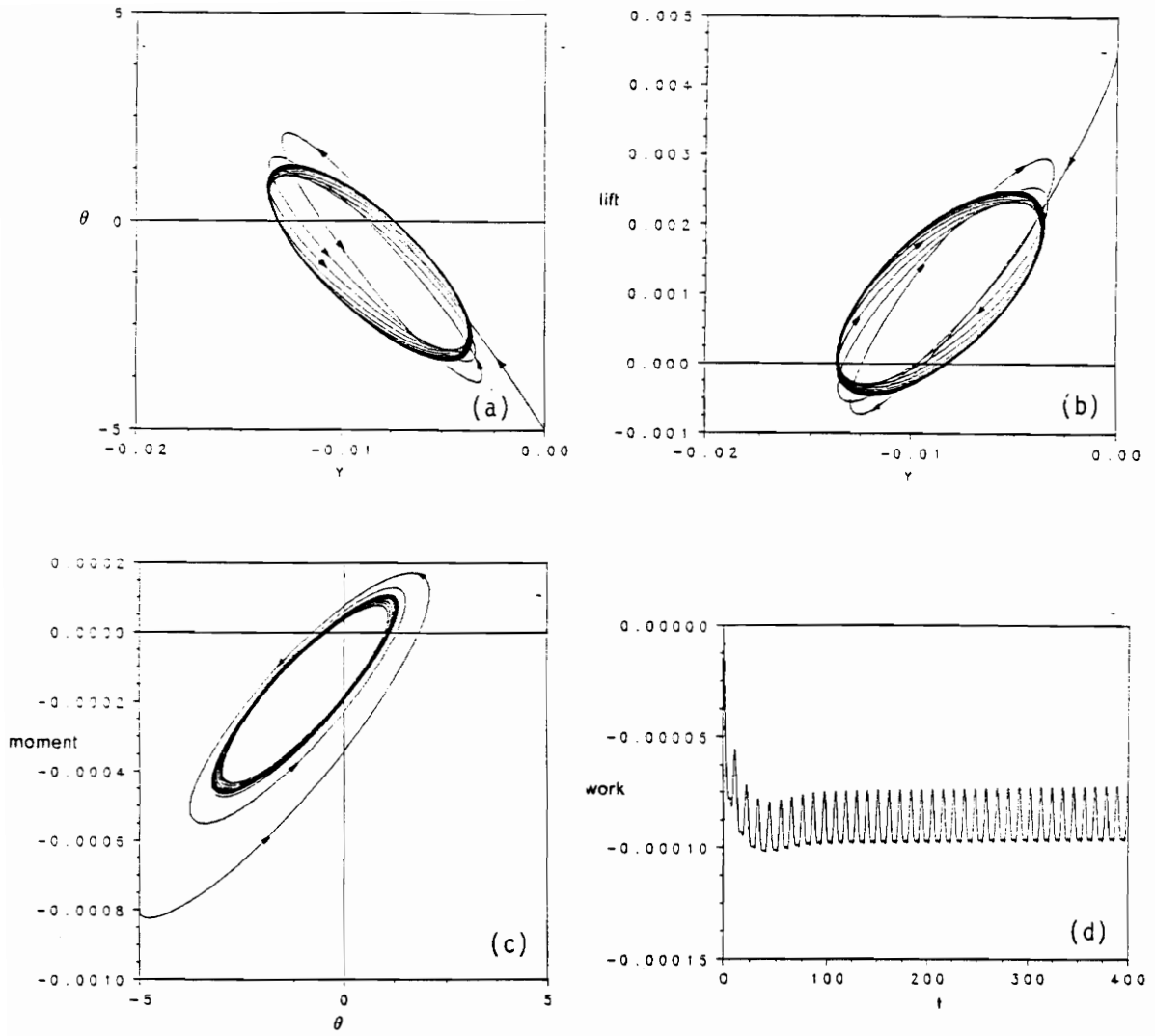

Figure 43. State plane, lift, total moment, hinge moment and net work for the same case as in part (b) of Figure 40: $V_\infty = 89$ ft/sec, (a) y vs. θ, the direction of the curve is counterclockwise; (b) the lift vs. y, the direction of the curve is clockwise and the work is positive; (c) the moment vs. θ, the direction of the curve is counterclockwise and the work is negative; (d) the net work vs. the time.

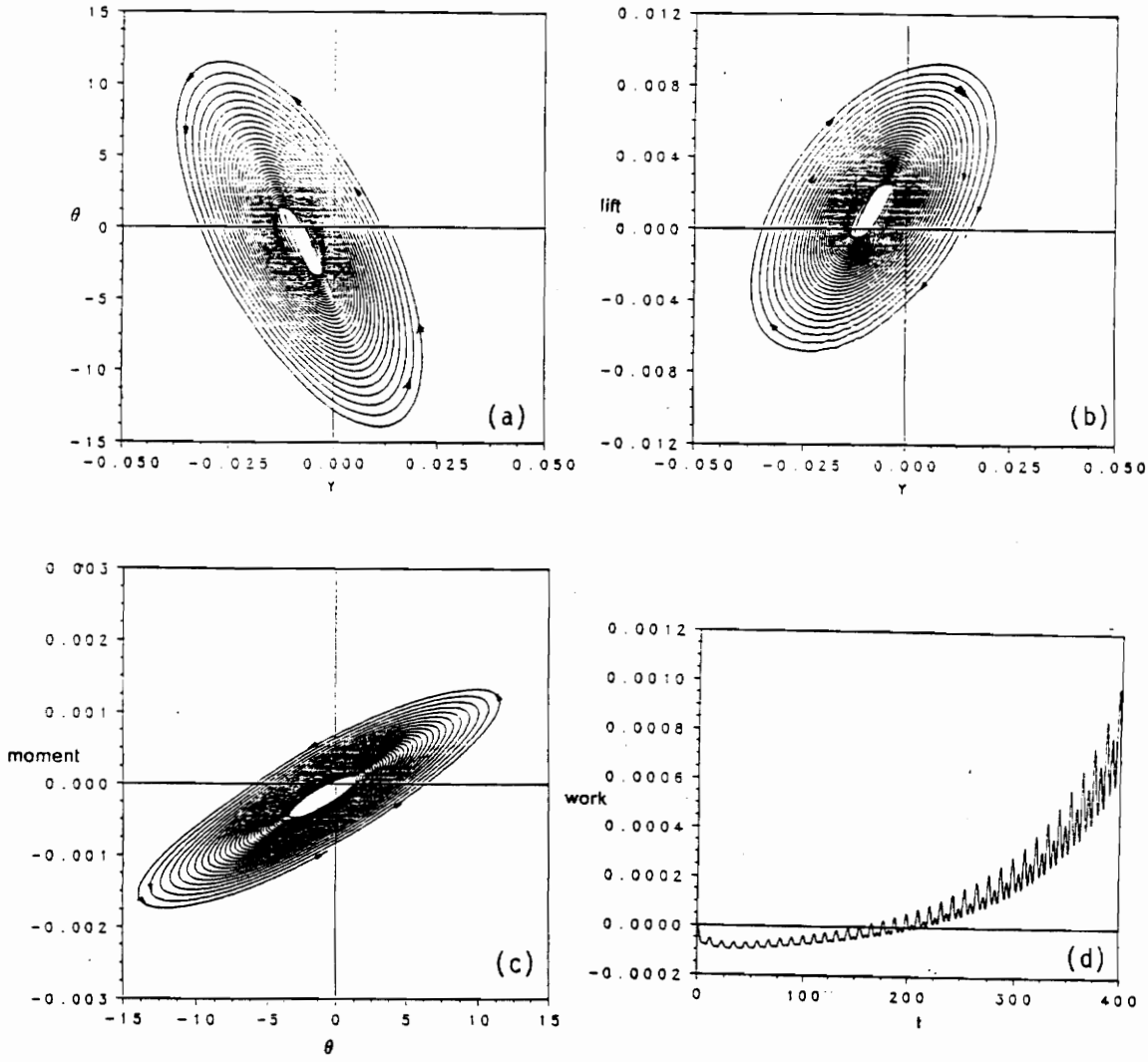

Figure 44. **State plane, lift, total moment, hinge moment and net work for the same case as in part (c) of Figure 40:** $V_\infty = 90$ ft/sec, (a) y vs. θ, the direction of the curve is counterclockwise; (b) the lift vs. y, the direction of the curve is clockwise and the work is positive; (c) the moment vs. θ, the direction of the curve is counterclockwise and the work is negative; (d) the net work vs. the time.

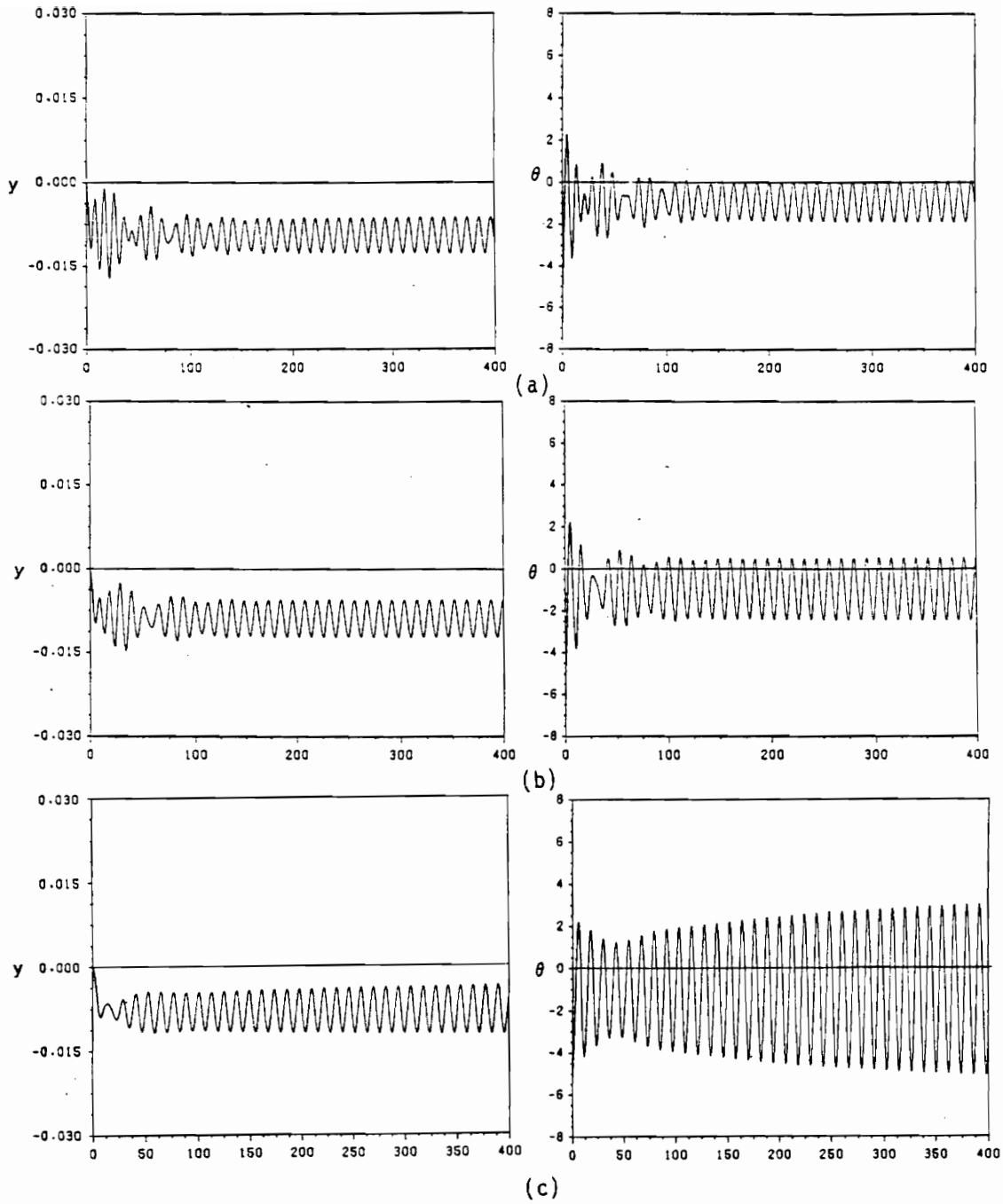

Figure 45. Motion of an NACA 0012 airfoil: (a) $V_\infty = 80$ ft/sec; (b) $V_\infty = 85$ ft/sec; (c) $V_\infty = 90$ ft/sec.

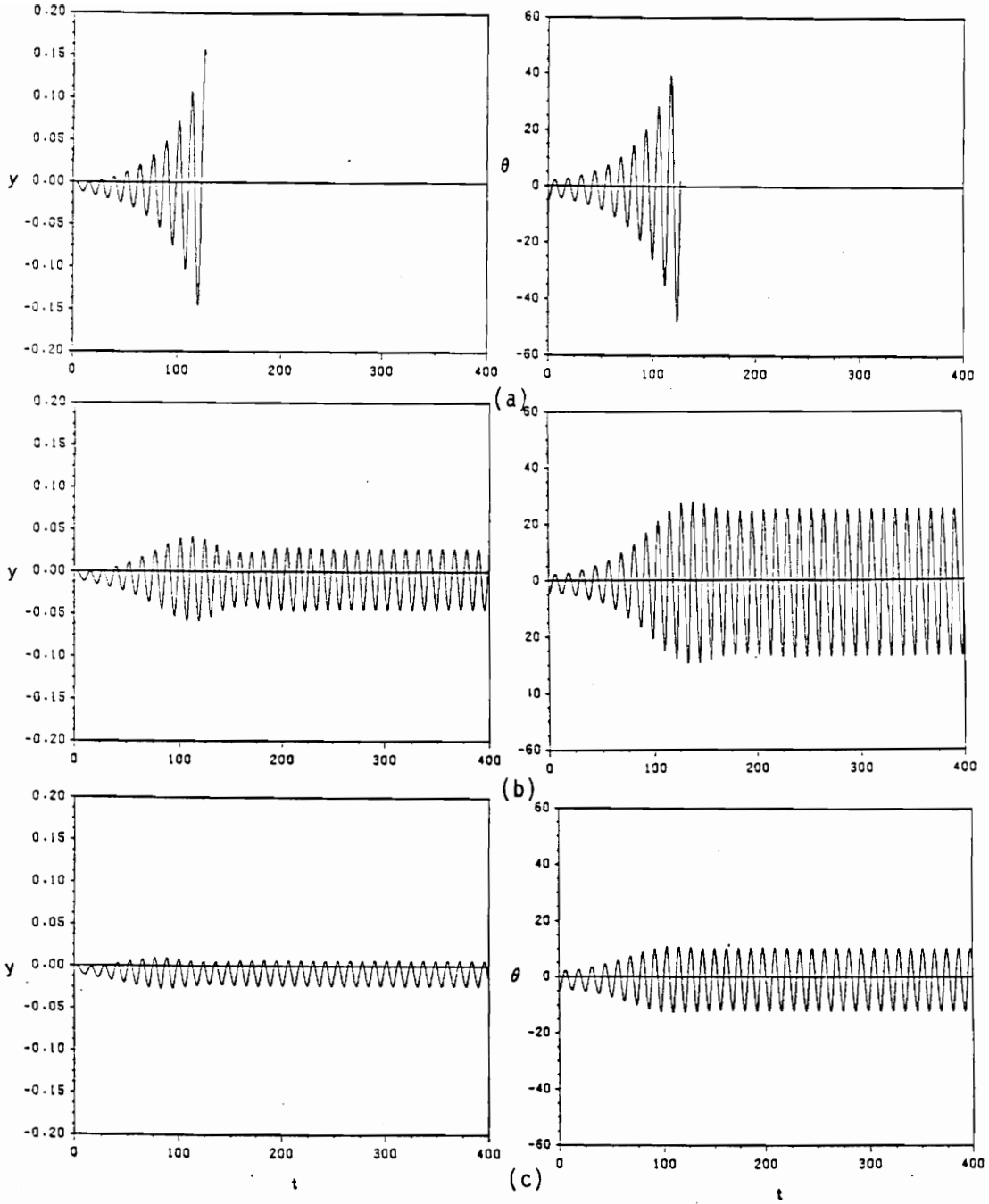

Figure 46. **Motions of an NACA 0012 airfoil mounted on a nonlinear elastic support:** $F_\theta^e = k_\theta^e(\theta + \beta\theta^3)$ and $V_\infty = 95$ ft/sec. (a) $\beta = 0$; (b) $\beta = 1$; (c) $\beta = 5$.

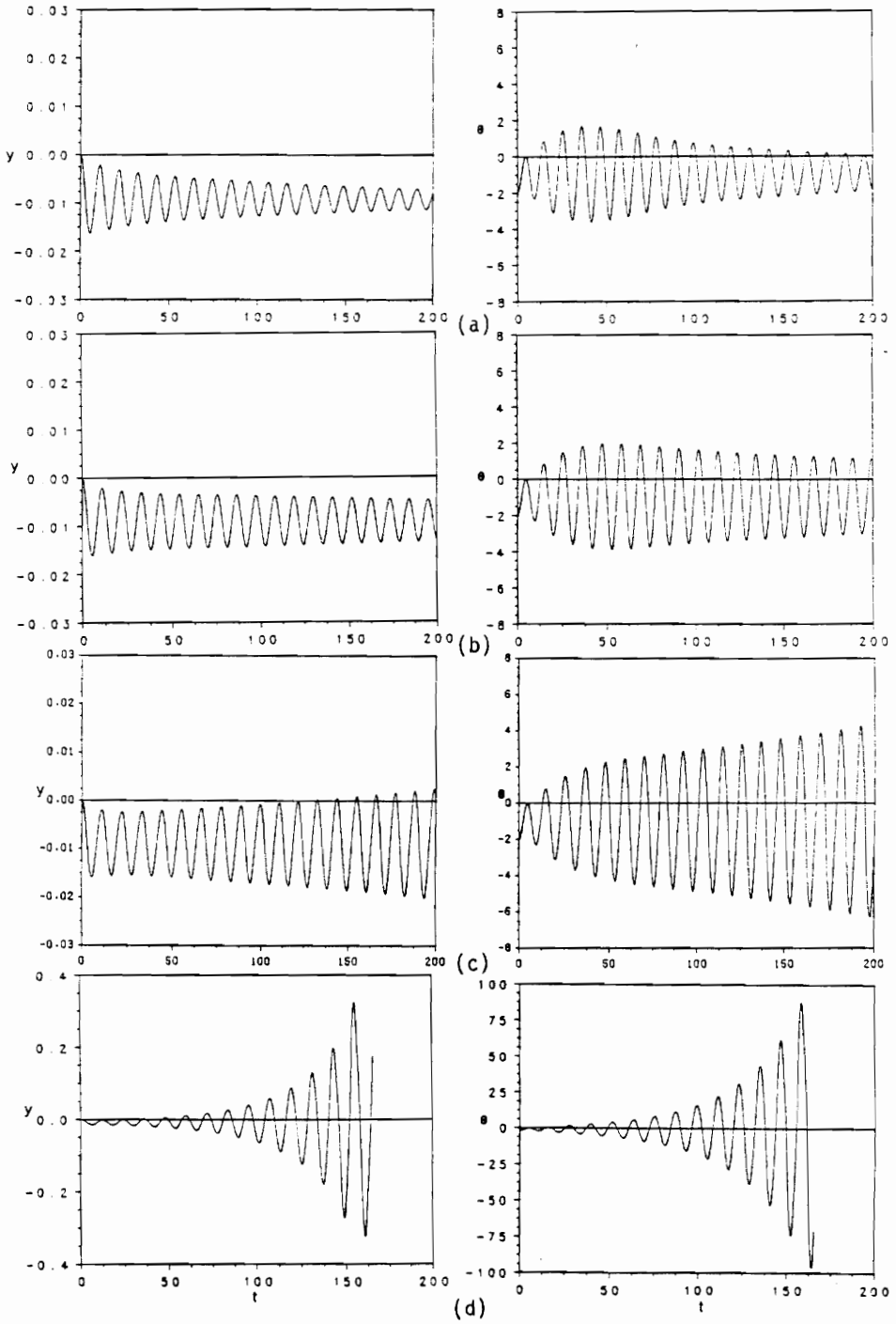

Figure 47. Motion of the flat airfoil when $\alpha = 0°$: the initial conditions are $y(0) = 0$, $\dot{y}(0) = 0$, $\theta(0) = -2°$ and $\dot{\theta}(0) = 0$. (a) $V_\infty = 88$ ft/sec; (b) $V_\infty = 89$ ft/sec; (c) $V_\infty = 90$ ft/sec; (d) $V_\infty = 95$ ft/sec.

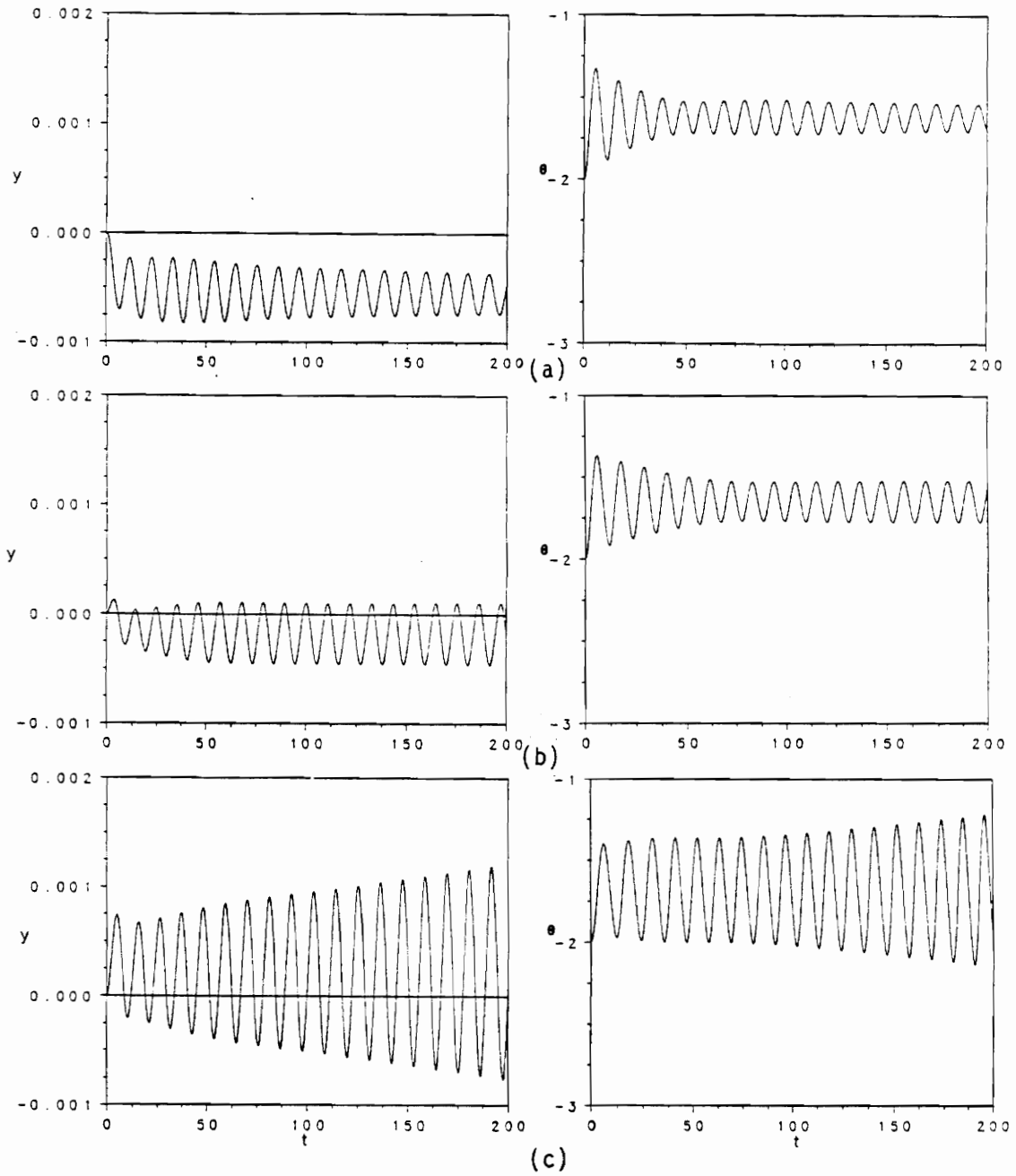

Figure 48. Motion of the flat airfoil when $\alpha = 2°$: the initial conditions are $y(0) = 0$, $\dot{y}(0) = 0$, $\theta(0) = -2°$ and $\dot{\theta}(0) = 0$. (a) $V_\infty = 88$ ft/sec; (b) $V_\infty = 89$ ft/sec; (c) $V_\infty = 90$ ft/sec.

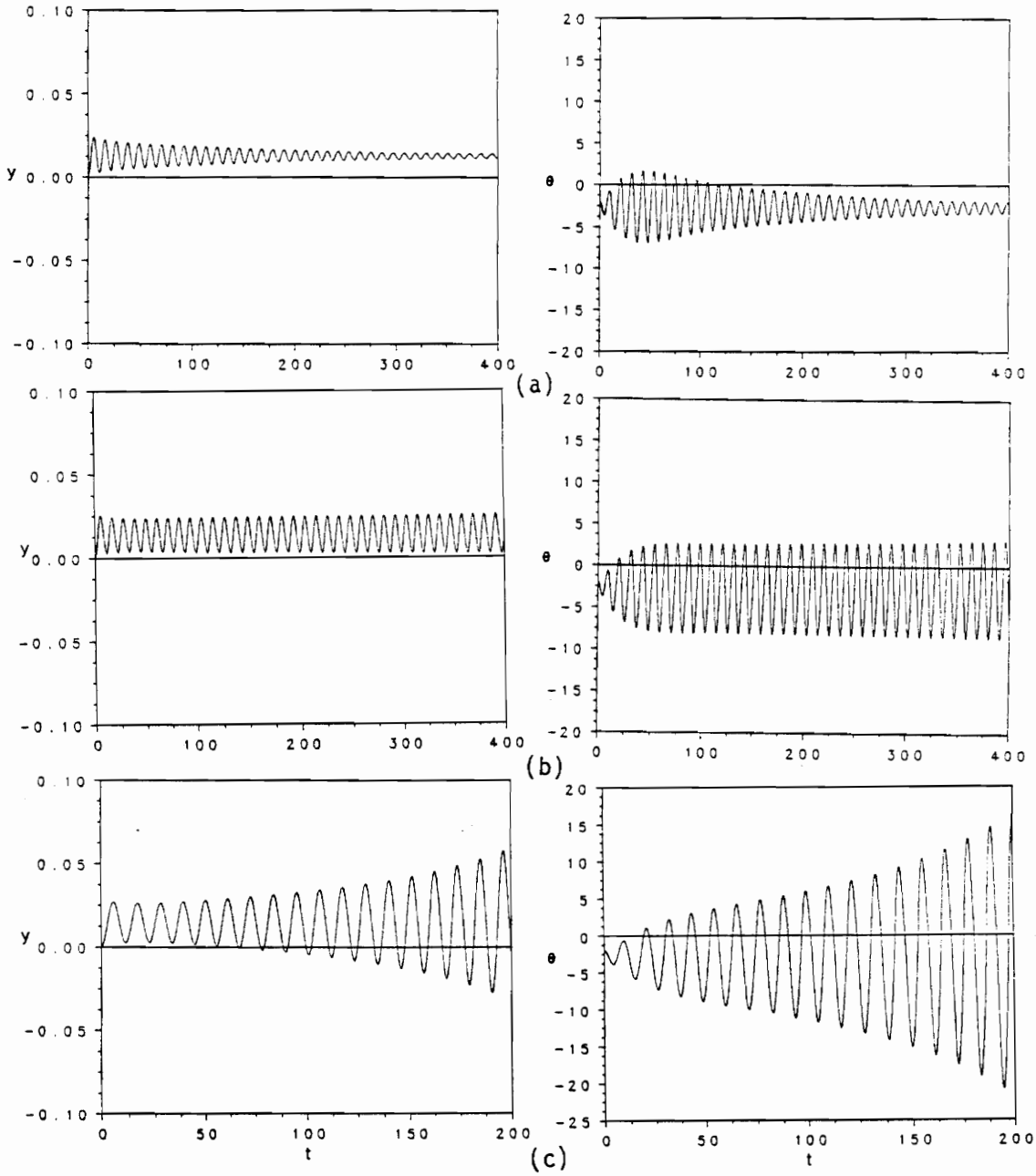

Figure 49. Motion of the flat airfoil when $\alpha = 5°$: the initial conditions are $y(0) = 0$, $\dot{y}(0) = 0$, $\theta(0) = -2°$ and $\dot{\theta}(0) = 0$. (a) $V_\infty = 89$ ft/sec; (b) $V_\infty = 90$ ft/sec; (c) $V_\infty = 91$ ft/sec.

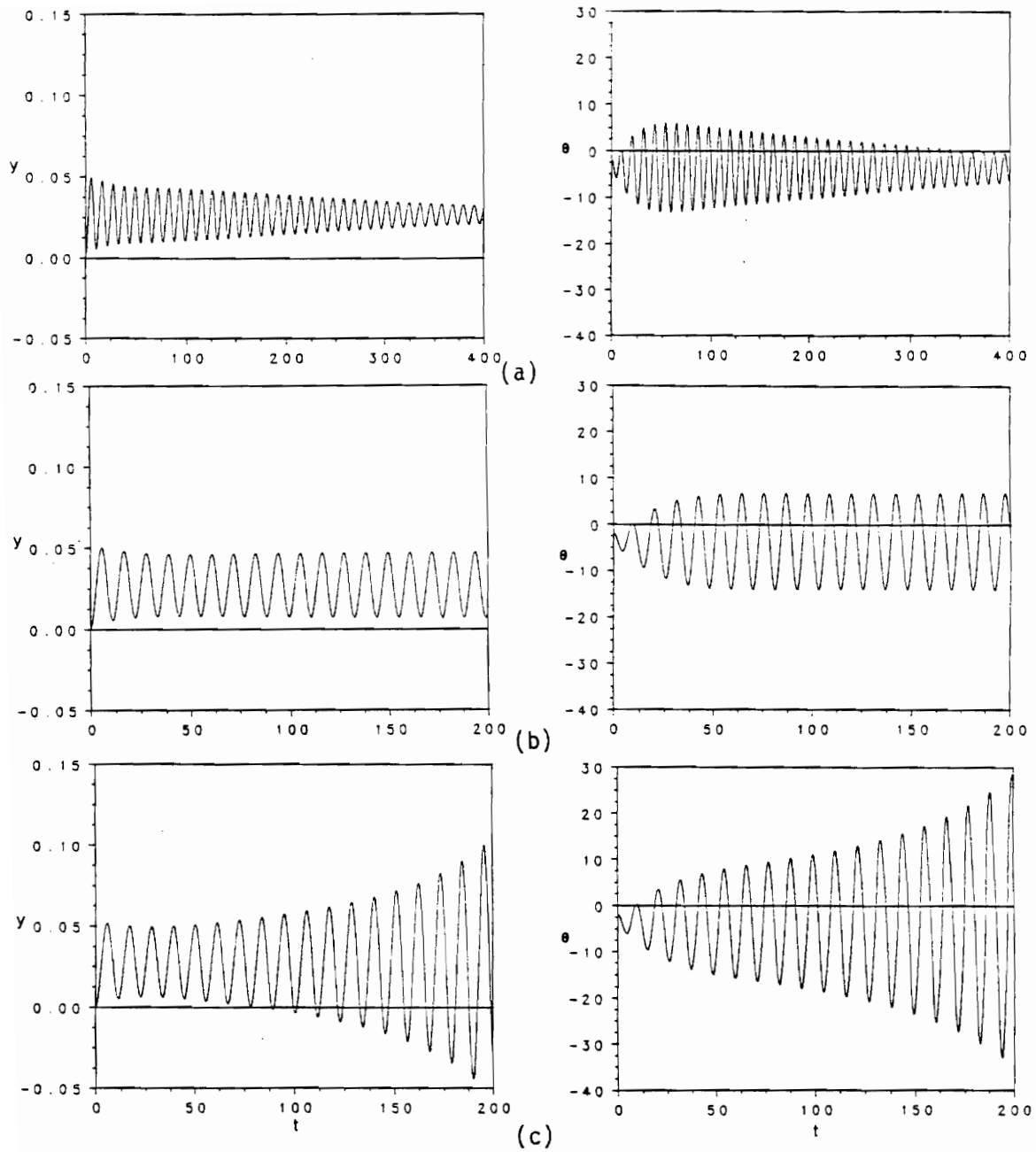

Figure 50. **Motion of the flat airfoil when $\alpha = 8°$:** the initial conditions are $y(0) = 0$, $\dot{y}(0) = 0$, $\theta(0) = -2°$ and $\dot{\theta}(0) = 0$. (a) $V_\infty = 90$ ft/sec; (b) $V_\infty = 90.3$ ft/sec; (c) $V_\infty = 91$ ft/sec.

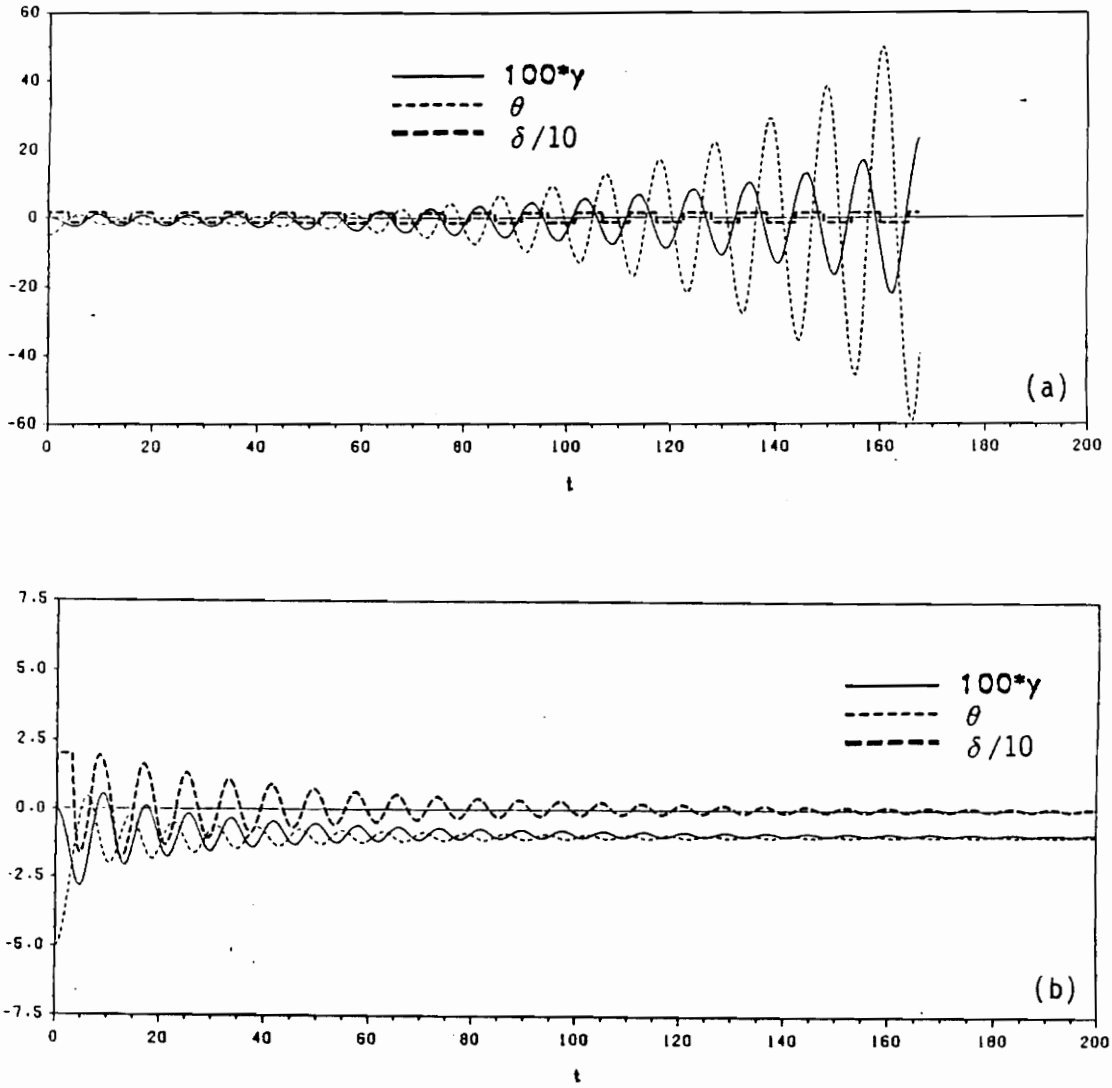

Figure 51. **Flutter suppression by instantaneous control:** $\delta = 102(y - y_e) + 101\dot{y} + 2.4(\theta - \theta_e) + 99\theta$, $V_\infty = 90$ ft/sec and the initial condition is $y(0) = \dot{y}(0) = \theta(0) = 0$, $\dot{\theta}(0) = -5°$. (a) $\delta_{max} = 15°$; (b) $\delta_{max} = 20°$.

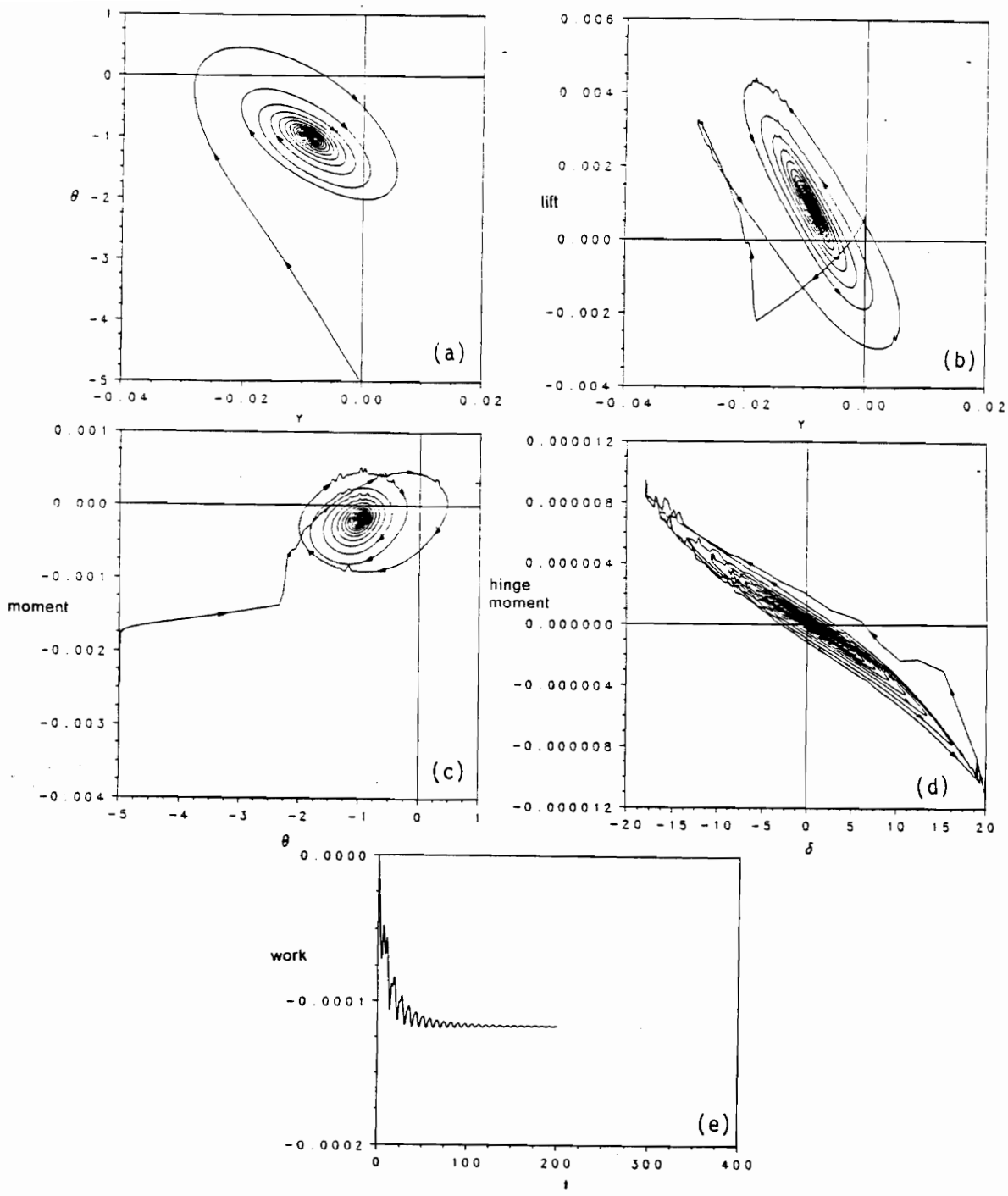

Figure 52. State plane, lift, total moment, hinge moment and net work for the same case as in part (b) of Figure 51: (a) y vs. θ, the direction of the curve is clockwise; (b) the lift vs. y, the direction of the curve is counterclockwise and the work is negative; (c) the total moment vs. θ, the direction of the curve is clockwise and the work is positive; (d) the moment acting on the flap about the hinge point vs. δ, the direction of the curve is counterclockwise and the work is negative; (e) the net work vs. the time.

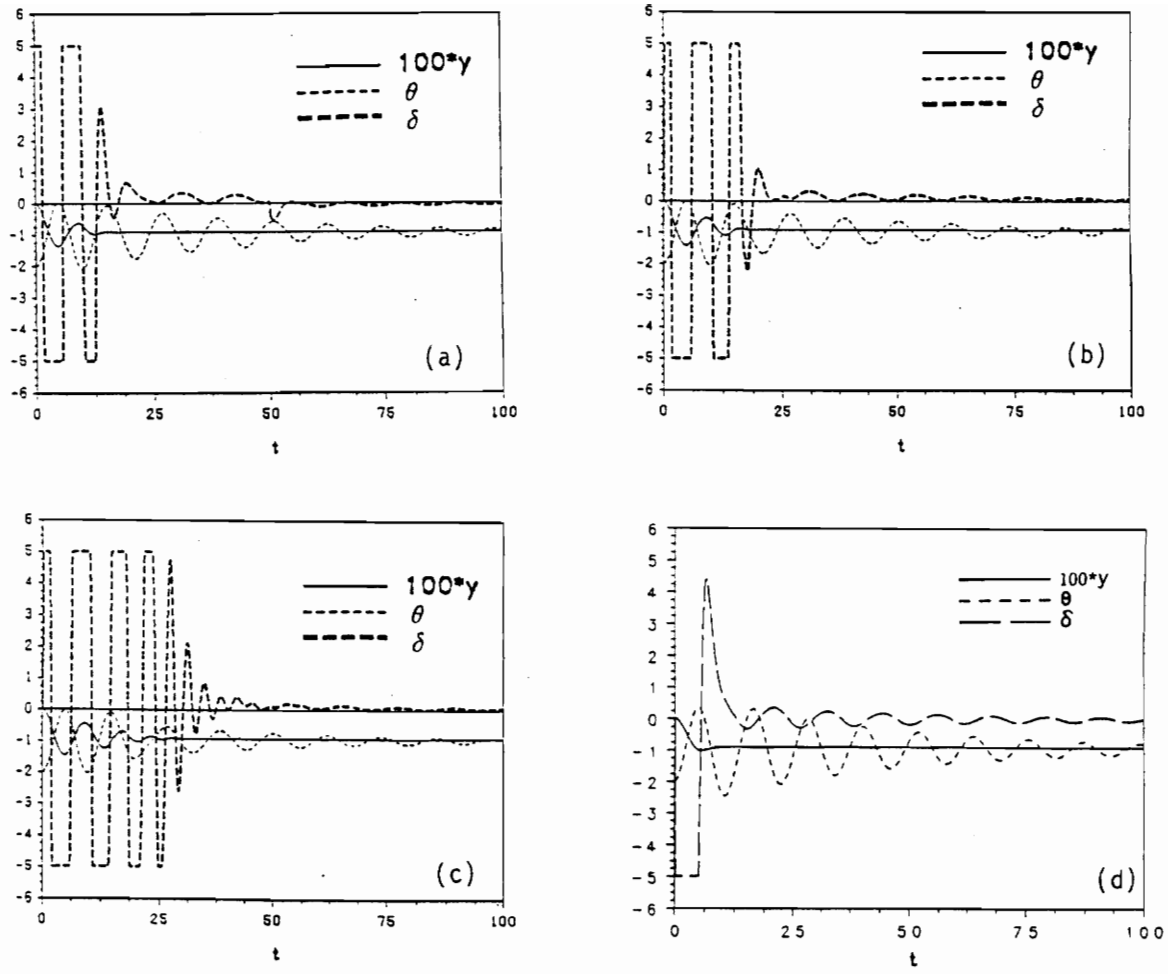

Figure 53. Suppressed motions of a flat airfoil by feedback control: $V_\infty = 90$ ft/sec and the initial condition is $y(0) = \dot{y}(0) = \theta(0) = 0$, $\dot{\theta}(0) = -2°$. For the delayed control δ satisfies $\ddot{\delta} + c_1\dot{\delta} + c_2(\delta - \delta_c) = 0$ where $\delta_c = 114(y - y_e) + 172\dot{y}$ and $\delta_{max} = 5°$. (a) the instantaneous control $\delta = \delta_c$; (b) the delayed control with $c_1 = 4$ and $c_2 = 40$; (c) the delayed control with $c_1 = 4$ and $c_2 = 10$; (d) the instantaneous control $\delta = 172\dot{y}$.

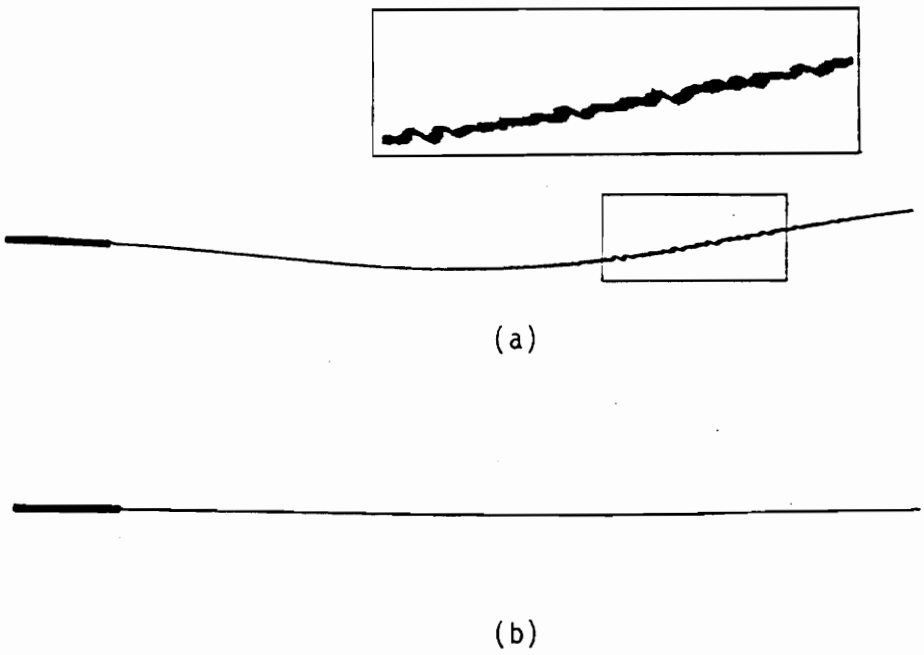

Figure 54. Wakes behind a flat airfoil with/without feedback control: $V_\infty = 90$ ft/sec. (a) Without control, corresponding to part (c) of Figure 47 at t=200, in the frame is a close look; (b) with control, corresponding to part (a) of Figure 53 at t = 25 .

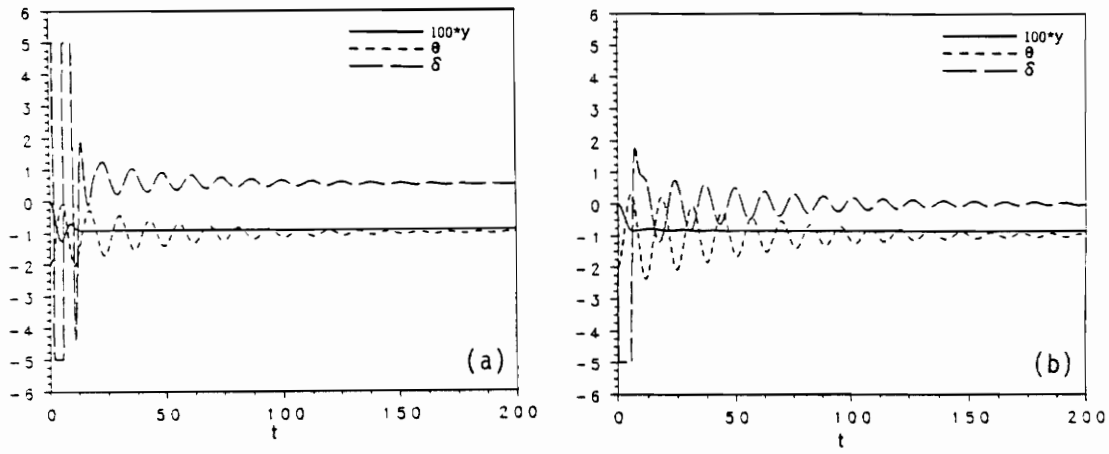

Figure 55. **Suppressed motions by the instantaneous feedback control corresponding to the case in part (d) of Figure 47:** $\alpha = 0°$, $V_\infty = 95$ ft/sec, and $\delta_{max} = 5°$. (a) $\delta = 114(y - y_e) + 172\dot{y}$; (b) $\delta = 172\dot{y}$.

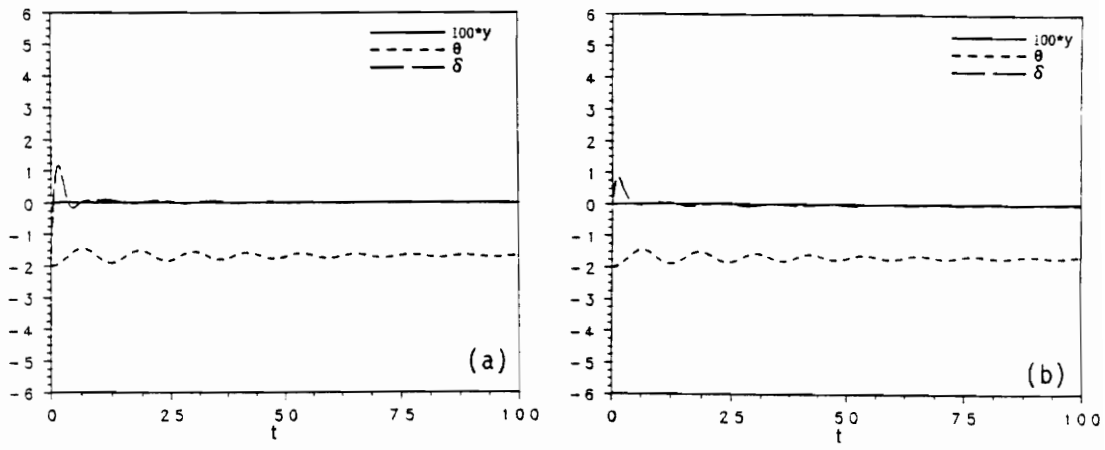

Figure 56. **Suppressed motions by the instantaneous feedback control corresponding to the case in part (c) of Figure 48:** $\alpha = 2°$, $V_\infty = 90$ ft/sec, and $\delta_{max} = 5°$. (a) $\delta = 114(y - y_e) + 172\dot{y}$; (b) $\delta = 172\dot{y}$.

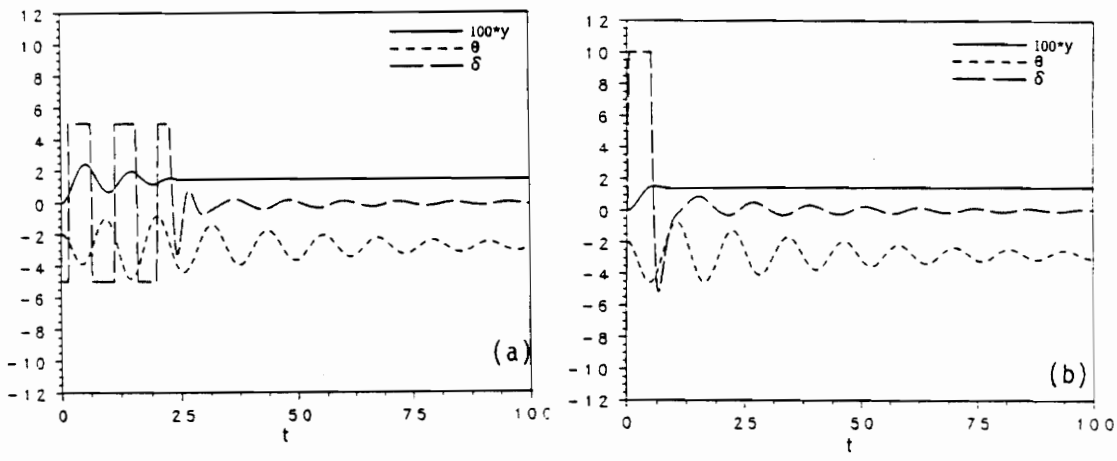

Figure 57. **Suppressed motions by the instantaneous feedback control corresponding to the case in part (c) of Figure 49:** $\alpha = 5°$ and $V_\infty = 91$ ft/sec. (a) $\delta_{max} = 5°$, $\delta = 114(y - y_e) + 172\dot{y}$; (b) $\delta_{max} = 10°$, $\delta = 172\dot{y}$.

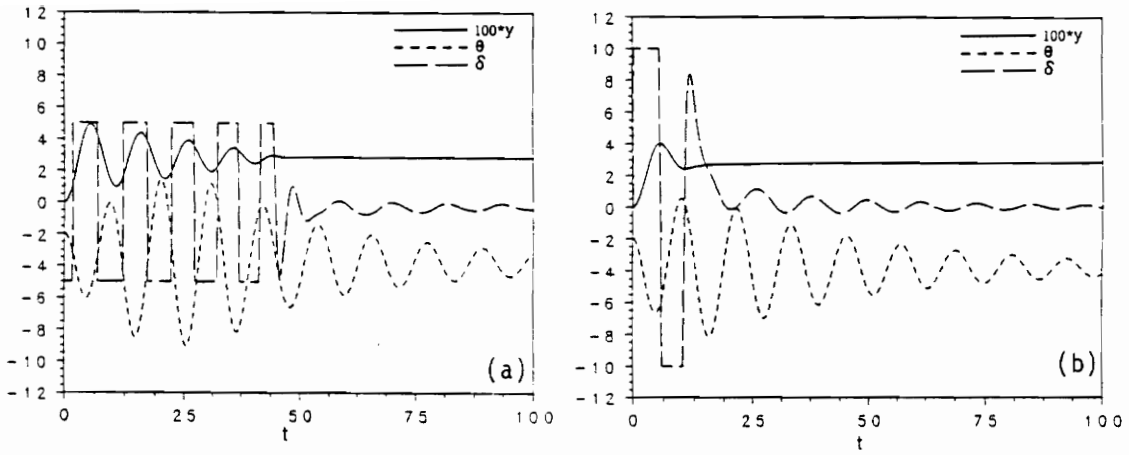

Figure 58. Suppressed motions by the instantaneous feedback control corresponding to the case in part (c) of Figure 50: $\alpha = 8°$ and $V_\infty = 91$ ft/sec. (a) $\delta_{max} = 5°$, $\delta = 114(y - y_e) + 172\dot{y}$; (b) $\delta_{max} = 10°$, $\delta = 172\dot{y}$.

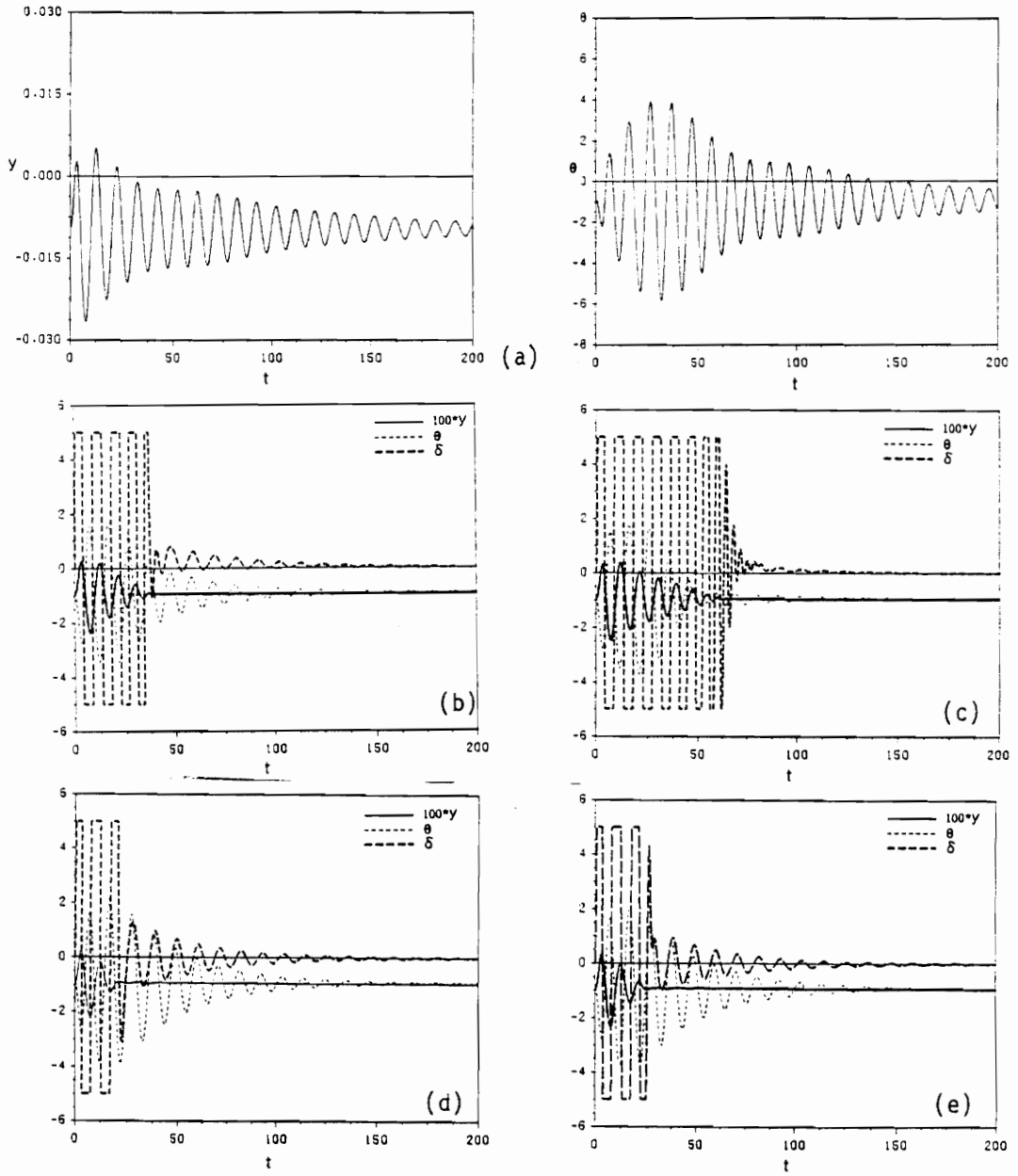

Figure 59. Motions (with/without feedback control) responding to a wind gust when $\alpha = 0°$ and $V_\infty = 85$ ft/sec: for the delayed control, $\ddot{\delta} + 4\dot{\delta} + 10(\delta - \delta_c) = 0$; and for the instantaneous control, $\delta = \delta_c$. $\delta_{max} = 5°$. (a) The motion without control; (b) the instantaneous control and $\delta_c = 114(y - y_e) + 172\dot{y}$; (c) the delayed control and $\delta_c = 114(y - y_e) + 172\dot{y}$; (d) The instantaneous control and $\delta_c = 172\dot{y}$; (e) the delayed control and $\delta_c = 172\dot{y}$.

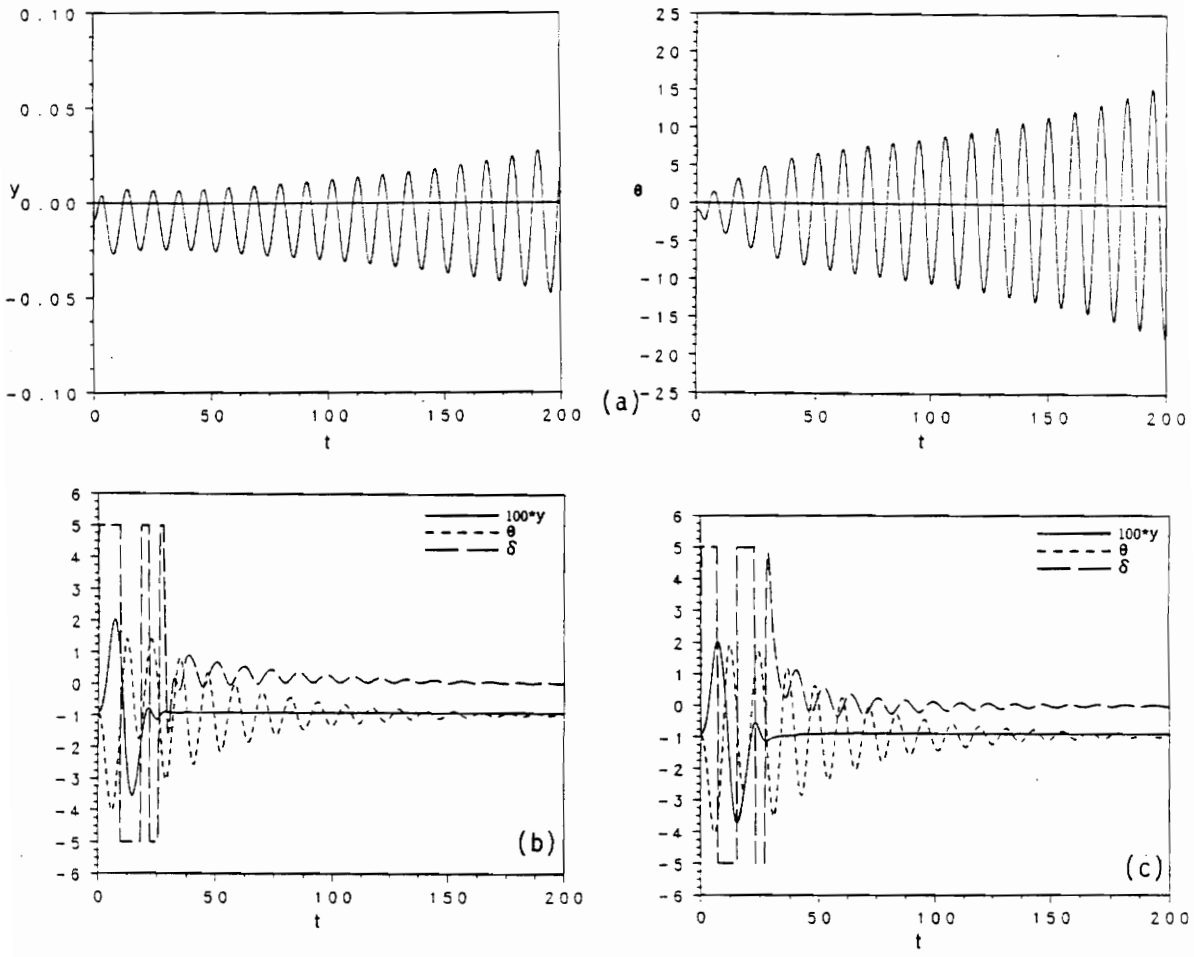

Figure 60. Motions (with/without feedback control) responding to a wind gust when $\alpha = 0°$ and $V_\infty = 90$ ft/sec: for the instantaneous control, $\delta = \delta_c$. $\delta_{max} = 5°$. (a) The motion without control; (b) the instantaneous control and $\delta_c = 114(y - y_e) + 172\dot{y}$; (c) The instantaneous control and $\delta_c = 172\dot{y}$.

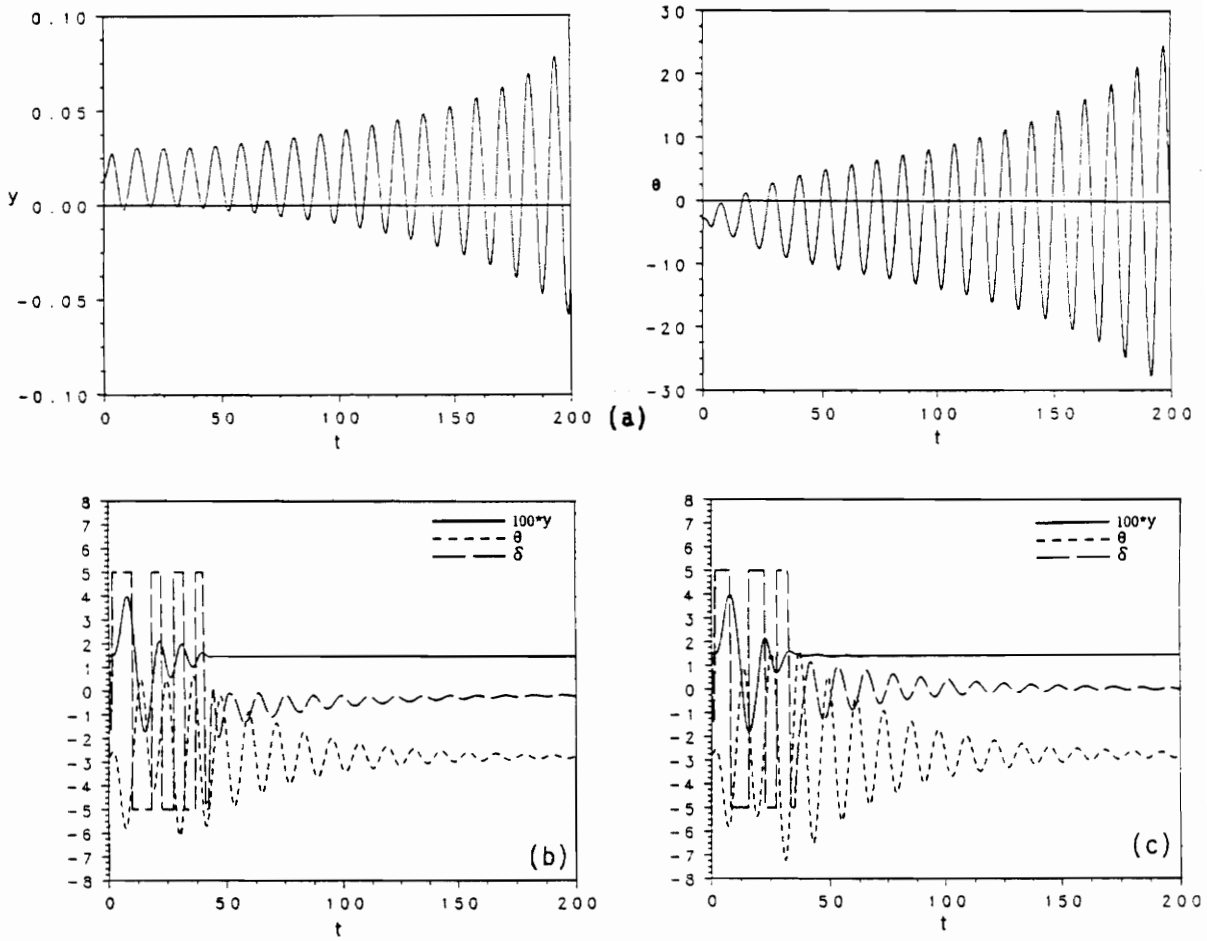

Figure 61. Motions (with/without feedback control) responding to a wind gust when $\alpha = 5°$ and $V_\infty = 91$ ft/sec: for the instantaneous control, $\delta = \delta_c$. $\delta_{max} = 5°$. (a) The motion without control; (b) the instantaneous control and $\delta_c = 114(y - y_e) + 172\dot{y}$; (c) The instantaneous control and $\delta_c = 172\dot{y}$.

Chapter 6. Conclusions

A general aerodynamic model for two-dimensional inviscid flows based on a vorticity panel method was developed. This model was used to simulate the wake generated by an oscillating airfoil and the blade-vortex interaction. This model was also coupled with dynamics and feedback control to simulate the flutter motion of an airfoil and to suppress the flutter motion and the response to a wind gust.

The present aerodynamic model is very adequate to simulate two-dimensional lifting flows. The condition imposed at the trailing edge of the airfoil is reasonable when the frequency of the oscillation is not very high. The solutions obtained by using this model show a convergent trend when the number of elements that represent the surface of the airfoil increases and the time step decreases.

The use of vortex blobs and the scheme of splitting blobs in the wake is successful in the wake simulation. The numerically calculated wakes agree very well with the experimental ones: the numerically predicted spacing of the wake structures, circulations around the regions of concentrated vorticity, and the velocity profiles across those regions are in close agreement with experimental results. This simulation based on the inviscid flow gives strong

support to the argument that the evolution of the wake, at least within a certain distance behind the airfoil, is mainly controlled by an inviscid mechanism.

The case of the blade-vortex interaction is more complicated than the simulation of wakes. For the cases where the wake generated by the pitching airfoil does not brush the stationary airfoil (i.e. interaction is not very close) the numerical results are in good agreement with the experimental ones. When the passing vorticity slows the flow on the facing surface, separation might occur and cause some discrepancy between the numerical and experimental results because the separation is not taken into account in the numerical model. But this discrepancy is not very large and only happens when the region of concentrated vorticity approaches and leaves the trailing edge, so the numerical model still predicts a qualitatively good solution for such cases. When the wake passed by very closely, enveloping the stationary airfoil, the numerical solutions fail to match the experimental results, probably because of the severe separation caused by the close interaction.

The coupled model of aerodynamics/dynamics predicts the flutter motion accurately. The effect of the static angle of attack on the critical flutter speed is investigated, and when the static angle of attack is within eight degrees, the critical flutter speed is about same. Also the effect of the nonlinearity of the elastic support (cubic term in the hardening spring) is investigated by this model.

Feedback control is coupled with the model of aerodynamics/dynamics, and the combination is used to simulate the suppression of the flutter motion of the airfoil. With carefully designed control laws, the oscillations triggered by small disturbances can be suppressed. The numerical results show different control variables can be used. The efficiency of the control depends on the allowed maximum angle of the flap (control surface at the trailing edge) and the control variables used in the control law. Without any change in the gains, control laws using either y and $\dot{y}$ or only $\dot{y}$ can be used to suppress the flutter motion

for different static angles of attack. The model of aerodynamics/dynamics/control is also used to suppress the response to a wind gust with the same control laws as used for the flutter suppression.

If the problem is restricted to one degree of freedom, under normal circumstances, the motion of the airfoil can only be damped by the flow because the aerodynamic loads do negative work, i.e. the motion loses energy to the flow. In the problems of two degrees of freedom, the phase difference between y and θ makes the energy exchange between the flow and motion of the airfoil possible. Whether the motion is growing or not depends on the direction in energy exchange. When the flow speed is low, the flow acts like damping, while above the critical flutter speed the flow behaves as an exciter. In the present work, if without feedback control, the lift always does positive work to the motion and the moment always does negative work, and the flow speed influences the balance between the positive and negative work. When feedback control is added to the system, the lift does negative work and the moment does positive work; the net work done by the lift and moment is negative. In other words, the lift has major influence on the motion: flutter might happen when the lift does positive work; and the lift does negative work when the motion is suppressed by feedback control.

The present model treats the airfoils, the wakes, the elastic supports, and the control devices as an integral system and solves the problems simultaneously and interactively. The approach of this model is general. Other aerodynamic models and (nonlinear) control laws can be used. Moreover, one could even use a set of manufacturer-supplied characteristics for the motors driving the flap in place of the so-called servo equations.

References

1. Anderson, J. D., Jr., **Fundamentals of Aerodynamics,** McGraw Hill, New York, 1984.

2. Aref, H., "Integrable, Chaotic and Turbulent Vortex Motion in Two-Dimensional Flows," Annual Review of Fluid Mechanics, Vol. 15, 1983, pp. 345-389.

3. Aref, H., Kadtke, J. B., and I. Zawadzki, "Point Vortex Dynamics: Recent Results and Open Problems," The Japan Society of Fluid Mechanics, Vol. 3, 1988, pp. 63-74.

4. Aref, H. and Kambe, T., "Report on the IUTAM Symposium: Fundamental Aspects of Vortex Motion," Journal of Fluid Mechanics, Vol. 190, 1988, pp. 571-595.

5. Basu, B. C. and Hancock, G. J., "The Unsteady Motion of a Two-Dimensional Airfoil in Incompressible Inviscid Flow," Journal of Fluid Mechanics, Vol. 87, 1978, pp. 159-178.

6. Bennett, R. M., Batina, J. T., and Cunningham, H. J., "Wing Flutter Calculation with the CAP-TSD Unsteady Transonic Small Disturbance Program," AIAA Paper, No. 88-2347, 1988.

7. Booth, E. R., Jr., "Surface Pressure Measurement During Low Speed Two-Dimensional Blade-Vortex Interaction," AIAA Paper No. 86-1856, 1986.

8. Booth, E. R., Jr., "Measurement of Velocity and Vorticity Fields in the Wake of an Airfoil in Periodic Pitching Motion," NASA TP-2780, 1987.

9. Booth, E. R., Jr., "Experimental Observations of Two Dimensional Blade-Vortex Interaction," AIAA Paper No. 87-2745, 1987.

10. Booth, E. R., Jr. and Yu, J. C., "New Technique for Experimental Generation of Two-Dimensional Blade-Vortex Interaction at Low Reynolds Number," NASA TP-2551, 1986.

11. Booth, E. R., Jr. and Yu, J. C., "Two-Dimensional Blade-Vortex Flow Visualization Investigation," AIAA Journal, Vol. 24, pp. 1467-1473; also NASA TP-2551, 1986.

12. Borland, C. J. and Rizzetta, D. P., "Nonlinear Transonic Flutter Analysis," AIAA Journal, Vol. 20, November, 1981, pp. 1606-1615.

13. Bratt, J. B., "Flow Patterns in the Wake of an Oscillating Airfoil," Aeronautical Research Council Reports and Memoranda No. 2773, 1950.

14. Caflisch, R. E., "Nonlinear Analysis for the Evolution of Vortex Sheets," Fluid Dynamics Research, Vol. 3, 1988, pp. 75-77.

15. Carnahan, B., Luther, H. A. and Wilkes, J. O., **Applied Numerical Methods,** John Wiley & Sons Inc., NY, 1969.

16. Chorin, A. J. and Bernard, P. S., "Discretization of a Vortex Sheet, With An Example of Roll Up," Journal of Computational Physics, Vol. 13, 1973, pp. 423-428.

17. Chow, C.-Y. and Huang, M.-K., "Unsteady Flow About a Joukowski Airfoil in the Presence of Moving Vortices," AIAA Paper No. 83-0129, 1983.

18. Cunningham, H. J., Batina, J. T., and Bennett, R. M., "Modern Wing Flutter Analysis by Computational Fluid Dynamics Methods," Journal of Aircraft, Vol. 25, No. 10, 1988, pp.962-968.

19. Damodaran, M. and Caughey, D. A., "Finite-Volume Calculation of Inviscid Transonic Airfoil-Vortex Interaction," AIAA Journal, Vol. 26, No. 11, November, 1988, pp. 1346-1353.

20. Dong, B. and Mook, D. T., "Numerical Simulation of Unsteady Aeroelastic Behavior," Proceedings of the SECTAM XV 1990 Southeastern Conference on Theoretical and Applied Mechanics, Atlanta, GA, March 22-23, 1990.

21. Dong, B. and Mook, D. T., "Numerical and Asymptotic Analysis of the Flutter Phenomenon for an Airfoil," Proceedings of the Third Conference on the Nonlinear Vibrations, Stability and Dynamics of Structures and Mechanisms, Blacksburg, VA, Vol. XV, June 25-27, 1990, pp. 102-110.

22. Dong, B. and Mook, D. T., "Numerical Simulation of Flutter Suppression by Feedback Control," Proceedings of the Conference on Recent Advances in Active Control of Sound and Vibration, Blacksburg, VA, April 15-17, 1991.

23. Dong, B. and Mook, D. T., "Numerical Simulation of Wakes with Application to Blade-Vortex Interaction," Proceedings of the Third International Congress of Fluid Mechanics, Cairo, Egypt, January, 2-4, 1990, Vol. 2, pp. 765-775.

24. Dong, B., "Numerical Simulation of Two-Dimensional Lifting Flow," Master Thesis, Department of Engineering Science and Mechanics, Virginia Polytechnic Institute and State University, Blacksburg, Virginia, 1987.

25. Dowell, E. H., "Nonlinear Aeroelasticity," AIAA-90-1031-CP, 1990.

26. Fung, Y. C., **The Theory of Aeroelasticity,** Dover Publications, NY, 1969.

27. Giesing, J. P., "Nonlinear Two-Dimensional Unsteady Potential Flow with Lift," Journal of Aircraft, Vol. 5, 1968, pp. 135-143.

28. Giesing, J. P., "Vorticity and Kutta Condition for Unsteady Multienergy Flows," Journal of Applied Mechanics, Vol. 36, 1969, pp. 608-613.

29. Guruswamy, P. and Yang, T. Y., "Aeroelastic Time Response Analysis of Thin Airfoils by Transonic Code LTRAN2," Computers and Fluids, Vol. 9, 1981, pp. 409-425.

30. Guruswamy, G. P., "Unsteady Aerodynamic and Aeroelastic Calculation for Wings Using Euler Equations," AIAA Journal, Vol. 28, No. 3, March 1990, pp. 461-469.

31. Hardin, J. C. and Lamkin, S. L., "Aeroacoustic Interaction of a Distributed Vortex with a Lifting Joukowski Airfoil," AIAA Paper No. 84-2237, 1984.

32. Hauenstein, A. J., Laurenson, R. M., Eversman, W., Galecki, G., Qumei, I., and Amos, A. K., "Chaotic Response of Aerosurfaces with Structural Nonlinearities," AIAA-90-1034-CP, 1990.

33. Helmholtz, H., von, 1858, "On Integrals of the Hydrodynamic Equations Which Express Vortex Motion," Translation by P. G. Tait, 1867, Philosophical Magazine Vol. 4, pp. 485-512.

34. Ho, C. M. and Chen, S. H., "Unsteady Wake of a Plunging Airfoil," AIAA Paper No. 80-1446, 1980.

35. Ho, C. M. and Chen, S. H., "Unsteady Kutta Condition of a Plunging Airfoil," **Unsteady turbulent Shear Flows** , R. Michel et al. Eds., Springer, Berlin, 1981, pp. 197-206.

36. Hsu, T. M. and Wu, J. C., "Theoretical and Numerical Studies of a Vortex-Airfoil Interaction Problem," AIAA Paper No. 86-1094, 1986.

37. Hsu, T.-M. and Wu, J. C., "Vortex Flow Model for the Blade-Vortex Interaction Problem," AIAA Journal, Vol. 26, 1988, pp. 621-623.

38. Huang, M.-K. and Chow, C.-Y., "Tapping of a Free Vortex by Joukowski Airfoil," AIAA Journal, Vol. 20, No. 3, March, 1982, pp. 292-298.

39. Huttse, L. J. and Eastep, F. E., "Improved Unsteady Aerodynamics and Flutter for NACA 0012 Airfoil at Angle of Attack," AIAA Paper, No. 88-2349, 1988.

40. Kim, M. J. and Mook, D. T., "Application of Continuous Vorticity Panels to General Unsteady Two-Dimensional Lifting Flows," J. Aircraft, Vol. 23, 1986, pp. 464-471.

41. Koochesfahani, M. M., "Vortical Patterns in the Wake of an Oscillating Airfoil," AIAA Journal, Vol. 27, No. 9, September, 1989.

42. Krasny, R., "A Study of Singularity Formation in a Vortex Sheet by the Point-Vortex Approximation," Journal of Fluid Mechanics, Vol. 167, 1986, pp. 65-93.

43. Krasny, R., "Desingularization of Periodic Vortex Sheet Roll-up," Journal of Computational Physics, Vol. 65, 1988, pp. 292-313.

44. Krasny, R., "Numerical Simulation of Vortex Sheet Evolution," Fluid Dynamics Research, Vol. 3, 1988, pp. 93-97.

45. Lee, D. J. and Smith, C. A., "Distortion of the Vortex Core During Blade/Vortex Interaction," AIAA Paper No. 87-1243, 1987.

46. Lee, B. H. K. and LeBlanc, P., "Flutter Analysis of a Two-Dimensional Airfoil with Cubic Non-Linear Restoring Force," Aeronautical Note, NAE-AN-36, NRC NO. 25438, N87-22628, 1986.

47. Lee, B. H. K. and Desrochers J., "Flutter Analysis of a Two-Dimensional Airfoil Containing Structural Nonlinearities," Aeronautical Note, LR-618, NRC NO. 27833, 1987.

48. Leonard, A., 1980, "REVIEW Vortex Methods for Flow Simulation," Journal of Computational Physics, Vol. 37, 1980, pp. 289-335.

49. Liu, X. L., Wo, A., and Covert, E. E., "Unsteady Streamlines Near the Trailing Edge of a NACA 0012 Airfoil at Reynolds Number of 125,000," AIAA Journal, Vol. 28, 1990, pp. 169-170.

50. Maskell, E. C., "On the Kutta-Joukowski Condition in Two-Dimensional Unsteady Flow," unpublished note, Royal Aircraft Establishment, Farnborough, England, 1971.

51. Maskew, B, "Calculation of Two-Dimensional Vortex-Surface Interference Using Panel Methods," NASA Contractor Report 159334, N81-13020, 1980.

52. Mathioulakis, D. S., Kim, M. J., Telionis, D. P., and Mook, D. T., "On the Wake of a Pitching Airfoil," AIAA Paper, No. 85-1621, 1985.

53. Matsuzaki, Y., Ueda, T., Miyazawa, Y. and Matsushita, Y., "Gust Load Alleviation of a Transport-Type Wing: Test and Analysis," Journal of Aircraft, Vol. 26, April 1989, pp. 322-327.

54. McCroskey, W. J., "Unsteady Airfoils," Annual Review of Fluid Mechanics, Vol. 14, 1982, pp. 285-311.

55. Meiron, D. I., Baker, G. R., and Orszag, S. A., "Analytical Structure of Vortex-Sheet Dynamics, Part 1. Kelvin-Helmholtz Instability," Journal of Fluid Mechanics, Vol. 114, 1982, pp. 283-298.

56. Mook, D. T., Roy, S., Choksi, G., and Alexander, D. M., "On the Numerical Simulation of the Unsteady Wake Behind an Airfoil," AIAA Paper No. 87-0190, 1987.

57. Mook, D. T., Roy, S., Choksi, G., and Dong, B., "Numerical Simulation of the Unsteady Wake Behind an Airfoil," Journal of Aircraft, Vol. 26, 1989, pp. 509-514.

58. Mook, D. T. and Dong, B., "Application of Vortex Dynamics to Simulations of the Wakes of Airfoils," Proceedings of the International Symposium on Nonsteady Fluid Dynamics, FED-Vol. 92, Toronto, Canada, June 4-7, 1990, pp. 435-448.

59. Moore, D. W., "The Spontaneous Appearance of a Singularity in the Shape of an Evolving Vortex Sheet," Proceedings of the Royal Society of London, A365, 1979, pp. 105-119.

60. Moore, D. W., "Numerical and Analytical Aspects of Helmholtz Instability, in: Theoretical and Applied Mechanics," Proceedings of the XVI IUTAM Conference, eds. Niordson and Olhoff (North-Holland, Amsterdam), 1984, pp. 629-633.

61. Mracek, C. P. and Mook, D. T., "Numerical Simulation of Three-Dimensional Lifting Flows by a Vortex Panel Method," AIAA Paper No. 88-4335-CP, 1988.

62. Niblett, L. T., "A Guide to Classic Flutter," Aeronautical Journal, November, 1988, pp. 339-354.

63. Nissim, E. and Burken, J. J., " Control Surface Spanwise Placement in Active Flutter Suppression Systems," NASA Technical Paper 2873, 1988. *.Steady and Unsteady Ground Effects," Journal of Aircraft, Vol. 26,

64. Nuhait, A. O., "Numerical Simulation of Wings in Steady and Unsteady Ground Effects and of of Feedback Control," Ph.D. Dissertation, Department of Engineering Science and Mechanics, Virginia Polytechnic Institute and State University, Blacksburg, VA, October, 1988.

65. Ohashi, H. and Ishikawa, N., "Visualization Study of Flow Near the Trailing Edge of an Oscillating Airfoil," Bulletin of the Japan Society of Mechanical Engineers, Vol. 15, 1972, pp. 840-847.

66. Ohta, H., Fujimori, A., Nikiforuk, P. N. and Gupta, M. M., "Active Flutter Suppression for Two-Dimensional Airfoil," Journal of Guidance and Control, Vol. 12, March-April 1989, pp. 188-194.

67. Panaras, A. G., "Numerical Modeling of the Vortex/Airfoil Interaction," AIAA Journal, Vol. 25, 1987, pp. 5-11.

68. Park, S. O., Kim, J. S., and Lee, B. I., "Hot-wire Measurements of Near Wakes Behind an Oscillating Airfoil," AIAA Paper No. 88-3715, 1988.

69. Poling, D. R., "Airfoil Response to Periodic Disturbances - the Unsteady Kutta Condition," Ph.D. Dissertation, Department of Engineering Science and Mechanics, Virginia Polytechnic Institute and State University, Blacksburg, VA, August, 1985.

70. Poling, D. R. and Telionis, D. P., "The Response of Airfoils to Periodic Disturbances - The Unsteady Kutta Condition," AIAA J., Vol. 24, 1986, pp. 193-199.

71. Poling, D. R. and Telionis, D. P., "The Trailing Edge of a Pitching Airfoil at High Reduced Frequencies," Journal of Fluids Engineering, Vol. 109, 1987, pp. 410-414.

72. Poling, D. R., Dadone, L., and Telionis, D. P., "Blade-Vortex Interaction," AIAA Paper No. 87-0497, 1987.

73. Poling, D. R., Wilder, M. C., and Telionis, D. P., "Two-Dimensional Interaction of Vortices with a Blade," AIAA Paper No. 88-0044, 1988.

74. Pozrikidis, C. and Higdon, J. J. L., "Nonlinear Kelvin-Helmholtz Instability of a Finite Vortex Layer," Journal of Fluid Mechanics, Vol. 157, 1985, pp. 225-263.

75. Raj, P. and Gray, R. B., "Computation of Two-Dimensional Potential Flow Using Elementary Vortex Distributions," Journal of Aircraft, Vol. 15, 1978, pp. 698-700.

76. Rausch, R. D., Batina, J. T., and Yang, H. T. Y., "Euler Flutter Analysis of Airfoils Using Unstructured Dynamic Meshes," Journal of Aircraft, Vol. 27, No. 5, 1990, pp. 436-443.

77. Rizzetta, D. P., "Time-Dependent Responses of a Two-Dimensional Airfoil in Transonic Flow," AIAA Journal, Vol, 17, 1979, pp. 26-32.

78. Rizzetta, D. P., "Transonic Flutter Analysis of a Two-Dimensional Airfoil," AFFDL, TM-77-64-FBR, 1977.

79. Rosenhead, L., "The Formation of Vortices from a Surface of Discontinuity," Proceedings of the Royal Society of London, A134, 1931, pp. 170-192.

80. Sarpkaya, T., "Computational Methods with Vortices - The 1988 Freeman Scholar Lecture," Journal of Fluids Engineering, Vol. 111, 1989, pp. 5-52.

81. Sarpkaya, T. and Schoaff, R. L., "Inviscid Model of Two-Dimensional Vortex Shedding by a Circular Cylinder," AIAA Journal, Vol. 17, 1979, pp. 1193-1200.

82. Sears, W. R., "Aerodynamics, Noise, and Sonic Boom," AIAA Journal, Vol. 7, April 1969, pp. 577-586.

83. Sommerfeld, A., **Mechanics of Deformable Bodies,** Academic Press, New York, New York, 1964.

84. Spalart, P. R., "Vortex Methods for Separated Flows," NASA Technical Memorandum 100068, N88-26342, 1988.

85. Srinivasan, G. R., McCroskey, W. J., and Kutler, P., "Numerical Simulation of the Interaction of a Vortex with Stationary Airfoil in Transonic Flow," AIAA Paper No. 84-0254, 1984.

86. Srinivasan, G. R., "Computations of Two-Dimensional Airfoil-Vortex Interactions," NASA Contractor Report 3885, 1985.

87. Srinivasan, G. R., McCroskey, W. J., and Baeder, J. D., "Aerodynamics of Two-Dimensional Blade-Vortex Interaction," AIAA Journal, Vol. 24, pp. 1569-1576, 1986.

88. Straus, J., Renzoni, P., and Mayle, R. E., "Airfoil Pressure Measurements During a Blade Vortex interaction and a Comparison with Theory," AIAA Journal, Vol. 28, No. 2, February, 1990, pp. 222-228.

89. Strganac, T. W. and Mook, D. T., " The Numerical Simulation of Subsonic Flutter," AIAA-87-1428, 1987.

90. Strganac, T. W. and Mook, D. T., "Numerical Model of Unsteady Subsonic Aeroelastic Behavior," AIAA Journal, Vol. 28, 1990, pp. 903-909.

91. Telionis, D. P., Private Communications, 1990.

92. Wilder, M. C., Mathioulakis, D. S., Poling, D. R., Dong, B., Mook, D. T. and Telionis, D. P., "On the Wake of a Pitching Airfoil," submitted for publication, 1990.

93. Wu, J. C. and Sankar, N. L., "Aerodynamic Force and Moment in Steady and Time-Dependent Viscous Flows," AIAA Paper No. 80-0011, 1980.

94. Wu, J. C., Sankar, N. L., and Hsu, T. M., "Unsteady Aerodynamics of an Airfoil Encountering a Passing Vortex," AIAA Paper No. 85-0203, 1985.

95. Wu, J. C. and Thompson, J. F., "Numerical Solutions of Time-Dependent Incompressible Navier-Stokes Equations Using an Integro-Differential Formulation," Computer and Fluids, Vol. 1, 1973, pp. 197-215.

96. Yang, T. Y., Guruswamy, P. and Striz, A. G., "Aeroelastic Response Analysis of Two-Dimensional, Single and Two Degree of Freedom Airfoils in Low Frequency, Small Disturbance Unsteady Transonic Flow," AFFDL, TR-79-3077, 1979.

97. Yang, T. Y., Guruswamy, P., Striz, A. G. and Olsen, J. J., "Flutter Analysis of a NACA 64A006 Airfoil in Small Disturbance Transonic Flow," Journal of Aircraft, Vol. 17, 1980, pp. 225-232.

98. Yang, Z. C. and Zhao, L. C., "Analysis of Limit Cycle Flutter of an Airfoil in incompressible Flow," Journal of Sound and Vibration, Vol. 123, No. 1, 1988, pp. 1-13.

99. Zhao, L. C. and Yang, Z. C., "Chaotic Motions of an Airfoil with Non-Linear Stiffness in Incompressible Flow," Journal of Sound and Vibration, Vol. 138, No. 2, 1990, pp. 245-254.

100. "Generation of Circulation and Lift for an Airfoil," Film Loop SFM10, a production of National Committee for Fluid Mechanics Films, with the support of the National Science Foundation, produced by Education Development Center, Inc., distributed by Encyclopedia Britannica Educational Corp. Experiments done under the direction of L. Prandtl. Film edited by A. H. Shapiro and R. Bergman.

Appendix A.

In this appendix, the derivations of Equations (2.3.1), (2.3.2), (2.1.3) and (2.1.4) are presented for two dimensional problems, which were originally given by Wu and Thompson (1973) and Wu and Sankar (1980) for both two-dimensional and three-dimensional cases.

A.1 Basic Vector Calculus

The following formulas are used in the derivations in Sections A.2.

$$\nabla \times (\vec{A} \times \vec{B}) = (\vec{B} \cdot \nabla)\,\vec{A} - (\vec{A} \cdot \nabla)\,\vec{B} + \vec{A}\nabla \cdot \vec{B} - \vec{B}\nabla \cdot \vec{A} \qquad (A.1.1)$$

$$\nabla(\vec{A} \cdot \vec{B}) = (\vec{A} \cdot \nabla)\,\vec{B} + + (\vec{B} \cdot \nabla)\,\vec{A} + \vec{A} \times (\nabla \times \vec{B}) + \vec{B} \times (\nabla \times \vec{A}) \qquad (A.1.2)$$

$$\nabla \times (\nabla e) = 0 \qquad (A.1.3)$$

where e is a scalar.

$$\nabla \cdot (\vec{A} \times \vec{B}) = \vec{B} \cdot (\nabla \times \vec{A}) - \vec{A} \cdot (\nabla \times \vec{B}) \qquad (A.1.4)$$

Using Equation (A.1.4), one derives the following

$$\nabla \cdot [\vec{A} \times (\nabla \times \vec{B}) - \vec{B} \times (\nabla \times \vec{A})] = \vec{B} \cdot [\nabla \times (\nabla \times \vec{A})] - \vec{A} \cdot [\nabla \times (\nabla \times \vec{B})] \tag{A.1.5}$$

Gauss' theorem is expressed as follows

$$\int_S \nabla \cdot \vec{A}\, dS = \oint_c \vec{A} \cdot \vec{n}\, d\ell \tag{A.1.6}$$

where S is the region bounded by the surface c and $\vec{n}$ is the unit outward normal vector to a small differential element $d\ell$ on c. From Equations (A.1.5) and (A.1.6), the following equation is obtained

$$\int_S \{\vec{B} \cdot [\nabla \times (\nabla \times \vec{A})] - \vec{A} \cdot [\nabla \times (\nabla \times \vec{B})]\} dS = \oint_c [\vec{A} \times (\nabla \times \vec{B}) - \vec{B} \times (\nabla \times \vec{A})] \cdot \vec{n}\, d\ell \tag{A.1.7}$$

From

$$\vec{A} \times \nabla b = b\, \nabla \times \vec{A} - \nabla \times (b\, \vec{A}) \tag{A.1.8}$$

where b is a scalar and

$$\oint_c [\nabla \times (b\, \vec{A})] \cdot \vec{n}\, d\ell = \int_S \nabla \cdot [\nabla \times (b\, \vec{A})]\, dS = 0 \tag{A.1.9}$$

one derives the following

$$\oint_c (\vec{A} \times \nabla b) \cdot \vec{n}\, d\ell = \oint_c (b\, \nabla \times \vec{A}) \cdot \vec{n}\, d\ell \tag{A.1.10}$$

The following equations are used in the derivations in Sections A.3.

$$\nabla^2 \vec{A} = \nabla(\nabla \cdot \vec{A}) - \nabla \times (\nabla \times \vec{A}) \tag{A.1.11}$$

$$\int_S \nabla \times \vec{A}\, dS = \oint_c \vec{n} \times \vec{A}\, d\ell \qquad (A.1.12)$$

A.2 Kinematics of Flows

Here only the two-dimensional flow is considered

$$\frac{\partial}{\partial z} \equiv 0 \qquad (A.2.1)$$

and the velocity

$$\vec{V} = V_x \vec{i} + V_y \vec{j} + 0\,\vec{k} \qquad (A.2.2)$$

in a right-hand coordinate system (x, y, z) .

Because the velocity $\vec{V}$ of the incompressible fluid satisfies Equation (2.1.1) and is solenoidal, there is a vector potential $\vec{Q}$ satisfying

$$\vec{V} = \nabla \times \vec{Q} \qquad (A.2.3)$$

where $\vec{Q}$ can be chosen as

$$\vec{Q} = Q_z(x, y)\,\vec{k} \qquad (A.2.4)$$

because $\vec{V}$ has no component in z-direction.

From Equation (A.2.3), Equation (2.1.2) becomes

$$\vec{\Omega} = \nabla \times (\nabla \times \vec{Q}) \qquad (A.2.5)$$

For two-dimensional problems, let

$$\vec{P} = \nabla(\ln\frac{1}{r'}) \times \vec{a} \qquad (A.2.6)$$

where

$$r' = |\vec{r} - \vec{r}_0| \qquad (A.2.7)$$

is the distance between two points $\vec{r}$ and $\vec{r}_0$ in the flowfield, the Laplace operator ∇ is performed on $\vec{r}_0$, and $\vec{a}$ is chosen as an arbitrary constant unit vector on x,y-plane so that $\vec{P}$ is only in z-direction.

It is straightforward to verify that:

$$\nabla \cdot \left[\nabla(\ln\frac{1}{r'})\right] = 0 \qquad (A.2.8)$$

From Equations (A.1.1), (A.1.2), (A.1.3) and (A.2.8), it is easy to verify that, if $r' \neq 0$,

$$\nabla \times \vec{P} = \nabla[\vec{a} \cdot \nabla(\ln\frac{1}{r'})] \qquad (A.2.9)$$

and then

$$\nabla \times (\nabla \times \vec{P}) = 0 \qquad (A.2.10)$$

From Equations (A.1.7), (A.2.3), (A.2.5) and (A.2.10), $\vec{P}$, $\vec{Q}$, $\vec{V}$ and $\vec{\Omega}$ satisfy the following equation

$$\int_{S_f} \vec{P} \cdot \vec{\Omega}\, dS_f(\vec{r}_0) = \oint_{C_f} [\vec{Q} \times (\nabla \times \vec{P}) - \vec{P} \times \vec{V}] \cdot \vec{n}_f\, d\ell(\vec{r}_0) \qquad (A.2.11)$$

where S_f is the region of the flowfield bounded by C_f, and $\vec{n}_f$ is the unit outward vector normal to C_f. It should be mentioned that Equation (A.1.7) is generally for three-dimensional problems and it can be used two-dimensionally just

because the vector integrands in the right-hand side of Equation (A.2.11) have no components in z-direction.

From Equation (A.2.6), the integrand of the left-hand side of Equation (A.2.11) can be rewritten as

$$\begin{aligned}\vec{P}\cdot\vec{\Omega} &= [\nabla(\ln\frac{1}{r'})\times\vec{a}]\cdot\vec{\Omega} \\ &= \vec{a}\cdot[\vec{\Omega}\times\nabla(\ln\frac{1}{r'})]\end{aligned} \qquad (A.2.12)$$

From Equations (A.2.9), (A.1.10) and (A.2.6), the first term of the right-hand side of Equation (A.2.11) becomes

$$\oint_{C_f}[\vec{Q}\times(\nabla\times\vec{P})]\cdot\vec{n}_f\,d\ell = \oint_{C_f}[\vec{a}\cdot\nabla(\ln\frac{1}{r'})]\vec{V}\cdot\vec{n}_f\,d\ell \qquad (A.2.13)$$

From Equation (A.2.6), the second term of the integrand of the right-hand side of Equation (A.2.11) can be rewritten as

$$\begin{aligned}(\vec{P}\times\vec{V})\cdot\vec{n}_f &= \{[\nabla(\ln\frac{1}{r'})\times\vec{a}]\times\vec{V}\}\cdot\vec{n}_f \\ &= \{[\nabla(\ln\frac{1}{r'})\cdot\vec{V}]\vec{a} - (\vec{a}\cdot\vec{V})\nabla(\ln\frac{1}{r'})\}\cdot\vec{n}_f \\ &= \{[\nabla(\ln\frac{1}{r'})\cdot\vec{V}]\vec{n}_f - [\nabla(\ln\frac{1}{r'})\cdot\vec{n}_f]\vec{V}\}\cdot\vec{a} \\ &= \vec{a}\cdot[(\vec{V}\times\vec{n}_f)\times\nabla(\ln\frac{1}{r'})]\end{aligned} \qquad (A.2.14)$$

Then Equation (A.2.11) becomes

$$\begin{aligned}\int_{S_f}\vec{a}\cdot[\vec{\Omega}\times\nabla(\ln\frac{1}{r'})]dS_f = &\oint_{C_f}\vec{a}\cdot\nabla(\ln\frac{1}{r'})(\vec{V}\cdot\vec{n}_f)\,d\ell \\ &-\oint_{C_f}\vec{a}\cdot[(\vec{V}\times\vec{n}_f)\times\nabla(\ln\frac{1}{r'})]\,d\ell\end{aligned} \qquad (A.2.15)$$

Because $\vec{a}$ is an arbitrary constant unit vector (non-zero), Equation (A.2.15) becomes

$$\int_{S_f} [\vec{\Omega} \times \nabla(\ln \frac{1}{r'})] dS_f = \oint_{C_f} [(\vec{V} \bullet \vec{n}_f)\nabla(\ln \frac{1}{r'}) - (\vec{V} \times \vec{n}_f) \times \nabla(\ln \frac{1}{r'})] d\ell \qquad (A.2.16)$$

Let the region S_f be multiply connected, and $C_f = C + C_0 + C_1$ be the boundaries, where C is the contour of an airfoil in the flow, C_0 is a small circle of radius ε centered at $\vec{r}$ and C_1 is a large circle of radius R centered at $\vec{r}$.

It is easy to verify that

$$\nabla(\ln \frac{1}{r'}) = \frac{\vec{r} - \vec{r}_f}{|\vec{r} - \vec{r}_f|^2} \qquad (A.2.17)$$

On C_0,

$$d\ell = \varepsilon d\theta \qquad \text{for } 0 \le \theta \le 2\pi \qquad (A.2.18)$$

and according Equation (A.2.17)

$$\nabla(\ln \frac{1}{r'}) = \frac{\vec{n}_f}{\varepsilon} \qquad (A.2.19)$$

Then, on C_0, the right-hand side of Equation (A.2.16) is

$$\begin{aligned} &\oint_{C_0} [(\vec{V} \bullet \vec{n}_f)\nabla(\ln \frac{1}{r'}) - (\vec{V} \times \vec{n}_f) \times \nabla(\ln \frac{1}{r'})] d\ell \\ &= \int_0^{2\pi} [(\vec{V} \bullet \vec{n}_f)\, \vec{n}_f - (\vec{V} \times \vec{n}_f) \times \vec{n}_f] d\theta \qquad (A.2.20) \\ &= \int_0^{2\pi} \vec{V} d\theta \end{aligned}$$

and as $\varepsilon \to 0$,

$$\int_0^{2\pi} \vec{V} d\theta \rightarrow 2\pi \vec{V}(\vec{r}) \tag{A.2.21}$$

Similarly, on C_1,

$$\nabla(\ln \frac{1}{r'}) = -\frac{\vec{n}_f}{R} \tag{A.2.22}$$

and as $R \rightarrow \infty$,

$$\oint_{C_1} [(\vec{V} \bullet \vec{n}_f)\nabla(\ln \frac{1}{r'}) - (\vec{V} \times \vec{n}_f) \times \nabla(\ln \frac{1}{r'})] d\ell \rightarrow -2\pi \vec{V}_\infty \tag{A.2.23}$$

where $\vec{V}_\infty$ is the velocity of the freestream. From Equations (A.2.16), (A.2.21) and (A.2.23), the velocity at $\vec{r}$ is

$$\vec{V}(\vec{r}) = \frac{1}{2\pi} \left\{ \int_{S_f} \vec{\Omega} \times \nabla(\ln \frac{1}{r'}) dS_f - \oint_C [(\vec{V} \bullet \vec{n}_f)\nabla(\ln \frac{1}{r'}) - (\vec{V} \times \vec{n}_f) \times \nabla(\ln \frac{1}{r'})] d\ell \right\} + \vec{V}_\infty \tag{A.2.24}$$

On the curve C,

$$\vec{n}_f = -\vec{n} \tag{A.2.25}$$

where $\vec{n}$ is the unit outward-pointing vector normal to the curve C, and

$$\vec{V} = \vec{v}_\ell \tag{A.2.26}$$

where $\vec{v}_\ell$ is the velocity of fluid next to the contour of the airfoil, which is equal to the velocity of the airfoil according to no-slip and no-penetration conditions.

The second term of the right-hand side in Equation (A.2.24) is the contribution from the motion of the airfoil, i.e.,

$$\vec{V}_a = -\frac{1}{2\pi}\oint_C [(\vec{V}\bullet\vec{n}_f)\nabla(\ln\frac{1}{r'}) - (\vec{V}\times\vec{n}_f)\times\nabla(\ln\frac{1}{r'})]d\ell \qquad (A.2.27)$$

where $\vec{V}_a$ is the velocity induced by the rptation of the airfoil.

According to Equations (A.2.17), (A.2.25) and (A.2.26), it is easy to verify that the right-hand side of Equation (A.2.27) is equal to the right-hand side of Equation (2.3.1).

For the motion of a rigid airfoil, the velocity $\vec{V}_a$ is also solenoidal and satisfies Equation (2.1.1):

$$\nabla\bullet\vec{V}_a = 0 \qquad (A.2.28)$$

Then following the derivation of Equation (A.2.5) through Equation (A.2.16), one can prove that $\vec{V}_a$ also satisfies Equation (A.2.16)

$$\int_{S_a}[\vec{\Omega}\times\nabla(\ln\frac{1}{r'})]dS_a = \oint_C [(\vec{V}_a\bullet\vec{n})\nabla(\ln\frac{1}{r'}) - (\vec{V}_a\times\vec{n})\times\nabla(\ln\frac{1}{r'})]d\ell \qquad (A.2.29)$$

where $\vec{\Omega}$ is given by Equation (2.3.3), S_a is the interior of the airfoil, and $\vec{n}$ is the unit outward-pointing vector normal to the contour of the airfoil C.

Because of the no-slip and no-penetration conditions on the surface of the airfoil, one has

$$\vec{V}_a = \vec{v}_\ell \qquad (A.2.30)$$

on the contour C.

With Equations (A.2.25), (A.2.29) and (A.2.30), Equation (A.2.27) can be rewritten as

$$\vec{V}_a = \frac{1}{2\pi} = \int_{S_a} \vec{\Omega} \times \nabla(\ln \frac{1}{r'}) dS_a \qquad (A.2.31)$$

With Equations (A.2.17) and (2.3.3), one can easily prove that the right-hand side of Equation (A.2.31) is equal to the right-hand side of Equation (2.3.2). And with Equations (A.2.27) and (A.2.31), Equation (2.1.3) can be obtained from Equation (A.2.24).

A.3 Principle of Total Vorticity Conservation

Because Equation (2.1.2), the vorticity $\vec{\Omega}$ satisfies

$$\nabla \bullet \Omega = 0 \qquad (A.3.1)$$

For two-dimensional incompressible flows, the vorticity transport equation is

$$\frac{d\vec{\Omega}}{dt} = \nu \nabla^2 \vec{\Omega} \qquad (A.3.2)$$

where ν is the coefficient of kinematic viscosity.

From Equations (A.1.11) and (A.3.1), Equation (A.3.2) becomes

$$\frac{d\vec{\Omega}}{dt} = -\nu \nabla \times (\nabla \times \vec{\Omega}) \qquad (A.3.3)$$

Integrate Equation (A.3.3) over the flowfield

$$\int_{S_f} \frac{d\vec{\Omega}}{dt} \, dS_f = -\nu \int_{S_f} \nabla \times (\nabla \times \vec{\Omega}) \, dS_f \qquad (A.3.4)$$

Because the flow is incompressible, $\frac{d}{dt}$ can be pulled out of the integral of Equation (A.3.4). With Equation (A.1.12), Equation (A.3.4) becomes

$$\frac{d}{dt}\int_{S_f}\vec{\Omega}\,dS_f = \nu\oint_{C_f}(\nabla\times\vec{\Omega})\times\vec{n}_f\,d\ell \qquad (A.3.5)$$

where the boundary $C_f = C + C_1$. The contribution of c, the contour of the airfoil, to Equation (A.3.5) is not zero; the contribution of C_1 , the boundary at infinity, to Equation (A.3.5) vanishes because Ω goes to zero exponentially as R goes to infinity (Wu and Sankar, 1980). Then Equation (A.3.5) becomes

$$\frac{d}{dt}\int_{S_f}\vec{\Omega}\,dS_f = -\nu\oint_{C}(\nabla\times\vec{\Omega})\times\vec{n}\,d\ell \qquad (A.3.6)$$

where $\vec{n} = -\vec{n}_f$ is the unit outward-pointing vector normal to C.

With Equations (2.1.2) and (A.1.11) Navier-Stokes Equation is

$$\frac{d\vec{V}}{dt} = -\frac{1}{\rho}\nabla p + \nu\nabla^2\vec{V} = -\frac{1}{\rho}\nabla p - \nu\nabla\times\vec{\Omega} \qquad (A.3.7)$$

for incompressible flows.

From Equation (A.3.7), one has

$$\oint_C \frac{d\vec{V}}{dt}\times\vec{n}\,d\ell = -\frac{1}{\rho}\oint_C \nabla p\times\vec{n}\,d\ell - \nu\oint_C(\nabla\times\vec{\Omega})\times\vec{n}\,d\ell \qquad (A.3.8)$$

With Equations (A.1.12) and (A.1.3), the integral of the first term of the right-hand side in Equation (A.3.8) becomes

$$\oint_C \nabla p\times\vec{n}\,d\ell = -\int_{S_a}\nabla\times(\nabla p)\,dS_a = 0 \qquad (A.3.9)$$

From Equations (A.3.6), (A.3.8) and (A.3.9), one has

$$\frac{d}{dt}\int_{S_f}\vec{\Omega}\,dS_f = \oint_C \frac{d\vec{V}}{dt}\times\vec{n}\,d\ell \qquad (A.3.10)$$

According no-slip and no-penetration conditions, $\frac{d\vec{V}}{dt}$ is same on the curve C for both the fluid and airfoil. Then from Equation (A.1.12)

$$\oint_C \frac{d\vec{V}}{dt}\times\vec{n}\,d\ell = -\int_{S_a}\nabla\times\frac{d\vec{V}_a}{dt}\,dS_a = -\frac{d}{dt}\int_{S_a}\vec{\Omega}dS_a \qquad (A.3.11)$$

where $\vec{V}_a$ is the velocity of the airfoil, and $\vec{\Omega}$ is defined by Equation (2.3.3).

From Equation (A.3.11), Equation (A.3.10) becomes

$$\frac{d}{dt}\left(\int_{S_f}\vec{\Omega}\,dS_f + \int_{S_a}\vec{\Omega}\,dS_a\right) = 0 \qquad (A.3.12)$$

With Equation (2.3.4), Equation (2.1.4) can be obtained from Equation (A.3.12).

Appendix B.

The theory of complex variables is used to derive Equation (2.6.6) calculating the force at the leading edge of a flat airfoil.

B.1 Complex Transformation

The function of Joukowski transformation is

$$z(\zeta) = \frac{b}{2}(\zeta + \frac{1}{\zeta}) \qquad (B.1.1)$$

where $z = x + iy$ and $\zeta = \xi + i\eta$ are the complex variables on z-plane and ζ-plane respectively, $i = \sqrt{-1}$, and b is a real positive number. Its inverse function is

$$\zeta(z) = \frac{1}{b}(z \pm \sqrt{z^2 - b^2}) \qquad (B.1.2)$$

The Joukowski transformation maps a unit circle ($|\zeta| = 1$) on ζ-plane into a flat plate of length $2b$ ($-b \leq x \leq b$ and $y = 0$) on z-plane.

The derivative of the Joukowski function is

$$\frac{dz}{d\zeta} = \frac{b}{2}(1 - \frac{1}{\zeta^2}) \tag{B.1.3}$$

and its limit at infinity ($|\zeta| \to \infty$) is

$$\left.\frac{dz}{d\zeta}\right|_{\infty} = \frac{b}{2} \tag{B.1.4}$$

B.2 Complex Potential and Velocity

According to the theory of complex variable in the ideal flow, if the complex velocity potential for a flow on ζ-plane is $W(\zeta)$, the potential for the corresponding flow on z-plane obtained through the transformation $z(\zeta)$ is $W[\zeta(z)]$. And then complex conjugates of the velocities, U (on ζ-plane) and V (on z-plane), respectively are

$$\begin{aligned} \overline{U} &= \frac{dW}{d\zeta} \\ \overline{V} &= \frac{dW}{dz} \end{aligned} \tag{B.2.1}$$

where the bars on the top of U and V represent complex conjugates. The relation between the velocities at infinity (the velocities of the freestream) on the both planes are

$$\overline{U}_{\infty} = \left.\frac{dW}{d\zeta}\right|_{\infty} = \left.\frac{dW}{dz}\right|_{\infty} \left.\frac{dz}{d\zeta}\right|_{\infty} = \frac{b}{2}\overline{V}_{\infty} \tag{B.2.2}$$

where U_{∞} is on ζ-plane, and V_{∞} is on z-plane and given by

$$V_{\infty} = v_{\infty} e^{i\alpha_{ins}} \tag{B.2.3}$$

where $v_{\infty} = |V_{\infty}|$, and α_{ins} is the instantaneous angle of attack.

On ζ-plane, the potential of the flow around a unit circle $|\zeta| = 1$ is

$$W(\zeta) = \overline{U}_{\infty}\zeta + \frac{U_{\infty}}{\zeta} + \frac{i\Gamma}{2\pi}\ln\zeta + \sum_{k=1}^{M}\frac{i\Gamma_k}{2\pi}\left[\ln(\zeta - \zeta_k) - \ln(\frac{1}{\zeta} - \overline{\zeta}_k)\right] \qquad (B.2.4)$$

where Γ and Γ_k are respectively the circulations (clockwise direction is positive) around the circle and the k^{th} vortex outside of the circle at the position ζ_k ($= \xi_k + i\eta_k$), and the second term in the summation is contributed by the vortices inside of the circle, which are images of those outside.

When the Joukowski transformation defined by Equation (B.1.1) is applied, $W[\zeta(z)]$ represent the potential of the flow around a flat plate of length $2b$ ($-b \le x \le b$ and $y = 0$) on z-plane, and the complex conjugate of the velocity V_{∞} is

$$\overline{V} = \frac{dW}{dz} = \frac{\frac{dW}{d\zeta}}{\frac{dz}{d\zeta}} \qquad (B.2.5)$$

From Equations (B.1.3), (B.2.3) and (2.2.4), Equation (B.2.5) becomes

$$\overline{V} = \frac{\left[v_{\infty}e^{-i\alpha_a}\zeta^2 - v_{\infty}e^{i\alpha_a} + \frac{i\Gamma\zeta}{b\pi} + \frac{i}{b\pi}\sum_{k=1}^{M}\Gamma_k\left(\frac{\zeta^2}{\zeta - \zeta_k} + \frac{\zeta}{1 - \zeta\overline{\zeta}_k}\right)\right]}{(\zeta - 1)(\zeta + 1)} \qquad (B.2.6)$$

Equation (B.1.2) can be rewritten as

$$\zeta + 1 = \frac{z + b \pm \sqrt{z^2 - b^2}}{b} = \frac{\sqrt{z + b}\,(\sqrt{z + b} \pm \sqrt{z - b})}{b} \qquad (B.2.7)$$

From Equations (B.2.6) and (B.2.7), the order of $\overline{V}$ in the neighborhood of the leading edge of the flat plate ($z = -b$ or $\zeta = -1$) is

$$|\bar{V}| \sim \left(\frac{1}{|\sqrt{z+b}|} \right) \qquad (B.2.8)$$

B.3 Force Acting at the Leading Edge of a Flat Airfoil

The Bernoulli equation is

$$\frac{\partial \phi}{\partial t} + \frac{p}{\rho} + \frac{|V|^2}{2} = f(t) \qquad (B.3.1)$$

where ϕ is the real velocity potential, p is the pressure, ρ is the density of the fluid, and $f(t)$ is a bounded function of time. Equation (B.3.1) can be rewritten as

$$p = \rho \left[f(t) - \frac{\partial \phi}{\partial t} - \frac{|V|^2}{2} \right] \qquad (B.3.2)$$

The force acting at the leading edge ($z = -b$) can be calculated by the following

$$\vec{F} = \oint_c (-p)\vec{n}\, d\ell \qquad (B.3.3)$$

where $\vec{n}$ is a unit outward pointing vector normal to the small circle c around the leading edge, which is given by

$$z + b = \varepsilon e^{i\theta} \qquad \text{for } 0 \le \theta \le 2\pi \qquad (B.3.4)$$

where ε is a small positive number.

From Equation (B.2.8), the order of ϕ is

$$\phi \sim O\left(\left|\sqrt{z+b}\,\right|\right) \tag{B.3.5}$$

i.e. $\dfrac{\partial \phi}{\partial t}$ is bounded around the trailing edge.

Because $f(t)$ and $\dfrac{\partial \phi}{\partial t}$ are bounded around the leading edge, they do not contribute to the integral in Equation (B.3.3) as ε in Equation (B.3.4) goes to zero. Then the Blasius' relation for steady flows can be used for the current unsteady case to calculate the complex force $F = F_x + iF_y$ at the leading edge

$$\bar{F} = \frac{i\rho}{2} \lim_{\varepsilon \to 0} \oint_c (\bar{V})^2 \, dz \tag{B.3.6}$$

From Equation (B.2.6) and (B.2.7), Equation (B.3.6) becomes

$$\bar{F} = \frac{i\rho}{2} \lim_{\varepsilon \to 0} \oint_c \frac{H}{z+b} \, dz \tag{B.3.7}$$

where

$$H = \frac{b^2 \left[v_\infty e^{-i\alpha_{ins}} \zeta^2 - v_\infty e^{i\alpha_{ins}} + \dfrac{i\Gamma\zeta}{b\pi} + \dfrac{i}{b\pi} \displaystyle\sum_{k=1}^{M} \Gamma_k \left(\frac{\zeta^2}{\zeta - \zeta_k} + \frac{\zeta}{1 - \zeta\bar{\zeta}_k} \right) \right]^2}{\left[(\zeta - 1)\left(\sqrt{z+b} \pm \sqrt{z-b} \right) \right]^2} \tag{B.3.8}$$

and at the leading edge ($z = -b$ or $\zeta = -1$)

$$H = H(-b) = \frac{b}{8} \left[2v_\infty \sin \alpha_{ins} + \frac{\Gamma}{b\pi} + \frac{2}{b\pi} \sum_{k=1}^{M} \frac{\Gamma_k (1 + \xi_k)}{(1 + \xi_k)^2 + \eta_k{}^2} \right]^2 \tag{B.3.9}$$

From Equation (B.3.4), Equation (B.3.7) becomes

$$\bar{F} = \frac{i\rho}{2} \lim_{\varepsilon \to 0} \int_0^{2\pi} \frac{H}{\varepsilon e^{i\theta}} \, d(\varepsilon e^{i\theta}) = -\rho\pi H(-b) \tag{B.3.10}$$

From Equations (B.3.9) and (B.3.10), the complex force at the trailing edge $F = F_x + iF_y$ is given by

$$F_x = -\frac{\rho b\pi}{8}\left[2v_\infty \sin\alpha_{ins} + \frac{\Gamma}{b\pi} + \frac{2}{b\pi}\sum_{k=1}^{M}\frac{\Gamma_k(1+\xi_k)}{(1+\xi_k)^2+\eta_k{}^2}\right]^2 \qquad (B.3.11)$$

$$F_y = 0$$

where the absolute value of F_x is the same as F_S given by Equation (2.6.6).

Vita

The author was born on July 7th, 1956 in Qingdao, Shandong Province, the People's Republic of China. He completed his primary school, middle school and high school in Beijing, China. In February of 1978, he entered the Department of Mathematics, Fudan University in Shanghai, China, and majored in mechanics. He graduated in February of 1982 with a B.S. degree. After graduating he worked as a teaching assitant in Beijing Agricultural Engineering University, and later he was granted a scholarship for postgraduate study. In September of 1985, he entered the Department of Engineering Science and Mechanics, Viginia Polytechnic Institute and State University. He obtained his M.S. degree in Engineering Mechanics. Then he continued the study for the degree of Ph.D in Engineering Science. He is a member of the Honor Society of Φ K Φ (Phi Kappa Phi).